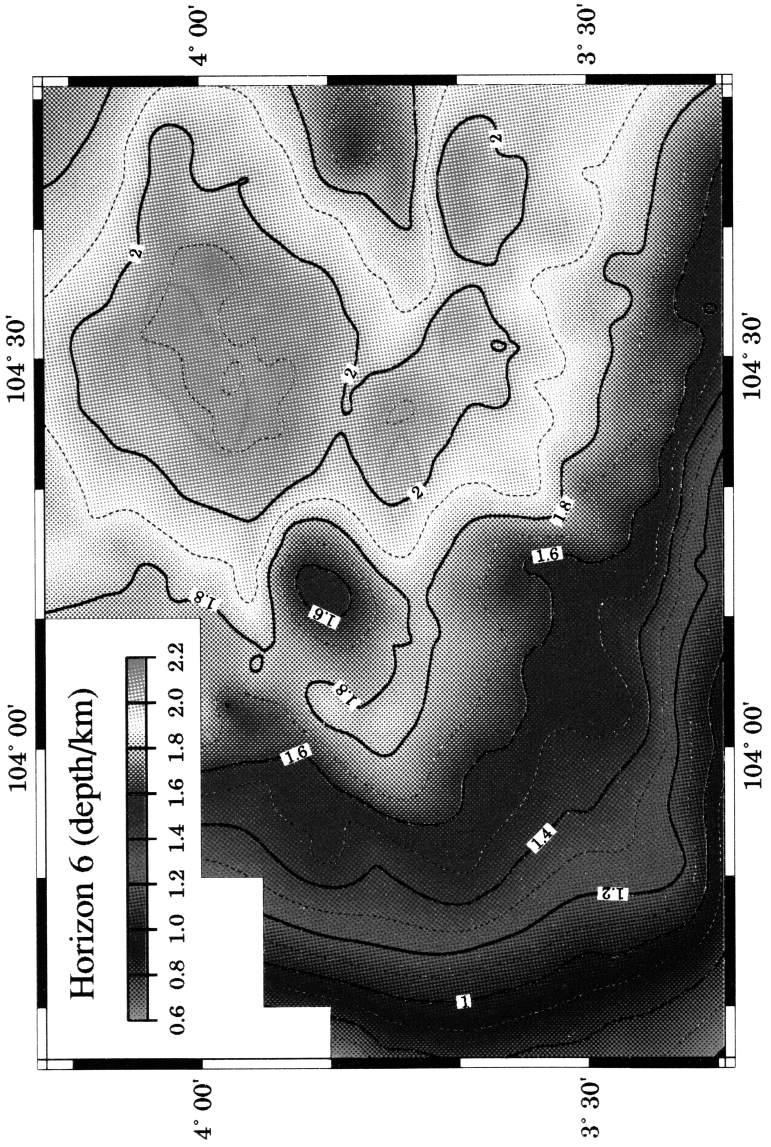

Figure 3.42. cont. (B) Structure map of Horizon 6— Top-Oligocene Unconformity. Inversion anticlines started to form over the main half-grabens. Continued next page....

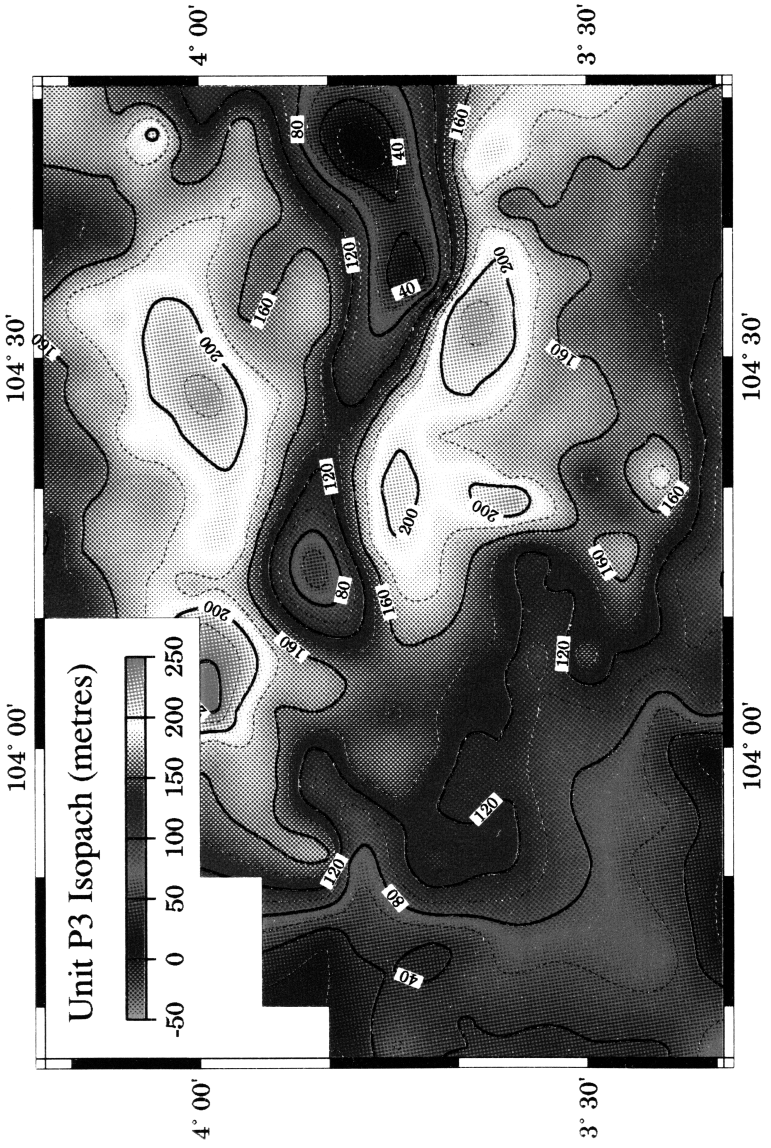

Figure 3.42. cont. (C) Isopach map of Unit P3 showing the general form of the inversion structures over the main half-grabens. Note the thinning of Unit P3 as a result of half-graben inversion. Continued next page....

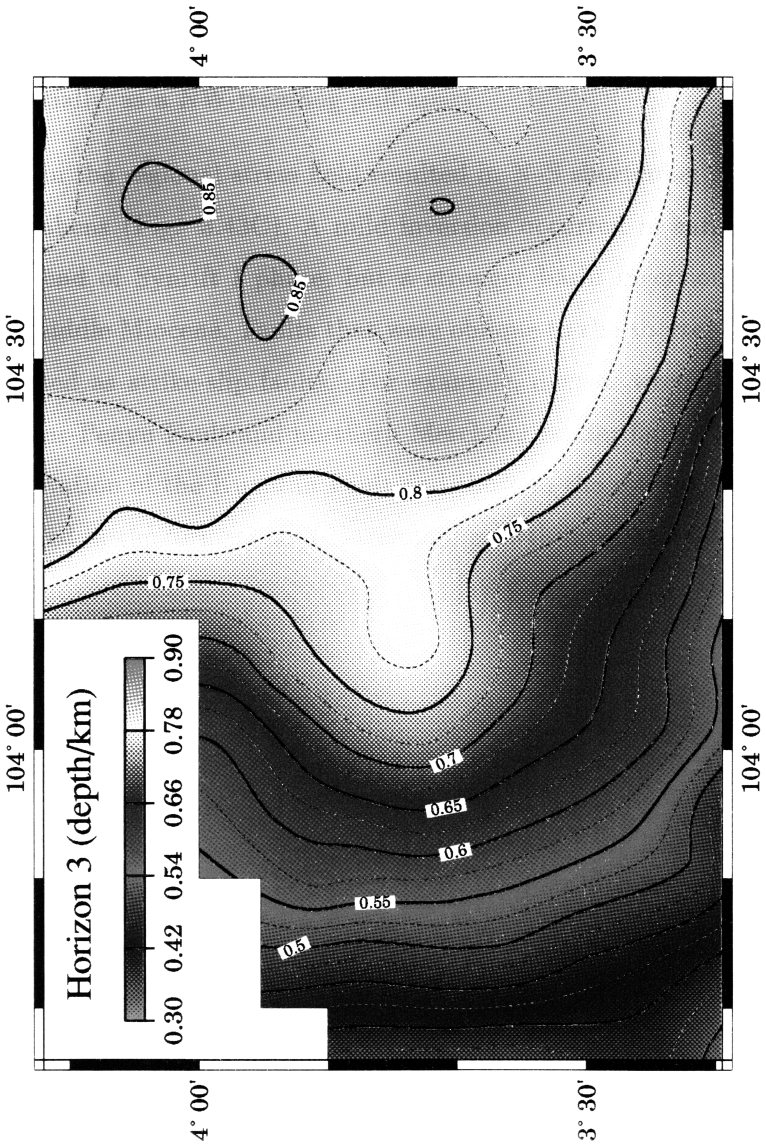

Figure 3.42. cont. (D) Structure map of Horizon 3— Mid-Miocene Unconformity. Gentle eastwards tilt of the Late Miocene Unconformity, implying slow post-Late Miocene subsidence during tectonically quiescent phase, which probably persists to the present day.

entation of the bounding faults (Fig. 3.43B). Where pre-existing faults are oblique to the regional extension direction, displacement along the faults is partitioned into strike and dip slip. Orthogonal extension occurred in the Kuantan Graben but oblique extension in the Rumbia and Merchong Grabens. Merchong Graben opened, essentially, as a NW-trending pull-apart.

A change in the regional stress field resulted in N–S shortening and inversion of the half-grabens (Fig. 3.43C). A mild inversion occurred in earliest Miocene times at the end of Synrift I phase, but a stronger basin inversion phase took place in the middle Miocene. Faults that were oblique to the shortening direction were reactivated as strike-slip faults. For example, dextral wrenching occurred along the Trans-Penyu Fault and northern Merchong border faults, while reverse dip-slip reactivation of the Kuantan Fault and those in the southeastern Rumbia Graben resulted in the formation of E-trending growth-inversion anticlines.

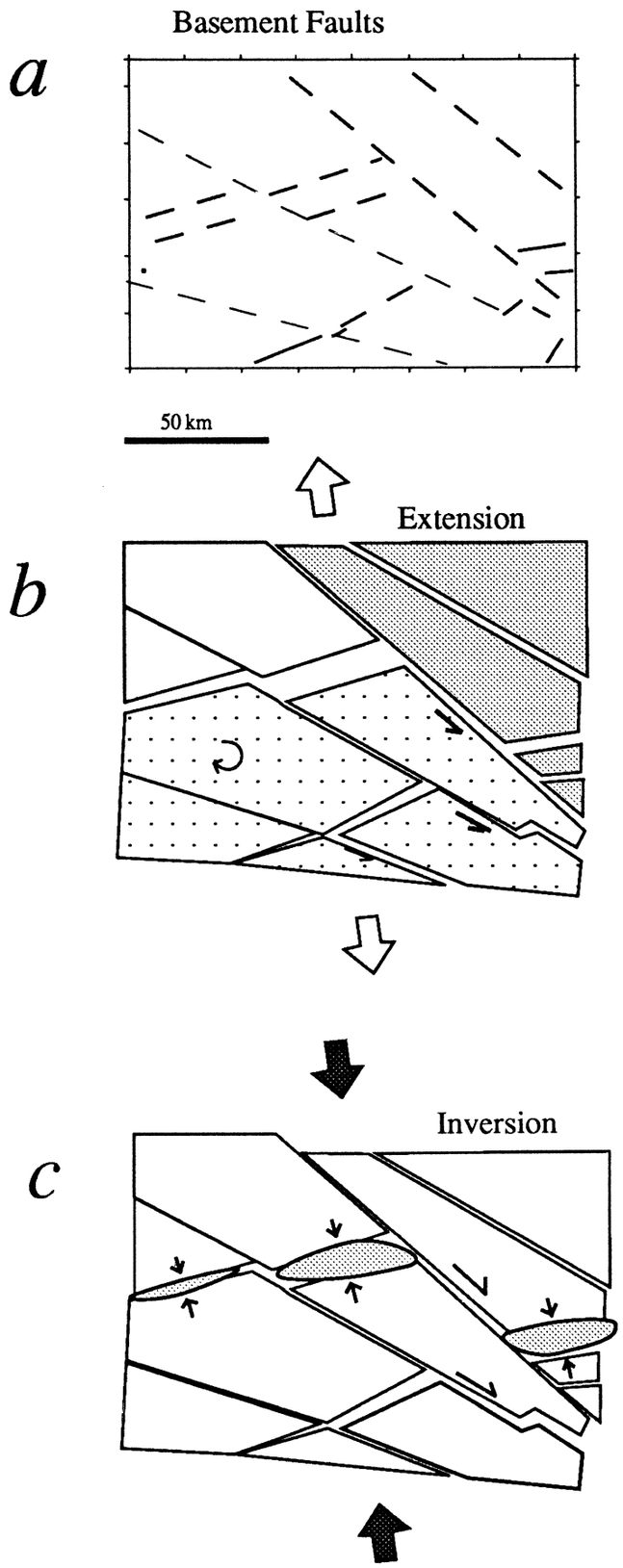

Figure 3.43. Development of the Penyu Basin by N–S extension, strongly influenced by presence of older basement faults. (A) Prior to basin formation. Basement faults shown by dashed lines. (B) N–S extension and reactivation of basement faults. (C) N–S shortening and inversion of half-graben.

Chapter 4

Structure II: The Malay Basin

The tectonic origin of the Malay Basin has been, for a long time, the subject of speculation, because detailed description of its structure has never been published. The Basin is situated at the centre of Sundaland and is the deepest among its interior extensional basins (Fig. 2.5, p. 31). Along with other Sundaland basins, the Malay Basin records a phase of widespread crustal/lithospheric extension in the region during early Tertiary times. The geological evidence from surrounding areas (Chapter 2) suggests that this extensional regime may have existed since Jurassic–Cretaceous times, probably, as a result of gravitational collapse after thickening of the lithosphere during the Late Triassic Indosinian Orogeny. The region may have been in a state of deviatoric tension since then, as the uplifted thickened lithosphere tries to maintain isostatic equilibrium. Jurassic-Cretaceous intermontane extensional/strike-slip basins in Peninsular Malaysia and Thailand are a testament of the post-orogenic extensional tectonics prior to the Tertiary. Widespread rift basin formation, however, did not take place until, probably, the early Oligocene.

Kingston *et al.* (1983), among others, postulated that extension in a back-arc setting resulting from subduction of the Indian Plate beneath Sumatra may have been responsible for lithospheric tension in Sundaland and for the formation of basins such as the Malay Basin. Tensional forces in the overriding plate at a subduction zone is attributed, commonly, to trench rollback (Dewey, 1980), which is caused primarily by the negative bouyancy of the subducted slab ("slab

pull" force). This force may have acted in concert with the lateral component of the gravitational force due to excess potential energy of the thickened Sundaland lithosphere. Back-arc extension is probably not the main cause of extension in Sundaland during the early Tertiary, for the following reasons. First, the subduction along the Sumatra Arc has been in progress since Jurassic times (Wajzer *et al.*, 1991) whereas the Tertiary extensional basins did not begin to form until Paleocene-Oligocene times. Secondly, the Malay Basin is ~1000 km away from the Sumatra trench, unlike many extensional back-arc basins floored by continental crust (*e.g.* Okinawa Trough, Letouzey and Kimura, 1985) which form, usually, within about 100-200 km from the trench axis. Thirdly, the strain regime in Sumatra does not appear to favour widespread back-arc extension. Studies of "back-arc" basins in Sumatra (*e.g.* Moulds, 1989, Situmorang *et al.* 1991) have demonstrated the importance of pre-existing basement heterogeneities, particularly trench-parallel strike-slip faults, in controlling extensional basin formation. More importantly, the highly-oblique subduction of the Indian plate beneath Sumatra has resulted in strong slippage of ~2 cm a^{-1} along the trench axis and strike-slip partitioning of the northward-convergent motion of the plate by up to ~400 km of dextral slip on the Sumatra Fault Zone (Hutchison, 1989a, p. 38). Moreover, the apparent lack of a Benioff zone beneath Sumatra, apparently truncated at the Sumatra Fault Zone, suggests that slab-pull forces have contributed little to the extension in the overriding Sundaland lithosphere.

Another model to consider is the so-called "active" rifting model, in which continental extension results from shear stress at the base of the lithosphere induced by divergent asthenospheric upwelling. A similar model was suggested by Hutchison (1989a, p. 180–183) who postulated that thermal doming of central Sundaland occurred during the late Cretaceous, leading to uplift and extension in the Malay Basin (Fig. 2.1, p. 24). If this is correct, there should be evidence for late Cretaceous–Paleogene "synrift" sedimentation in the Basin, which is not available. Also, evidence for pre-rift uplift of the area is difficult to observe from the available offshore seismic data. Hence, this idea is highly speculative, although

it should still be considered as an alternative when more data becomes available.

Tapponnier *et al.* (1982, 1986) suggested that the Malay Basin may have developed as a pull-apart along a major strike-slip fault, reactivated as a result of the India-Eurasia collision in mid-Eocene times (45 Ma, Dewey *et al.* 1989). Subsequently, Daines (1985) and Polachan and Sattayarak (1989) adopted the model to explain the development of the West Natuna and Thai Basins, respectively. This is an attractive idea because it explains some key observations: (1) the almost synchronous development of extensional basins in Sundaland during late Eocene–Oligocene, which is linked to the time of the collision, and (2) extension occurs within a relatively narrow zone of deformation emanating from the collision zone. This zone of intraplate extension could well represent one of the major strike-slip faults observed in their analogue experiment (Tapponnier *et al.*, 1982).

None of the proposed models, however, were based on detailed structural analysis of the individual basins. Most authors did not provide direct structural evidence from the Malay Basin to support their tectonic models. Although a brief description of the Malay Basin's structure was given by Hamilton (1979), most of the literature on the region mentions the Malay Basin only in passing. Most of the published works on the Basin itself are limited to sedimentological or engineering-based studies of specific oil fields. In this chapter, previously unpublished structural data from the Basin are studied to gain further insight into its kinematic development and interpret the Basin's tectonic evolution.

4.1 Stratigraphic Framework

The sediment in the Malay Basin, as in the neighbouring Penyu and West Natuna Basins, is almost exclusively siliciclastic. The oil companies working in the Malay Basin have subdivided the strata, informally, into seismo-stratigraphical units (referred to as "groups" within the industry) (Fig. 4.1). These units are defined by basin-wide seismic reflectors (Armitage and Viotti, 1977), some of which represent

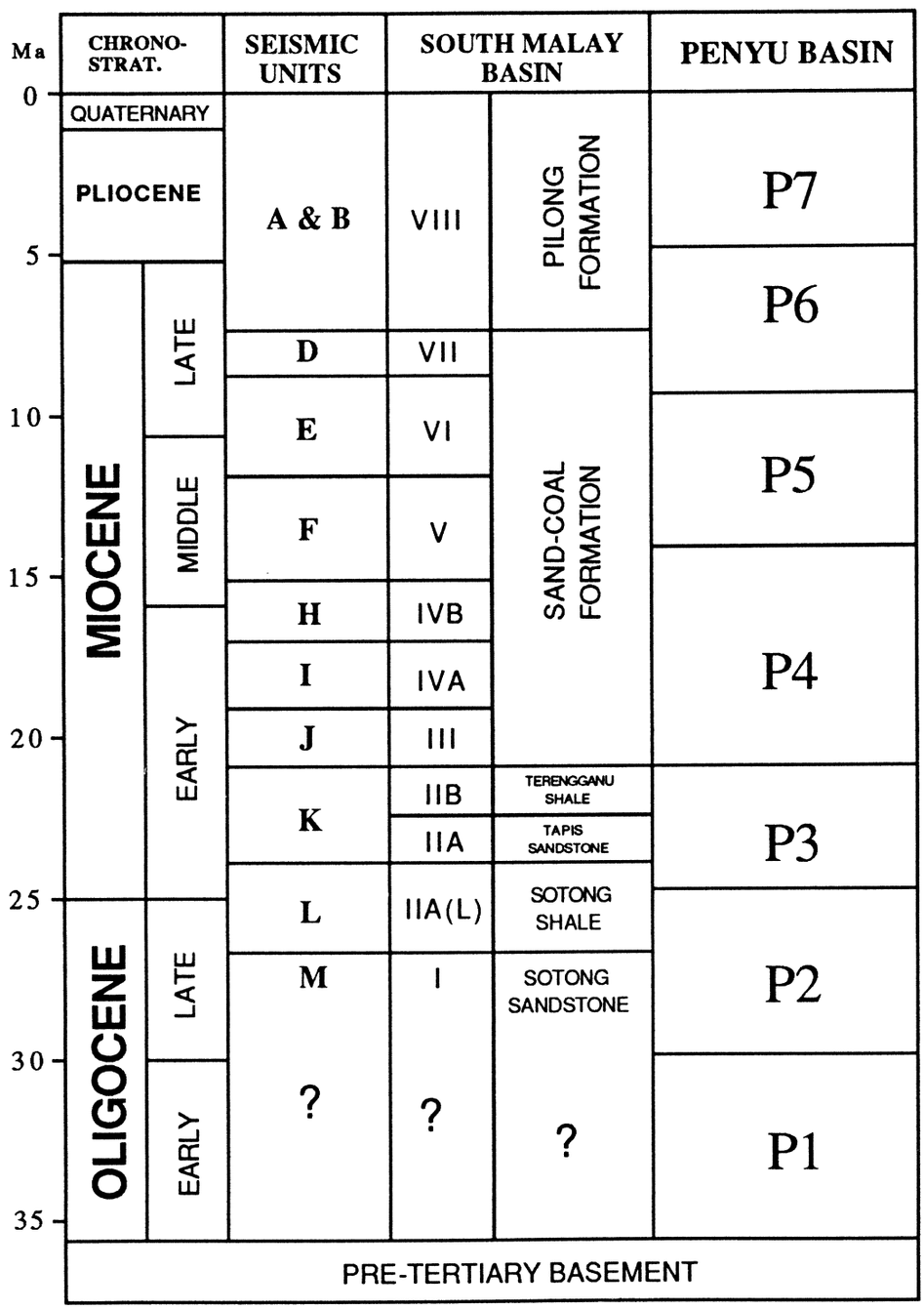

Figure 4.1. Seismo-tratigraphy of the Malay Basin and its tentative correlation with the more local, stratigraphy of its southern part (M.N. Ramli, 1988), and with the Penyu Basin (Chapter 3).

erosional unconformities on the flanks or in the southern part of the Basin, where there appears to have been a major inversion during the middle–late Miocene (ASCOPE, 1981). The sedimentation history of the Malay Basin is similar to that of the Penyu/West Natuna Basins; it may be described as comprising three main phases (Armitage and Viotti, 1977; Hamilton, 1979; ASCOPE, 1981; Murphy, 1989), described below.

Oligocene extensional phase

This represents the fault-controlled or "synrift" phase, which is the result of widespread extension in continental Sundaland. The synrift sedimentary succession, represented by Units M and older, consists of alternating sand-dominated and shale-dominated, nonmarine sequences deposited in fluvial-lacustrine environments. Much of the synrift stratigraphy lies more than 6–7 km deep, beneath the central part of the Basin and has not been drilled into. Information on the synrift rocks comes from, mainly, areas of shallow basement in the southeastern part of the Basin, where the effect of basin inversion during the early postrift phase has been most intense. The oldest sediment penetrated so far is no older than Oligocene (Morley *et al.*, 1994), although older sediment may still exist in the deeper, central part of the Basin.

Early–middle Miocene subsidence/inversion

Following the cessation of extensional faulting in late Oligocene times, the Basin continued to subside with the deposition of Units L to E. The Basin was probably at or near sea level by early Miocene times, as indicated by the abundance of coal-bearing strata in this part of the succession. The sediments were deposited in low-energy, dominantly nearshore/marine to fluvially-influenced deltaic environments. The absence of extensional faulting suggests that this phase of sedimentation represents the "postrift" stage, which resulted from thermal relaxation

of the stretched lithosphere (Chapter 6). Increasing marine influence upwards in the succession (Armitage and Viotti, 1977) suggests a relative rise in sea level, probably, because of rapid subsidence during the early postrift phase.

The middle–late Miocene period of subsidence was accompanied by compressional tectonics, which resulted in (1) local inversion of half-grabens by reactivation of their bounding faults, and (2) a major uplift in the southeastern part of the Basin (Fig. 4.4). A prominent, truncational seismic reflector marks the top of the succession, which is probably equivalent to the Postrift I sequence in the Penyu Basin (Chapter 3). This unconformity truncates folded and uplifted strata as old as Unit H in the southern part of the Basin and is overlain by undeformed marine sediment of Units A and B. The deformation was contemporaneous with sedimentation, such that erosion and nondeposition on the crests of the structures occurred simultaneously with deposition on the flanks. Murphy (1989) has estimated that up to 1200 m of sediment have been eroded off the crests of some structures, but this is probably a gross overestimation, considering that the structures are syndepositional (growth) features. Sedimentation in Units D, E, and F in the central and northern parts of the Basin was uninterrupted because the uplift was restricted to its southern end (Fig. 4.4). Erosion in the south may have supplied sediment to the north.

Late Miocene–Pliocene "quiescent" phase

This phase represents a gentle subsidence of the Basin without significant tectonic activity, and is probably equivalent to the Postrift I phase in the Penyu Basin (Chapter 3). The resulting sediment in Units A and B, which occurs above the Middle-Late Miocene Unconformity, consists of predominantly marine clays deposited in nearshore to shallow marine environments during an overall marine transgression.

4.2 Structural Characteristics

The Malay Basin is about 350 km long, 250 km wide, and is filled with up to 14 km of sediment. The present-day water depth is only about 70-80 m. Figure 4.2 illustrates the overall geometry of the Basin based on the depth to the top of pre-Tertiary basement. The map shows two main subbasins separated by a

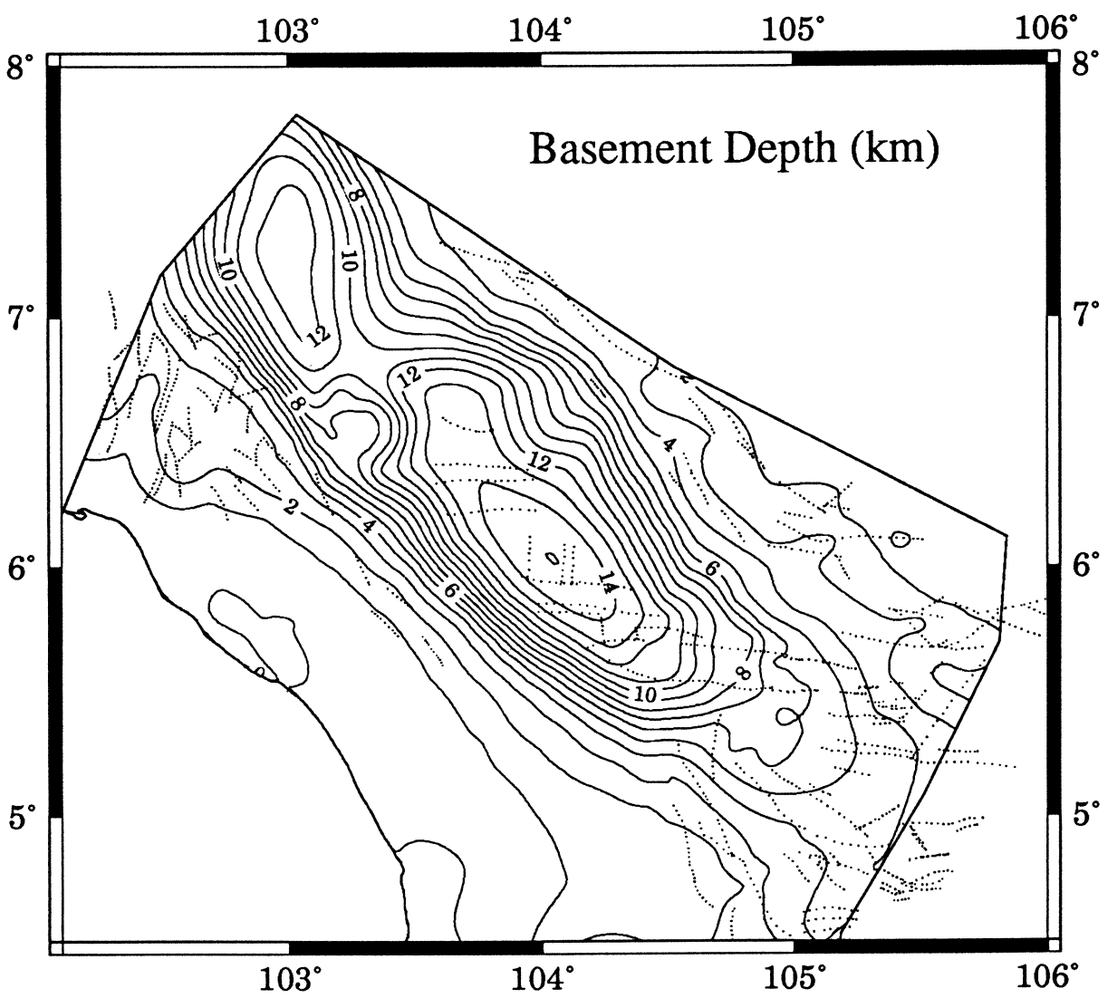

Figure 4.2. Basement structure of the Malay Basin. Contour intervals in km. Dotted lines represent traces of major basement faults. Compiled from unpublished PETRONAS maps.

N-trending basement high. Very little is known about the northern subbasin, but its northerly trend suggests that it is related, structurally, to the N-trending grabens in the Gulf of Thailand to the northwest of the area. The main Basin has a northwest-southeast trend, parallel to that of Peninsular Malaysia. The depth

contours suggest that the Basin is almost symmetrical in cross section, although its southwestern flank appears to be slightly steeper. The basement shallows gradually to the southeast as a result of basement uplift (Fig. 4.4).

The traces of major basement faults are shown in Fig. 4.2. Most of the faults strike roughly east-west, about 35° oblique to the basin trend. No major marginal fault or fault zones are present. Hence, the structural relationship between the basement fault pattern and the basin trend is not so obvious. The evidence seems to suggest that the Malay Basin is not a simple rift formed by orthogonal NE–SW extension.

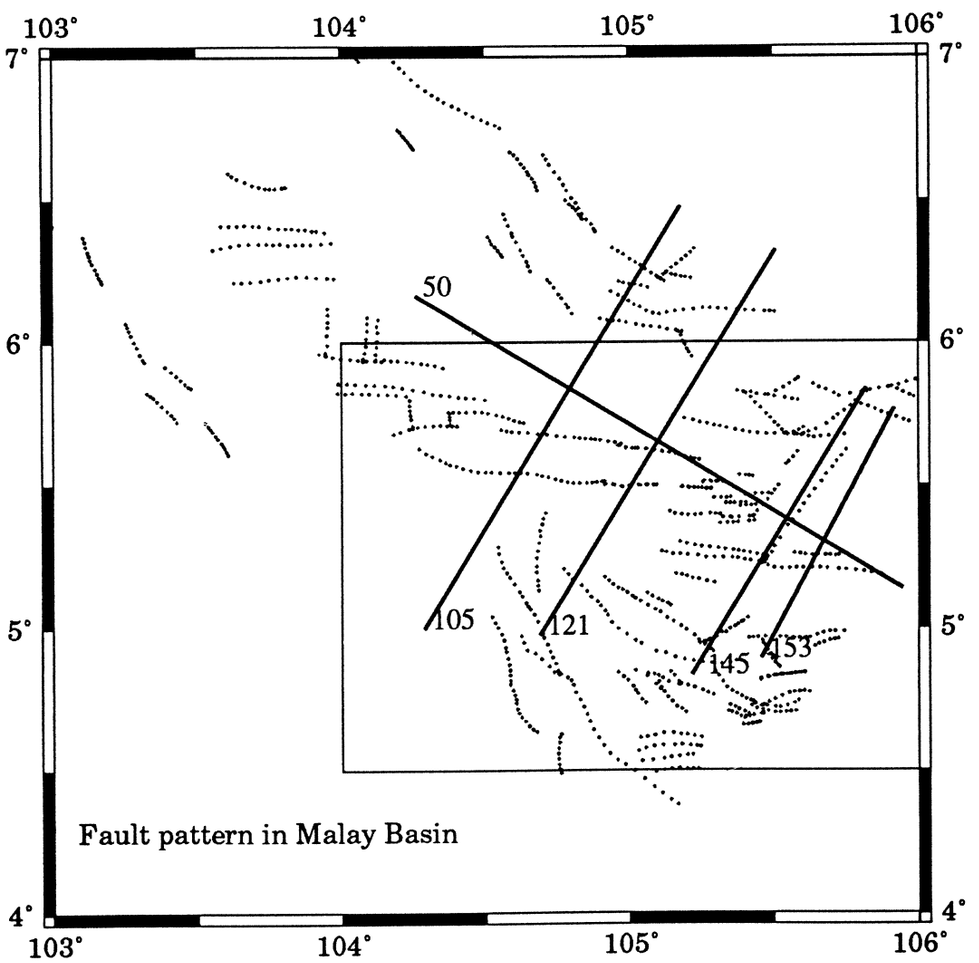

Figure 4.3. Basement fault pattern in the Malay Basin. Box represents area shown Fig. 4.12 (p. 134). Solid lines represent seismic profiles discussed in this chapter.

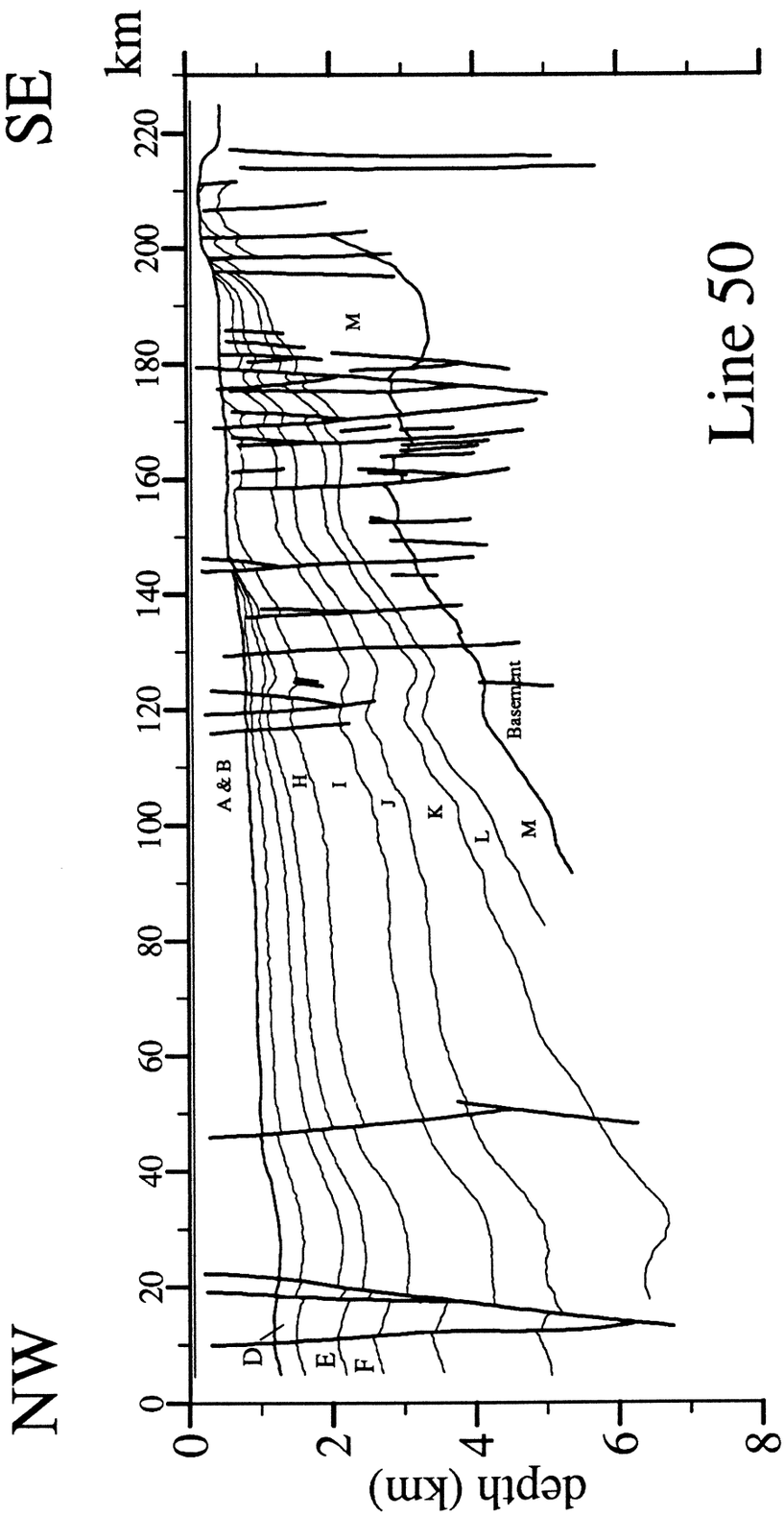

Figure 4.4. NW-SE section, roughly along the axis of Malay Basin. Note the deepening of basin to the NW, and basement uplift in the southeast, with truncation of postrift strata by the regional Mid-Miocene Unconformity.

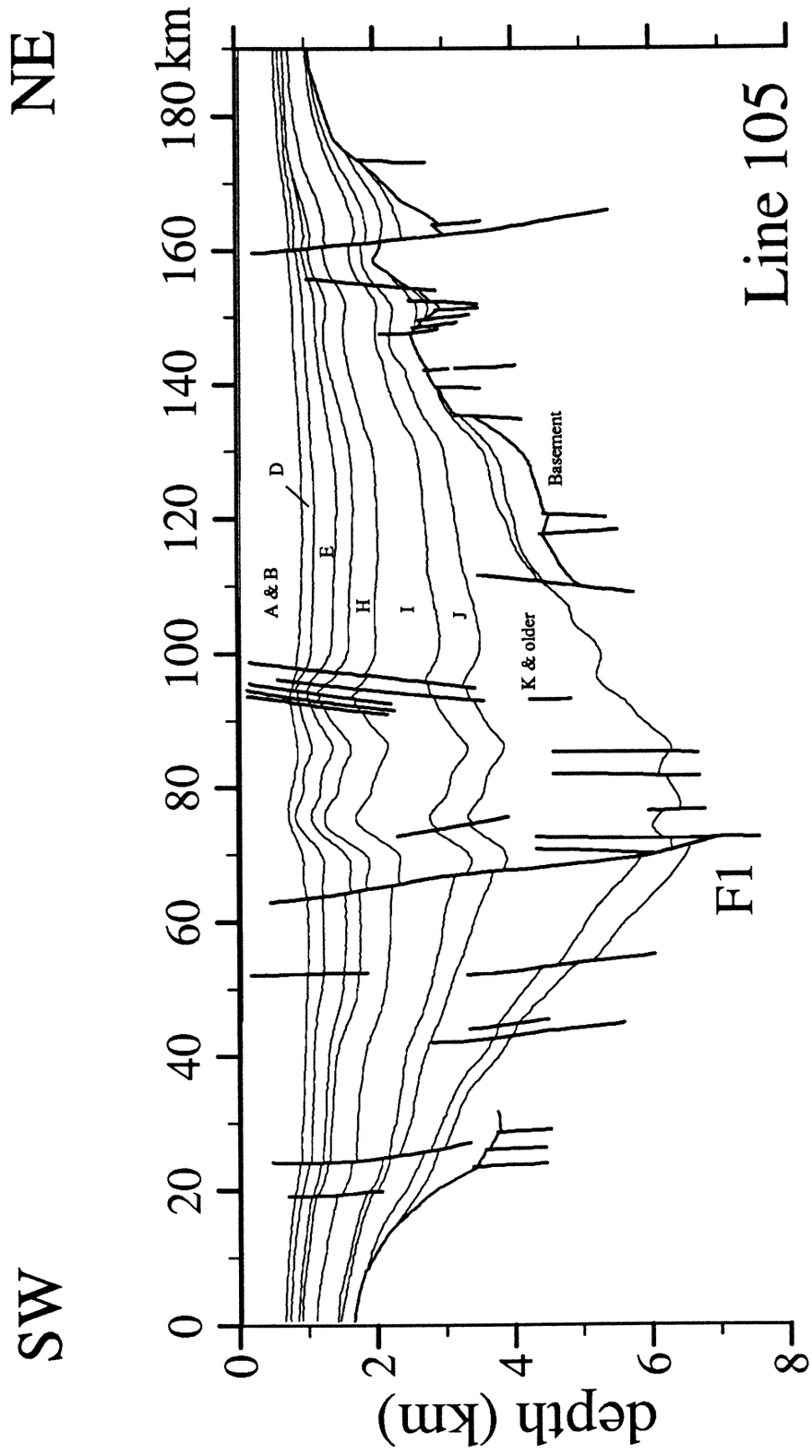

Figure 4.5. Seismic line 105, Malay Basin. NE-SW profile across the centre of the Basin showing almost symmetrical, steer's head basin geometry and the characteristic onlap of sedimentary strata onto basement at the margins. Note the folded strata at centre of Basin, resulting from transpressional tectonics prior to truncation by the Mid-Miocene Unconformity. Shortening along the plane of profile is estimated to be about 15 km. Depth-converted seismic line digitized from unpublished sections supplied by PETRONAS.

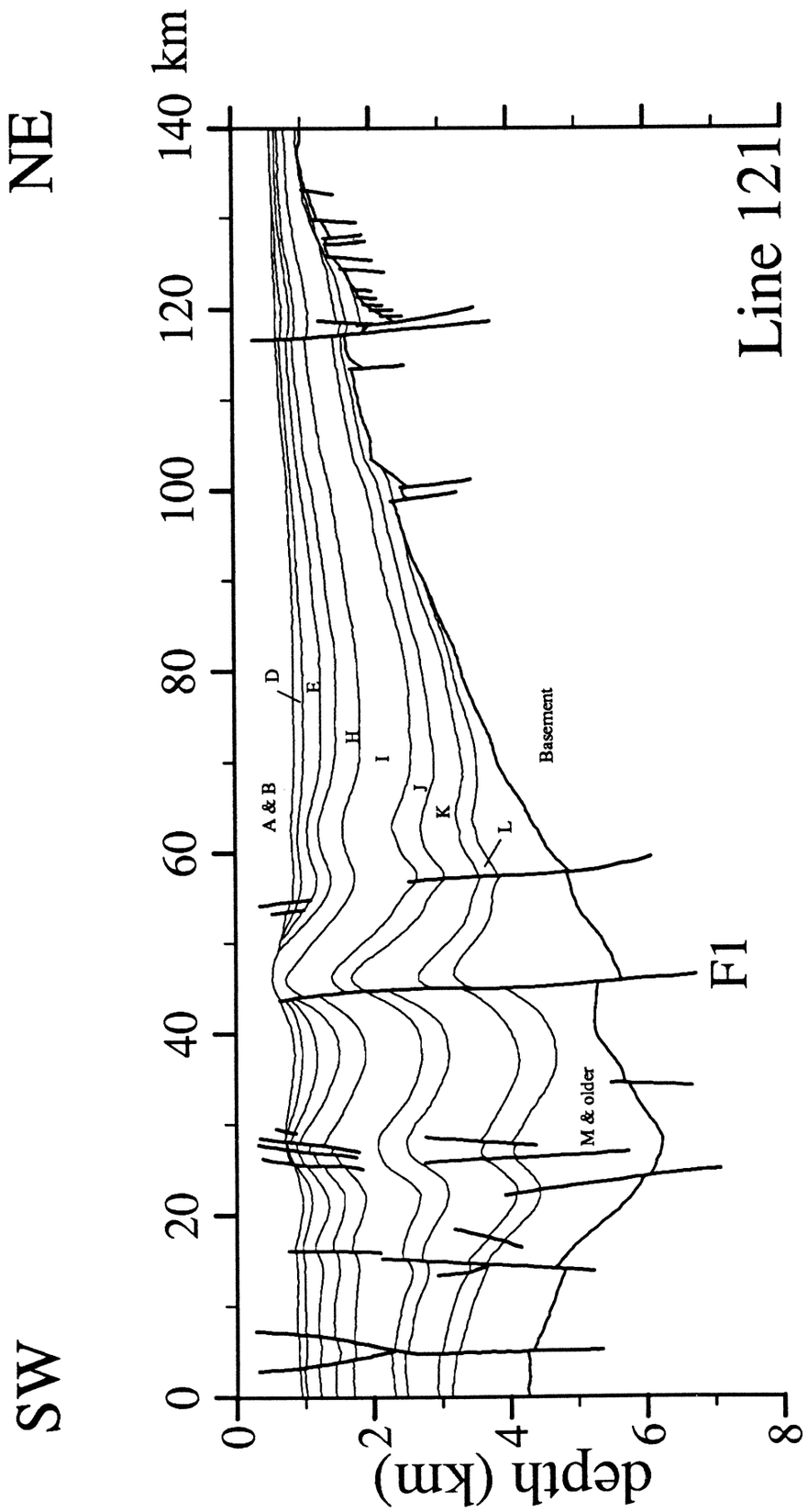

Figure 4.6. Seismic Line 121, Malay Basin, located southeastwards of Line 105 in Fig. 4.5. Note the more intense folding at centre compared to Line 105. Large reverse dip-slip occurs on the main bounding of the Tapis structure, associated with oblique reactivation of the fault during transpressional inversion. Based on depth converted seismic line, digitized from unpublished sections supplied by PETRONAS.

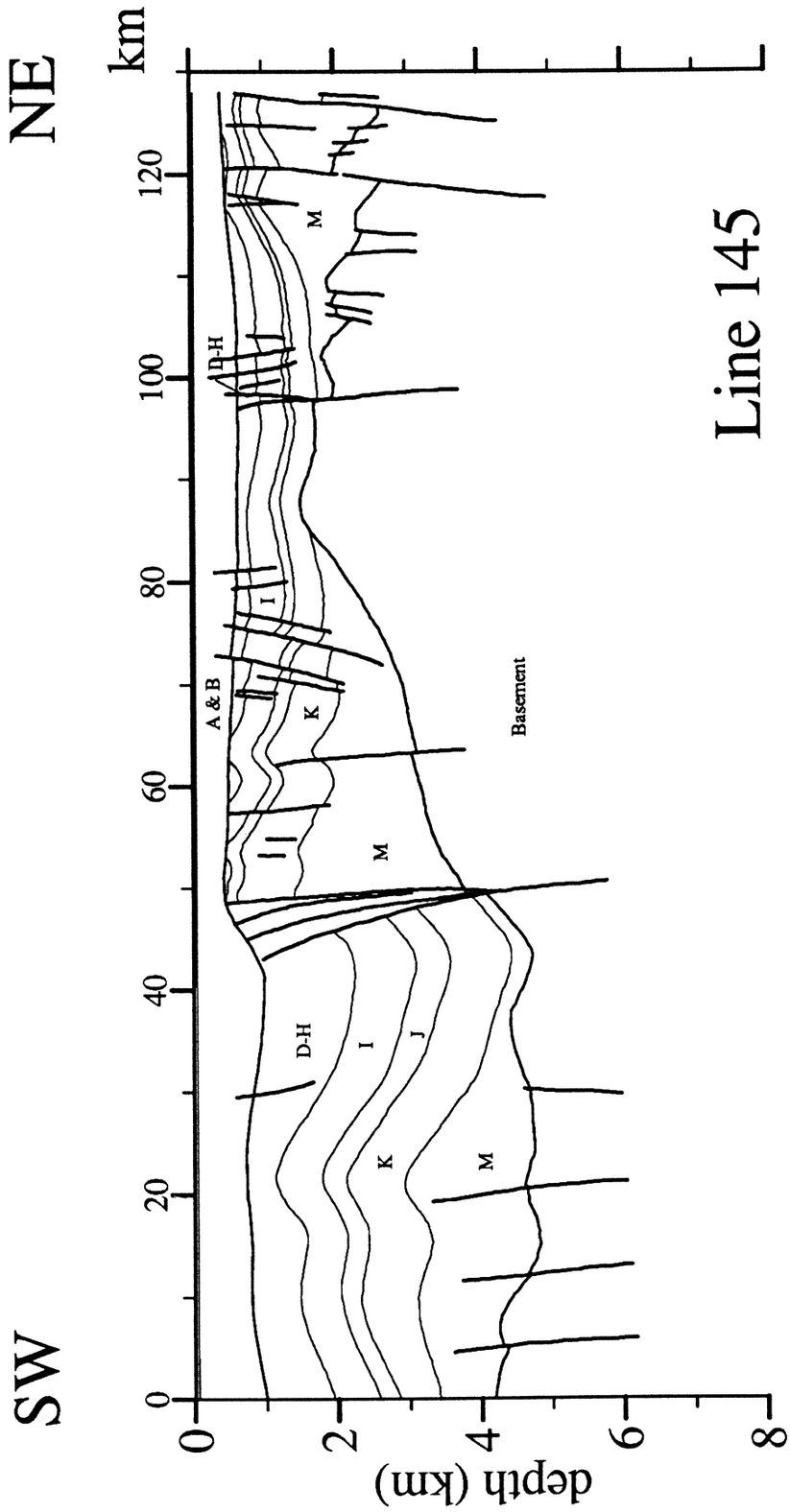

Figure 4.7. NE-SW geoseismic section across the Basin, based on Line 145, showing the basin geometry and the major inversion structures at Duyong, Ledang and N. Peta. The triangular geometry of the uplifted M unit suggests the structures are formed by inversion of half-grabens as a result of reactivation of the bounding fault (F1, F2, and F3) which were formerly normal-separation faults. The geometry of F1 suggests strong strike-slip and transpressional component during reactivation.

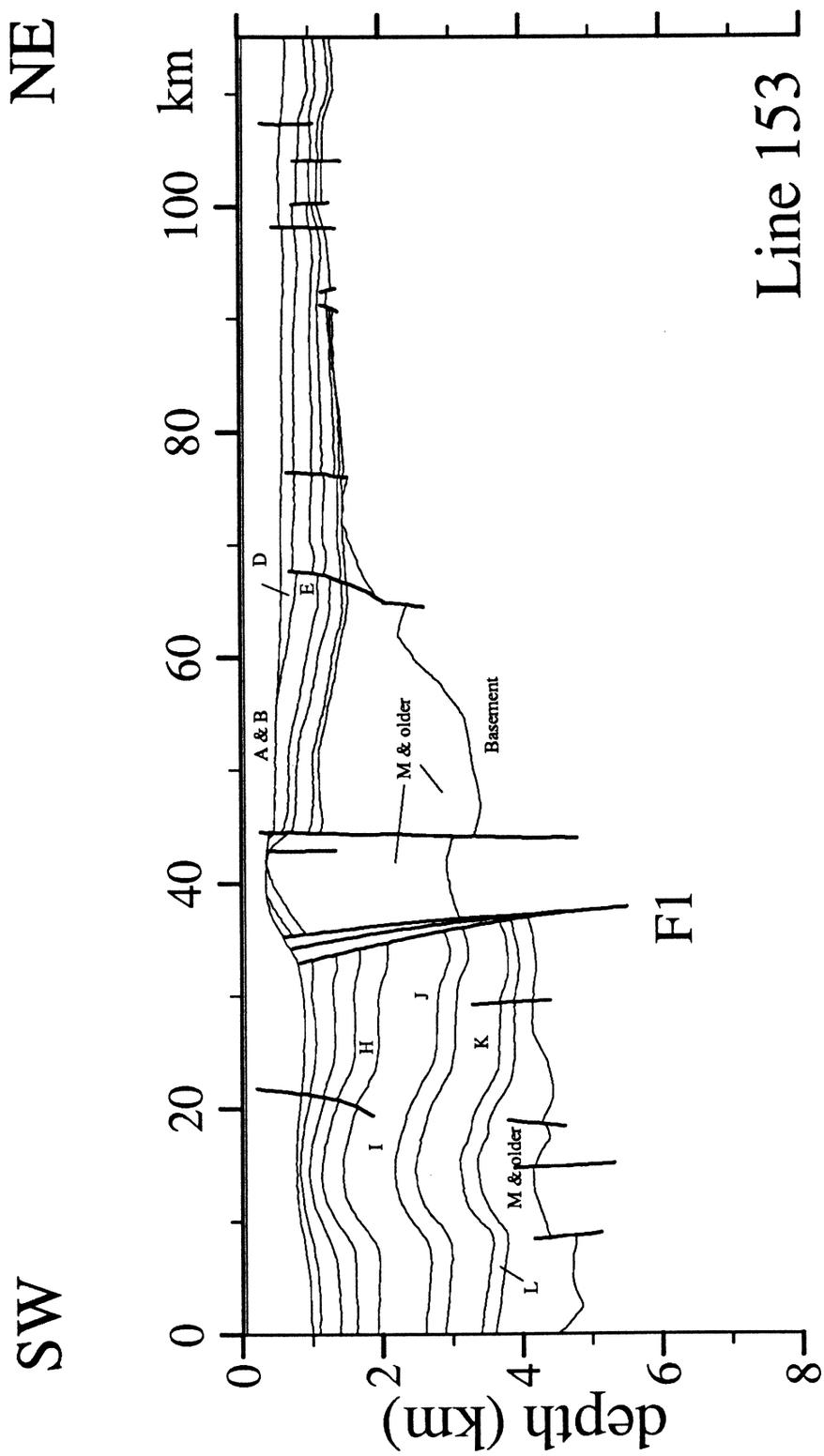

Figure 4.8. Seismic line 153, Malay Basin. This line is located within the Indonesian territory but still in the Malay Basin. Note up to 4 km of vertical displacement of Top M by the main fault F1, indicating increasing intensity of inversion-related deformation southwards (compare with Figs. 4.5 and 4.8). Based on depth converted seismic line, digitized from unpublished sections supplied by PETRONAS.

Seismic data (Figs. 4.5 – 4.8) indicate that the basement faults were originally the border faults to major extensional half-grabens which, subsequently, were inverted in middle–late Miocene times. The major inversion structures in the southeastern part of the Basin are formed of tightly folded postrift strata that once filled the half-grabens. The bounding faults to the half-grabens have been reactivated as reverse and/or strike-slip faults and, as a result, show complicated upward-diverging geometries, similar to positive flower structures characteristic of wrench faulting (*e.g.* Harding, 1985, 1990). Thus, shortening across the half-grabens appears to have involved, also, significant component of strike slip along the E-trending faults.

In Fig. 4.6, for example, the rapid thickening of Unit M towards Fault F1 suggests that the Tapis structure was formed by inversion of an underlying half-graben. Based on the offset of the top-M marker, it is estimated that about 500 m of reverse dip-slip on the fault has taken place. Figure 4.9 is a smaller-scale depth-converted seismic section across the structure. The geometry of the structure resembles a flower structure, which suggests a significant component of strike slip along the main bounding fault associated with transpressional deformation.

Half-graben inversion on the flanks of the Basin is not as severe as at the centre. Figure 4.7, which is based on Line 145 in the southern part of the Basin, shows the varying degrees of inversion between the flanks and central region. At the centre of the profile are two major inversion anticlines— the Ledang and Duyung structures. The Duyung structure, which is about 40 km across, is a relatively symmetrical anticline. Negligible offset of the Top-Basement reflector suggests that the half-grabens underlying the structure have been been completely inverted. The Ledang structure is underlain by an asymmetrical half-graben which, also, has been completely inverted as a result of reactivation of its border fault (Fault F1 in Fig. 4.7). As a result, its hangingwall now lies above the footwall. The steepness of the fault, and the presence of overturned strata to the southeast of it, suggest that its reactivation was associated with considerable shortening and,

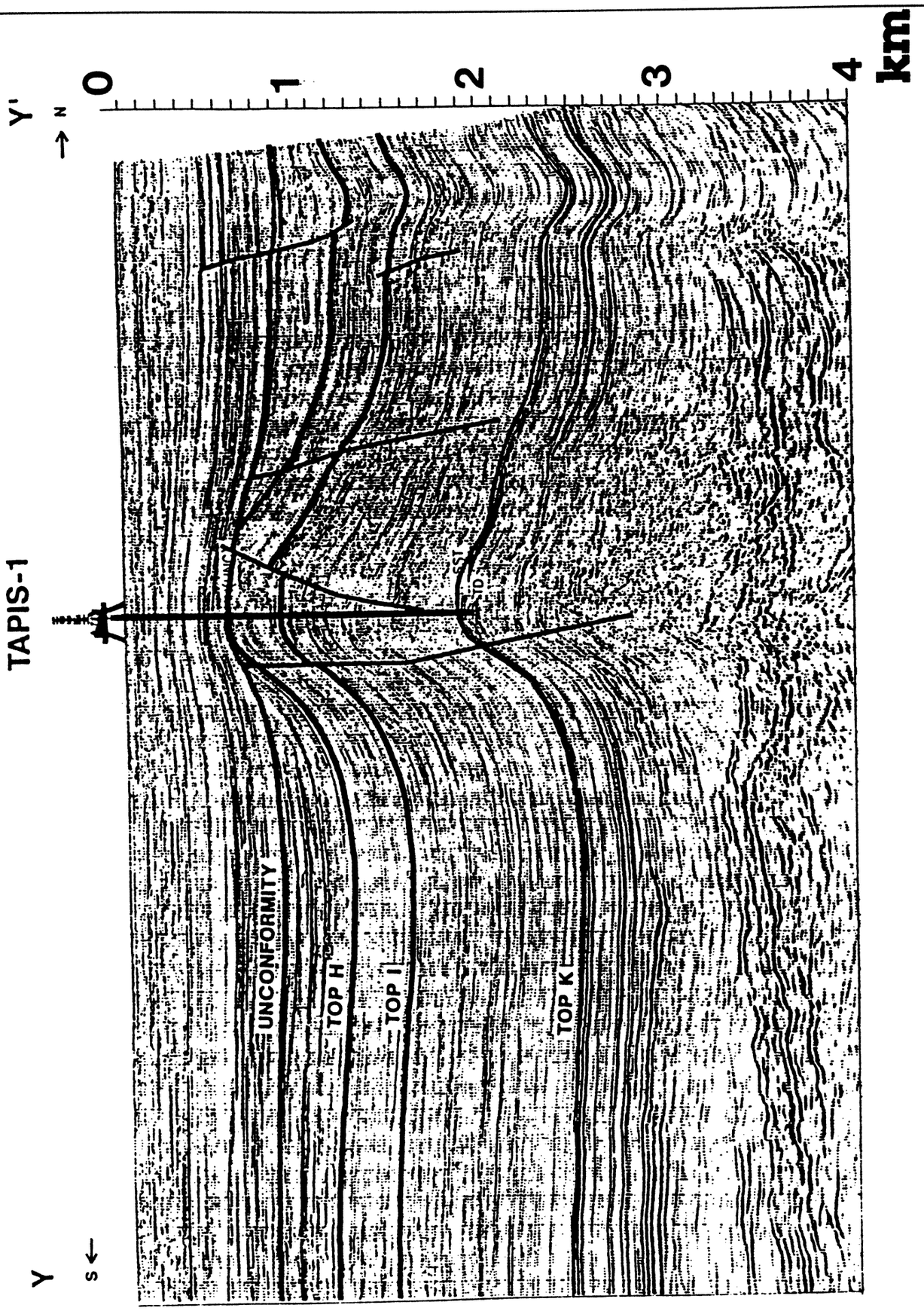

Figure 4.9. Seismic section across the Tapis structure, central Malay Basin (reproduced from Waples *et al.* in press). Bottom panel shows an interpretation of the structure, which suggests an upward diverging fault pattern characteristic of wrench structures.

perhaps also, strike-slip motion. At the northeastern end of the profile, there are two synthetic half-grabens which show less severe inversion, such that their half-graben geometries are still preserved. The milder inversion here has resulted in the gentle folding of the half-graben fill above the bounding fault, rather similar to the structures observed in the Penyu Basin (Chapter 3). Figure 4.10 shows schematically the structural style that results from different degrees of half-graben inversion. Mildly inverted structures are typical of those observed in the Penyu Basin, whereas strongly and completely inverted half-grabens are characteristic of the southern Malay Basin, and also in the West Natuna Basin. In some parts of the West Natuna Basin, thrusts and reverse faults are common (Ginger *et al.*, 1993).

Figure 4.5 is a section across the centre of the Basin, showing a typical steer's head geometry, resulting from progressive thinning of sedimentary units and onlap towards its margins. The overall basin geometry suggests formation by a lithospheric stretching mechanism (McKenzie, 1978; Dewey, 1982), whereby subsidence results from brittle extension in the upper crust and, later, thermal subsidence of the cooling lithosphere (Chapter 6). The basement reflector is not well-imaged in this profile because it is too deep, and thus gives poor seismic signals. The deformed strata at the Basin centre appears to be the result of transpression along fault F1.

The inversion structures shown in Figs. 4.5– 4.7, are only two of many anticlinal structures in the Basin. Figure 4.11 is a map of the anticlinal axes in the Basin. The figure shows that the majority of the anticlines are oriented roughly E–W, parallel to the basement fault trend (Fig. 4.2). Figure 4.12 is a map of the southern part of the Basin, representing the structure of the Top-I marker. The map shows that the location and geometry of the inversion anticlines are strongly controlled by the underlying E-trending half-graben border faults. The *en echelon* pattern of the inversion anticlines in the Malay Basin has led Hamilton (1979) to suggest that NW-trending right-lateral shear has played an important

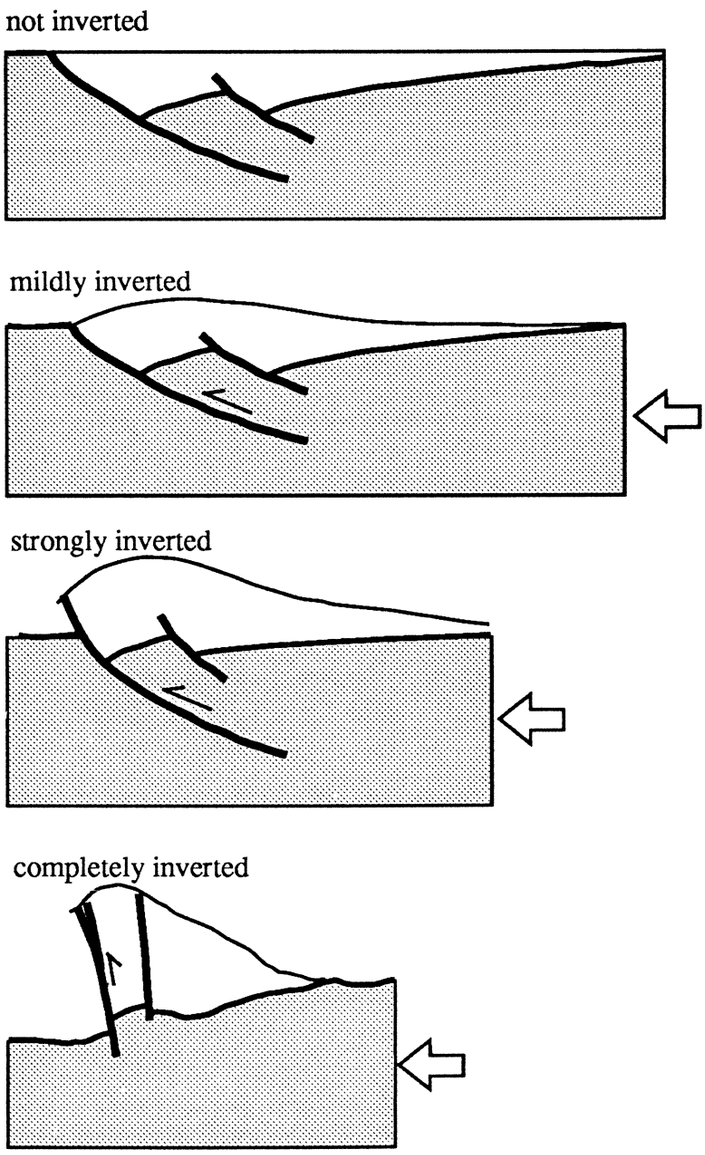

Figure 4.10. Structural style resulting from different degrees of inversion involving half-grabens. Based on structures observed in the Malay and Penyu Basins.

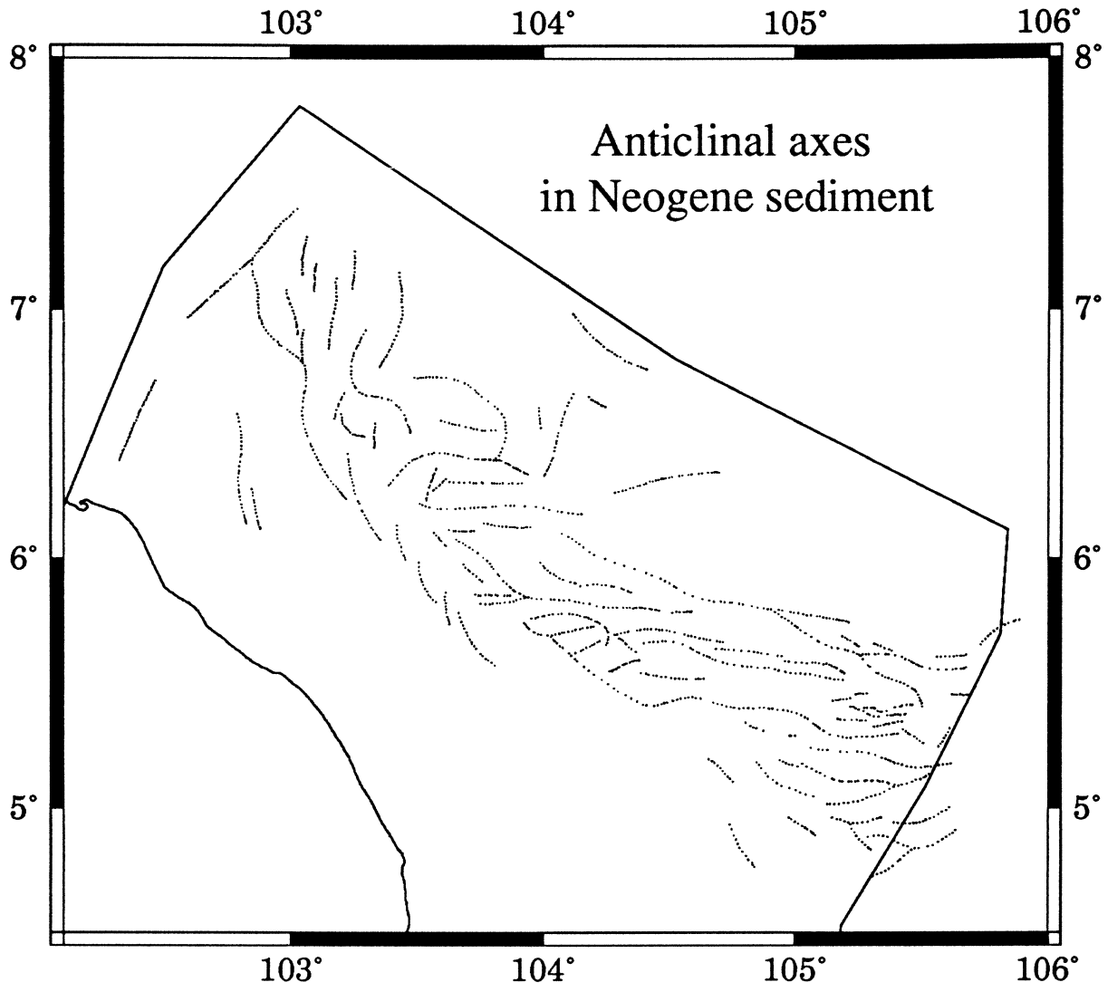

Figure 4.11. Simplified map of Malay Basin showing the axial traces of major anticlinal structures in Neogene strata, formed during the main basin inversion phase (Early Postrift) in middle-late Miocene times. Digitized from unpublished map of PETRONAS.

part in their formation. Figure 4.13 shows two possible ways in which *en echelon* anticlines could have formed as a result of dextral simple shear. In model A, the anticlines in the sedimentary cover were formed above a basement wrench-fault which acted as the principle displacement zone, as predicted by the classical wrench fault model, shown in Fig. 4.13B. Alternatively, as shown in Fig. 4.13C, folding could have resulted from distributed simple shear of a zone of deformation containing pre-existing *en echelon* half-grabens that are oblique to the zone boundaries. Half-graben inversion is, thus, caused by the N–S shortening component of shear. This model is preferred because there is no evidence for the existence of a throughgoing basement strike-slip fault in the Basin that could have acted as

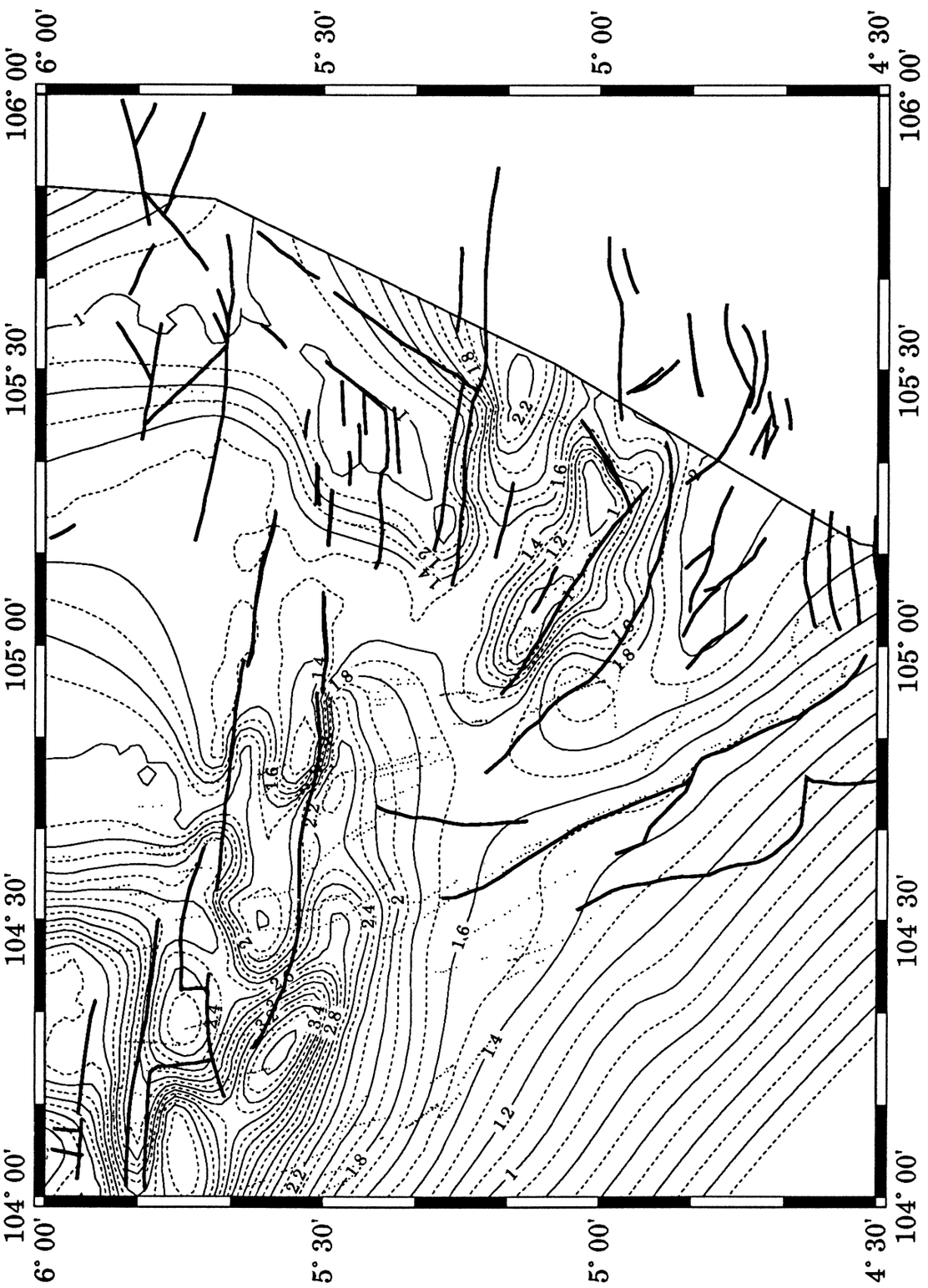

Figure 4.12. Structural contour map at top of Unit I, southern Malay Basin, showing the relationship between basement faults and anticlines. Location of area shown in Fig. 4.2. Bold lines represent major basement faults whereas dotted lines are faults in sedimentary cover.

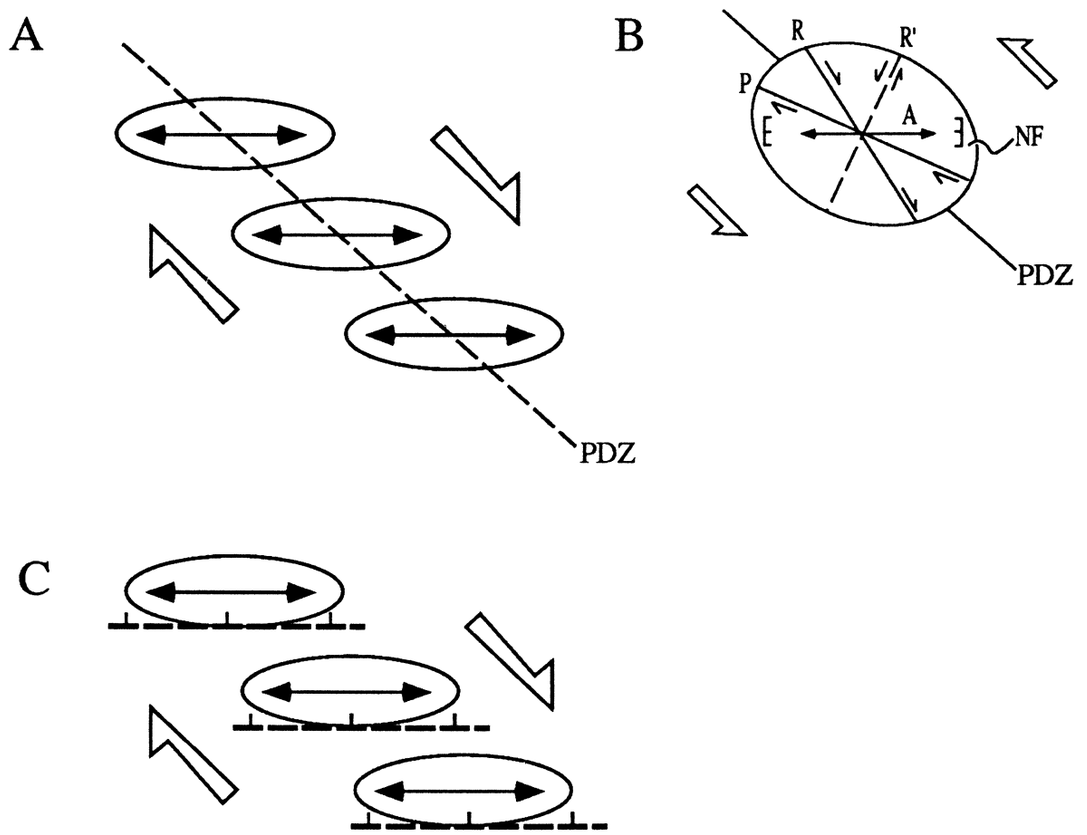

Figure 4.13. Possible models of *en echelon* folding in a right-lateral wrench fault system. (A) Fold configuration (ellipse with plunging arrows) in sedimentary layer above a principal displacement zone (PDZ) at depth (dashed line). (B) Strain ellipse representation of a right-lateral wrench system (after Christie-Blick and Biddle, 1985). NF– normal fault, A– anticlinal axis, R– Riedel shear, R′—antithetic Riedel shear. P– P shear. (C) Folds developed above north-dipping, *en echelon* normal faults by buckling of sedimentary cover in response to distributed deformation resulting from right-lateral shear.

the principle displacement zone, which has been confirmed in a recent study by Ismail *et al.* (1994). Hence, unlike in the classic wrench-fault model whereby a single fault acts as the principal displacement zone (Christie-Blick and Biddle, 1985), the Malay Basin anticlines appear to be the result of distributed deformation involving a series of *en echelon* half-grabens (Fig. 4.13C). Because the anticlines developed by shortening across the half-grabens, probably as a result of oblique transpressive motion on the bounding faults, their geometry and orientation merely conform to that of the underlying half-grabens. N–S shortening has resulted in reverse dip-slip reactivation of the basement faults (*e.g.* Fig. 4.6), but the amount and sense of the strike-slip component of displacement is impossible to determine from subsurface seismic data because there are no direct kinematic indicators.

4.3 Kinematic Model

The structural evidence, presented in the preceeding sections, suggests that the development of the Malay Basin involved some degree of strike-slip tectonics. The major basement faults in the Basin are oblique to the basin trend, which suggests that the Basin did not form as a simple NW-trending rift by orthogonal NE–SW extension. Minor basin-parallel NW-striking faults are absent except on the flanks (Fig. 4.3), but none can be regarded as major basin-bounding normal faults. One possible explanation for the E-trending basement faults is that the Basin had developed as a pull-apart at a releasing bend of a strike-slip fault (*cf.* Crowell, 1974), as shown schematically in Fig. 4.14. Alternatively, a pull-apart basin may have developed in the overlap zone between two unconnected strike-slip faults (Rodgers, 1980). In the pull-apart model, the E-trending faults at the Basin centre may be interpreted as extensional fractures (normal faults) developed between two crustal blocks, which were pulled apart as a result of local NW–SE transtension at the fault bend. I consider a pull-apart origin as unlikely on the grounds that there are no major marginal strike-slip fault. Pull-apart basins, such

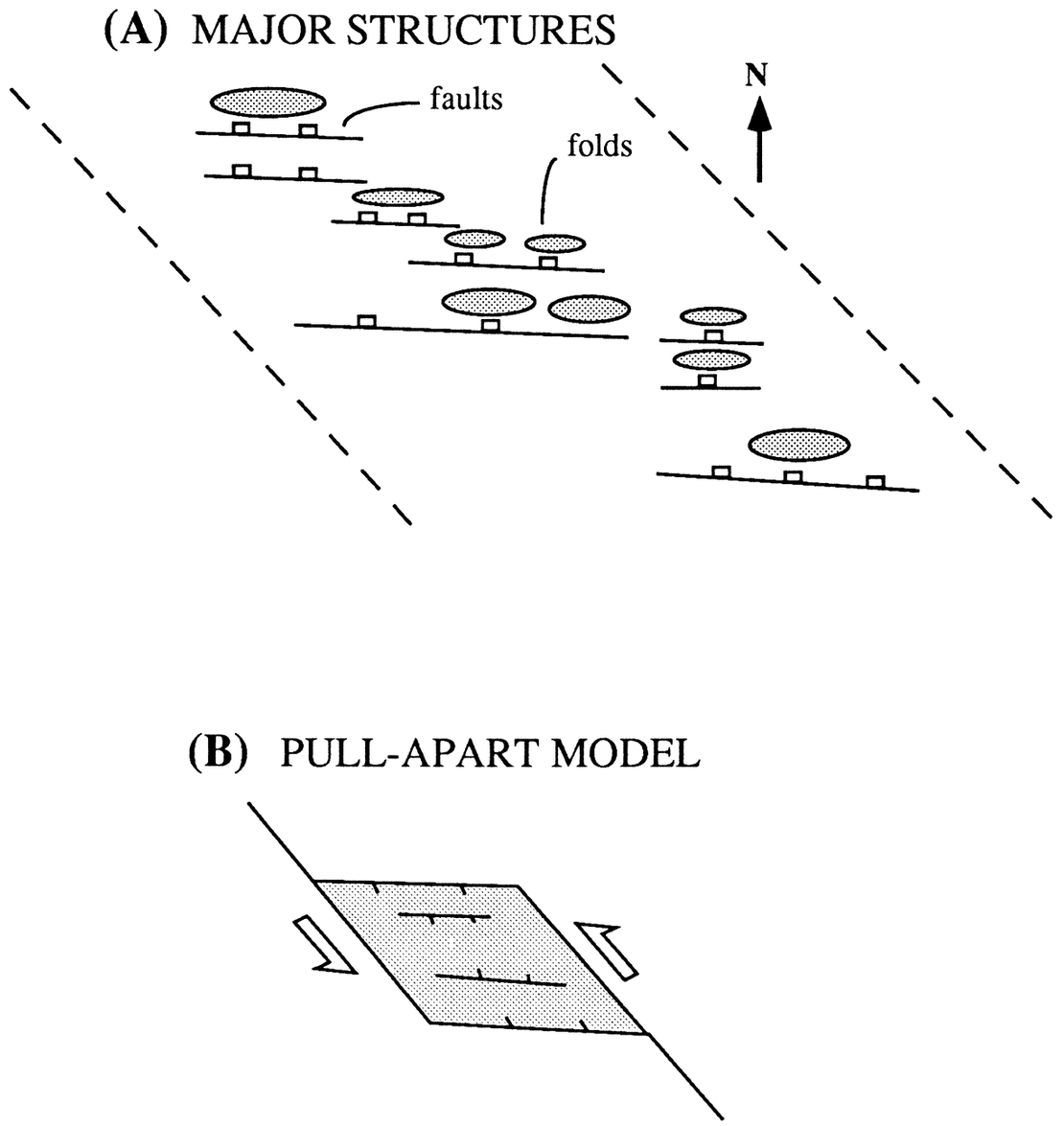

Figure 4.14. Pull-apart model for the Malay Basin. (A) Schematic illustration of *en echelon* array of E-trending faults and associated inversion anticlines. which is not observed. (B) Pull-apart basin formed by extension at a releasing bend of NW-trending strike-slip fault.

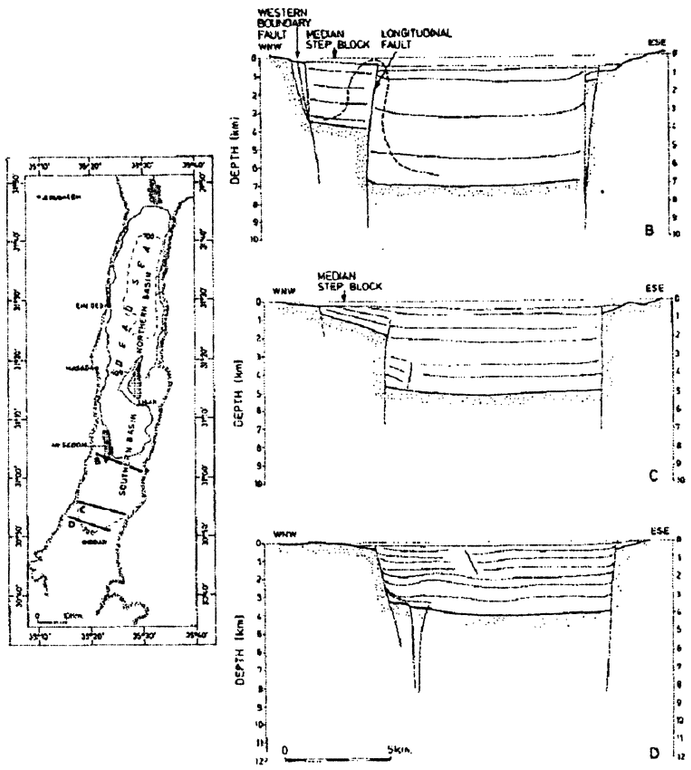

Figure 4.15. Profiles of the Dead Sea pull-apart basin (from ten Brink and Ben-Avraham, 1989), showing the geometry of basin-bounding strike-slip faults.

as the Dead Sea (ten Brink and Ben-Avraham, 1989), commonly, are bounded by major steeply-dipping strike-slip faults (Fig. 4.15). On the contrary, the Basin's flanks are undeformed except for the occurrence of relatively small extensional half-grabens. The gentle inward-tilting of the Basin's flanks seems to indicates, however, a thermal and/or flexural origin for the subsidence of the basin flanks (*cf.* Watts *et al.* 1982) (Chapter 6).

Because of the absence of any major strike-slip faults in the Basin, a more appropriate model would be to describe its formation as being the result of shear deformation over a wide zone rather than along a discrete strike-slip fault. The complex and somewhat rectilinear, basement fault pattern (Fig. 1.4, p. 6), attests to the distributed nature of the deformation, which was controlled probably by pre-existing basement inhomogeneities.

An alternative model is proposed in Fig. 4.16, based on the "block" model of

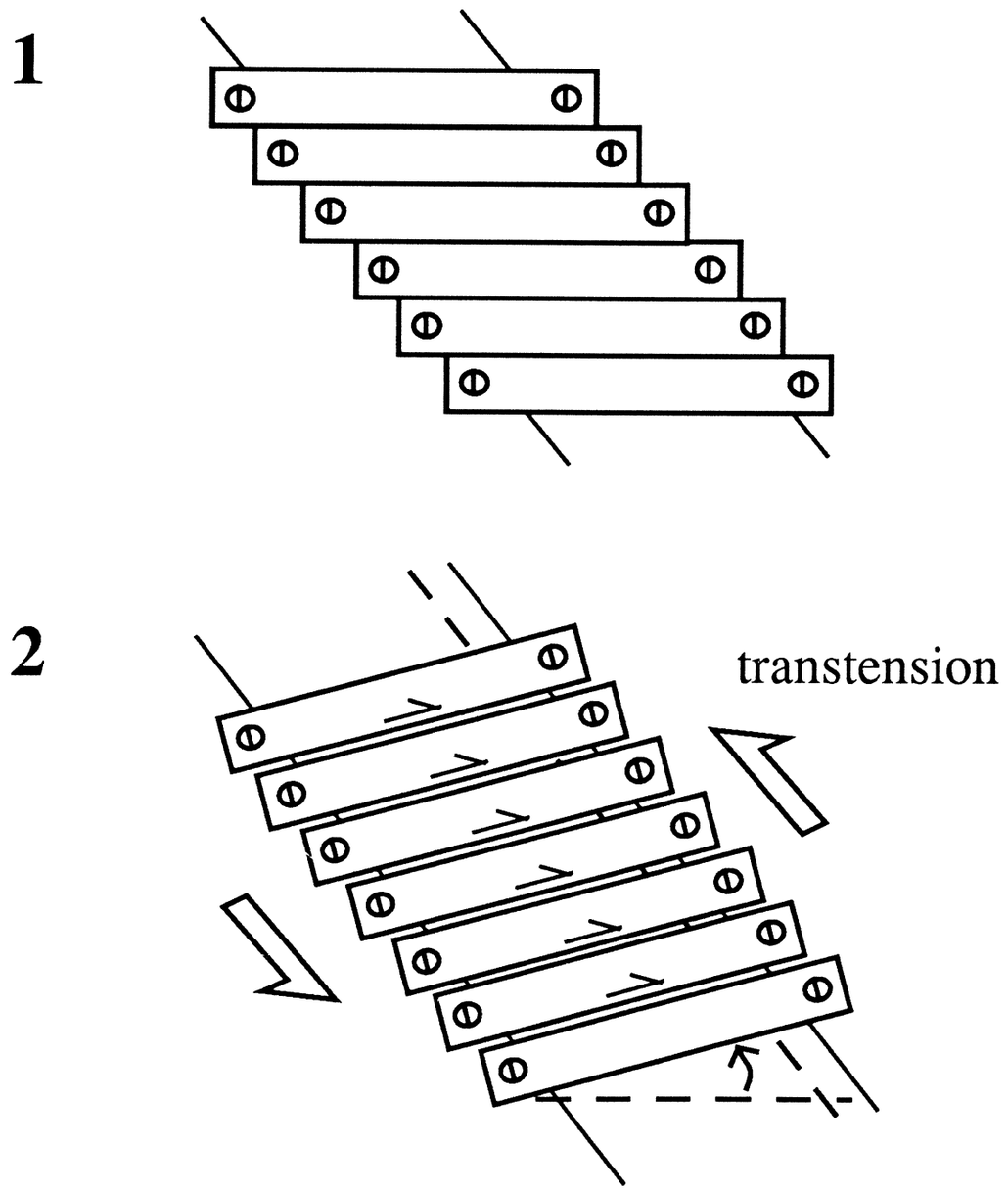

Figure 4.16. Model of transtensional sinistral shear for the formation of the Malay Basin (based on the block model of McKenzie and Jackson, 1986). (1) Initial geometry of shear zone. Crustal blocks, represented by wooden slats, bounded by parallel sets of faults. (2) Sinistral shear: blocks rotate anticlockwise about their fixed ends. Gaps are created by transtensional (dextral) oblique slip along faults between individual blocks. The shear zone width increases during deformation.

McKenzie and Jackson (1986) who applied it originally to the Aegean region. In the Malay Basin, the E-trending basement faults are envisaged as a set of parallel faults oriented obliquely to the zone boundary (compare with Fig. 4.3). During sinistral shearing, the fault-bounded blocks rotate anticlockwise, resulting in the opening of half-grabens between them. The model is very simplistic because it assumes that the ends of the fault-bounded blocks remained attached to the zone boundary during deformation but, yet, are free to rotate about their respective pivots (the screws at the ends of each slat). In nature, deformation at zone boundaries is probably accommodated by distributed deformation (McKenzie and Jackson, 1986). Hence, unlike in the pull-apart model, there is no discrete zone of displacement, such as a marginal strike-slip fault, that are parallel to the deformation zone boundary. This explains the observation that no major strike-slip faults exist on the Basin's flanks.

Because the length of the crustal blocks and of the deforming zone remain unchanged during deformation, half-graben formation is a result of internal rotation of the crustal blocks. The relative motion between any two points on adjacent blocks are always perpendicular to the zone boundary (McKenzie and Jackson, 1986) and hence, the slip on the faults are oblique to their boundaries as they move apart. The strike-slip component of displacement is opposite in sense to that of the external shear couple (Fig. 4.16). The model suggests, therefore, that the half-grabens in the Malay Basin were probably formed by dextral oblique motion between the fault-bounded blocks, as a result of sinistral transtension of the whole zone.

At the beginning of this chapter, seismic evidence (*e.g.* Fig. 4.6) was presented which indicates that half-graben inversion may have been accompanied by significant strike-slip displacement along the half-graben border faults. Figure 4.17 illustrates a possible mechanism by which the half-grabens could have been inverted. If the originally sinistral shear is reversed, so that the crustal blocks rotate clockwise, sinistral oblique slip will occur along their bounding faults. This

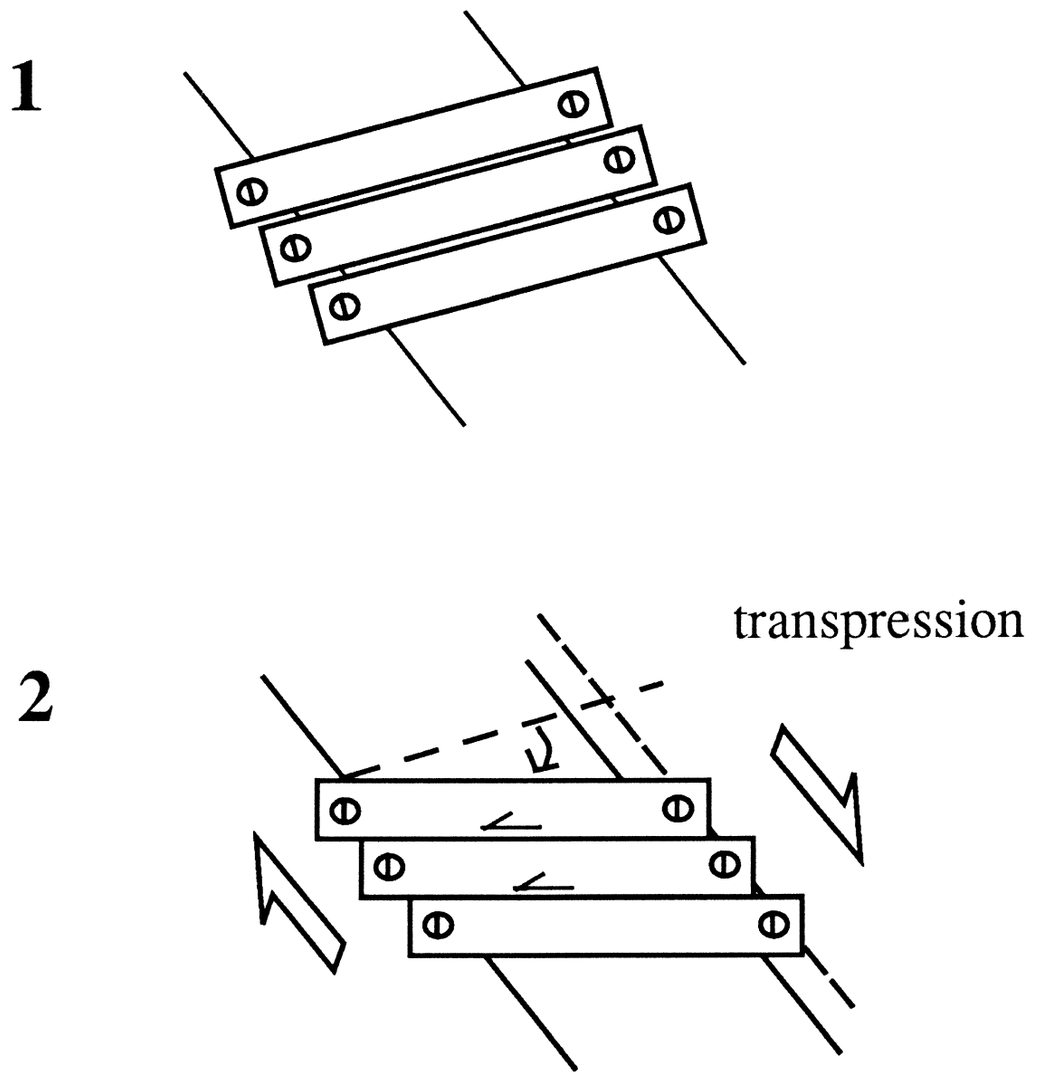

Figure 4.17. Transpressional dextral shear model to explain the inversion in the Malay Basin. (1) Before inversion: geometry as in Fig. 4.16. (2) Reversal of the sense of the external shear couple results in narrowing of the deformation zone, closure of the basin, and deformation of the sedimentary fill.

induces a N-S component of shortening across the grabens, which was observed in seismic sections as reverse dip-slip reactivation of the faults. It is deduced, therefore, the flower structures in the southern Malay Basin were produced by sinistral oblique-slip reactivation of the E-trending half-graben border faults, as a result of reversal in the shear direction.

The timing of inversion has important implications for the kinematic evolution of the Basin because it represents the approximate time at which the stress regime changed from sinistral to dextral. According to ASCOPE (1981), the inversion in the Malay Basin appeared to have started as early as late Oligocene and continued into the Pliocene. Nik Ramli (1986) argued, however, that syn-sedimentary wrench movement responsible for the inversion did not take place until late Miocene to Pliocene times. Here, an independent estimate of the time of basin inversion is obtained from the seismic data. This is done by examining the changes in stratigraphic thickness across the inversion structures. Because the inversion structures are "growth" features, *i.e.* they were formed during deposition, we would expect the thickness of syn-inversion stratigraphic units to decrease towards the crestal region as the depositional surface is being deformed and eroded (Fig. 3.15, p. 66). The timing of the start of inversion can, therefore, be estimated from stratigraphic thickness variation across the structures. The minimum age of inversion would correspond to the time interval represented by the unit that shows no apparent lateral thickness variation.

In the Duyong structure, southern Malay Basin, the postrift stratigraphy is almost completely preserved so that the full history of stratigraphic thickness variation can be observed. Figure 4.18A shows a two-way-time section of the Duyung structure. Cross-structure thickness variation of the units is not readily apparent in this section. However, if the individual thicknesses of the units are plotted with distance across the structure (Fig. 4.18B), we can see more clearly the variation in stratigraphic thickness. As expected, the older units show concave-upwards thickness-distance curves whereas the younger units show convex-upwards curves.

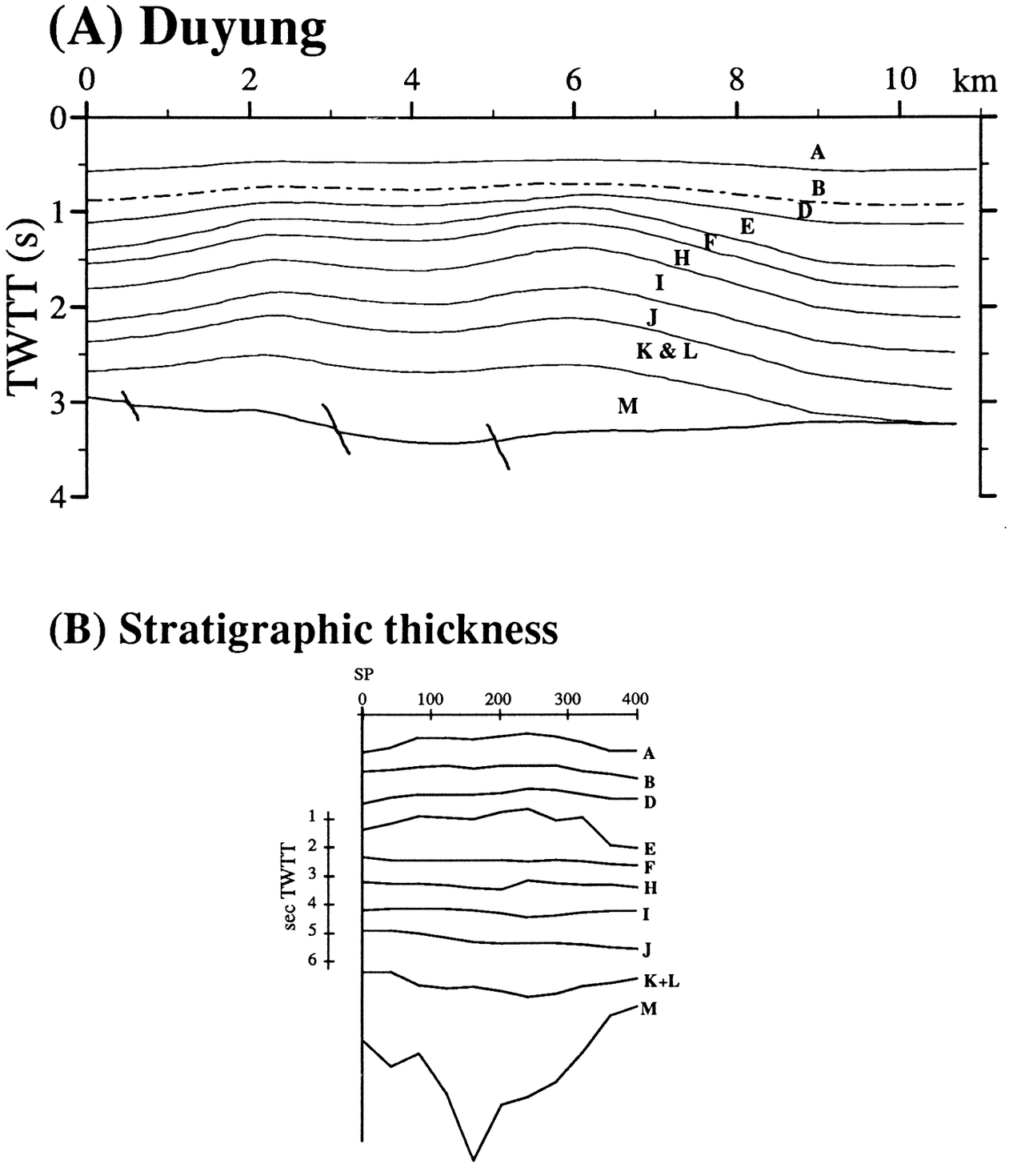

Figure 4.18. Stratigraphic thickness variation and timing of inversion in the Duyung structure. (A) Time section of the Duyung structure showing the stratigraphic units. (B) Plot of thickness of stratigraphic units in (A) to show the variation in thickness with time. Vertical scale is only relative, to show the overall shape of the thickness curves. The switch from concave-upwards (pre-inversion) to convex-upwards (syn-inversion) thickness curves represent the minimum age of the start of inversion, which is ~17–15 Ma (Unit F). Dot-dashed line between units D and B represents the post-inversion regional unconformity.

The flat curve shown by Unit I is interpreted as the "turning point" in the Basin's history, during which subsidence changed to inversion. Based on the age of this unit (Morley *et al.* 1994), the timing of inversion is dated as 17–15 Ma, corresponding to approximately the early-middle Miocene boundary.

4.4 Conclusion

A kinematic model is proposed whereby the Malay Basin was formed by transtension of a NW-trending sinistral shear zone, which contains pre-existing E-trending basement faults. During deformation, anticlockwise rotation of the fault-bounded blocks resulted in dextral oblique slip along the faults, producing a series of E-trending half-grabens. The resulting basin geometry (Fig. 4.19) is similar to that conceived by Beauchamp (1988) for the Es Çour Basin in the High Atlas of Morocco, except that the Malay Basin is not bounded by margin parallel strike-slip faults. The Malay Basin may be classified as a "transrotational" basin (Ingersoll and Busby, 1995; Nilsen and Sylvester, 1995), which developed as a result of rotation, about vertical axes, of crustal blocks within a sinistral shear zone.

Using this model, the formation of compressive anticlines over the half-grabens is explained as being the result of a reversal in the sense of shear. The inversion and, hence, the switch from sinistral to dextral shear, occurred sometime during the early-middle Miocene (~15–17 Ma). Dextral shear resulted in transpressive sinistral oblique-slip reactivation of the E-trending basement faults and the formation of anticlines over the inverted half-grabens.

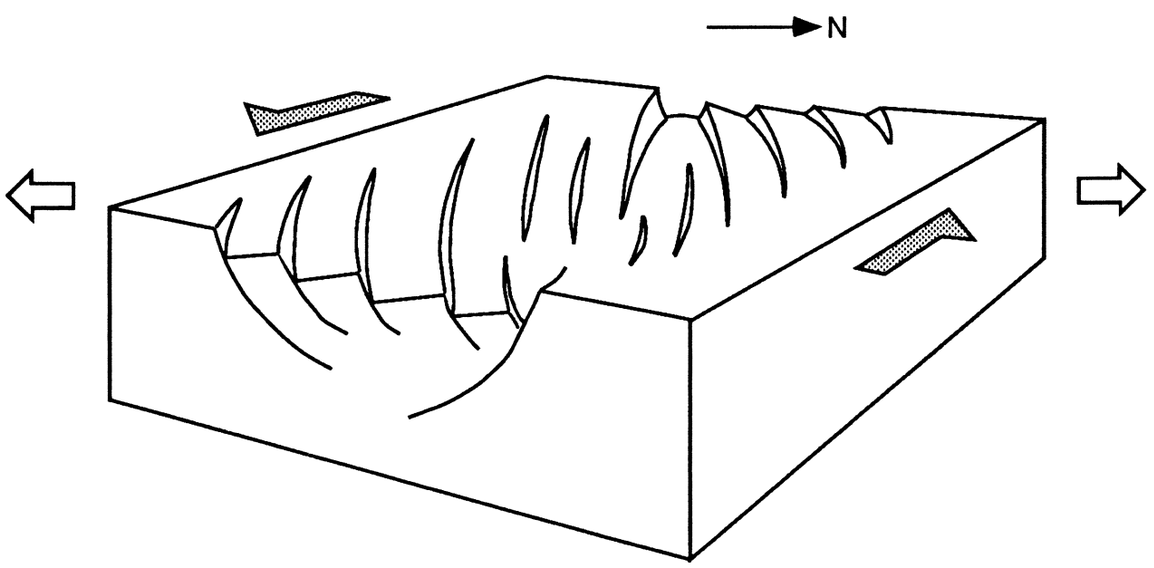

Figure 4.19. Block diagram showing the possible geometry of faulting in the Malay Basin during the extensional phase.

Chapter 5

Gravity Anomalies and Isostasy

The formation of sedimentary basins is primarily a consequence of isostatic adjustment of the lithosphere in response to a tectonic driving force and sediment loading. In the simple model of lithospheric stretching (McKenzie, 1978), subsidence is a direct result of homogeneous thinning of the lithosphere, in addition to the thermally-induced subsidence, as it tries to achieve isostatic equilibrium. Sediment filling the space created by crustal thinning acts as a load that enhances subsidence.

Because of the density contrasts that exist between the basin fill (*i.e.* sediment and/or water), the crust, and the mantle, gravity anomalies over sedimentary basins are sensitive indicators of the state of isostasy and may be used to infer the origin of basins. Theoretically, stretched (rift) basins formed by lithospheric extension have, depending on the width of the stretched zone, generally positive free-air anomalies because of the presence of dense mantle beneath the thinned crust, whereas strike-slip or "thin-skinned" extensional basins have negative anomalies that are isostatically uncompensated (Fig. 5.1). Basins that form by a mechanism that does not involve thinning of the whole lithosphere, *e.g.* some strike-slip basins, should therefore have a different isostatic signal from that of stretched basins.

The form of the gravity anomalies depends on the *flexural rigidity* of the lithosphere, which determines the behaviour of the lithosphere in response to loading. Flexural rigidity is a parameter that describes, essentially, the "stiffness" of the

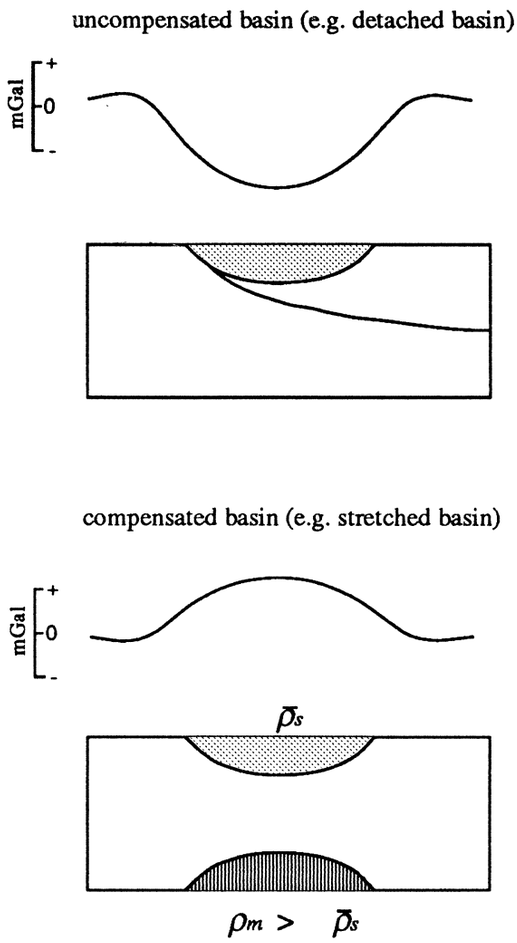

Figure 5.1. Gravity anomalies over hypothetical basins. (Top) Basins that form by crustal extension without mantle involvement are, generally, isostatically uncompensated, and have negative anomalies. (Bottom) Depending on the relative widths of basin and of the compensating mantle, stretched (rift) basins have, generally, positive anomalies because of mantle contribution to the density contrast.

lithosphere; a high-rigidity lithosphere will result in a very small deflection for a given load contrasted to a low-rigidity lithosphere. When a lithosphere has finite rigidity, loads are supported regionally as opposed to locally (Fig. 5.2). In the Airy model of isostasy, the load is supported by the buoyancy of the underlying fluid asthenosphere, whereas in the flexural model the load is supported by the rigidity of the plate.

It is common practice to quantify flexural rigidity, D, in terms of the *effective elastic thickness*, T_e, of the plate which is given by the relationship

$$D = \frac{ET_e^3}{12(1-\nu^2)} \tag{5.1}$$

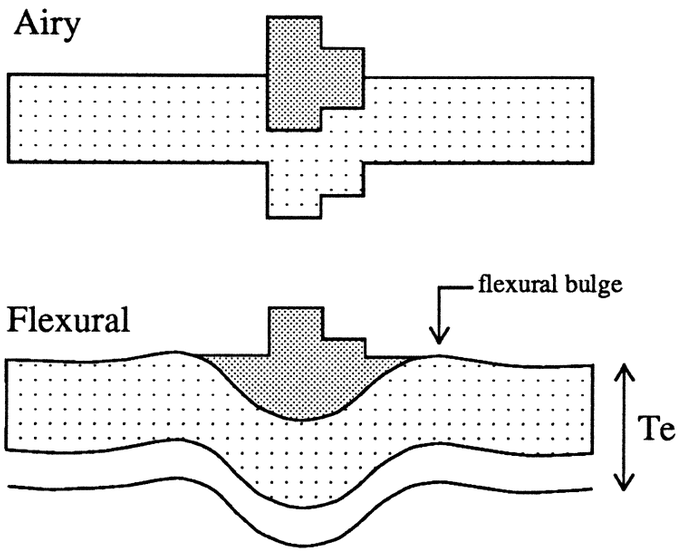

Figure 5.2. Schematic illustration of models of isostatic compensation; Airy *vs* flexural isostasy. Redrawn from Karner and Dewey (1989).

where E is Young's modulus and ν is Poisson ratio. The effective elastic thickness of the lithosphere may be viewed as the thickness *equivalent* to that of a perfectly elastic plate having the same physical properties. Because the state of isostasy in basins is governed by the way in which the loads are supported, whether locally (Airy-type) or regionally (flexural), gravity modelling can be used to constrain the effective elastic thickness T_e of the lithosphere.

In this chapter, free-air gravity anomaly and sediment thickness data from the Malay and Penyu Basins are used to investigate the state of isostasy of these basins. The technique of backstripping (Watts and Ryan, 1976) is used to isolate the effect of sediment loading from the total subsidence, which is represented by the sediment thickness, to obtain the subsidence caused by tectonic processes. By assuming Airy or flexural isostasy, the sediment thickness along selected profiles were "backstripped" to restore the crustal structure at the time of rifting, and for investigation of the role of flexure in the subsidence of the Basins. To determine the mechanism of isostatic compensation and constrain T_e, gravity anomalies were calculated using simple models of crustal thinning and sediment loading, and compared with the observed free-air anomalies. Three profiles across the Malay Basin and one across the Penyu Basin (Fig. 5.3) were modelled.

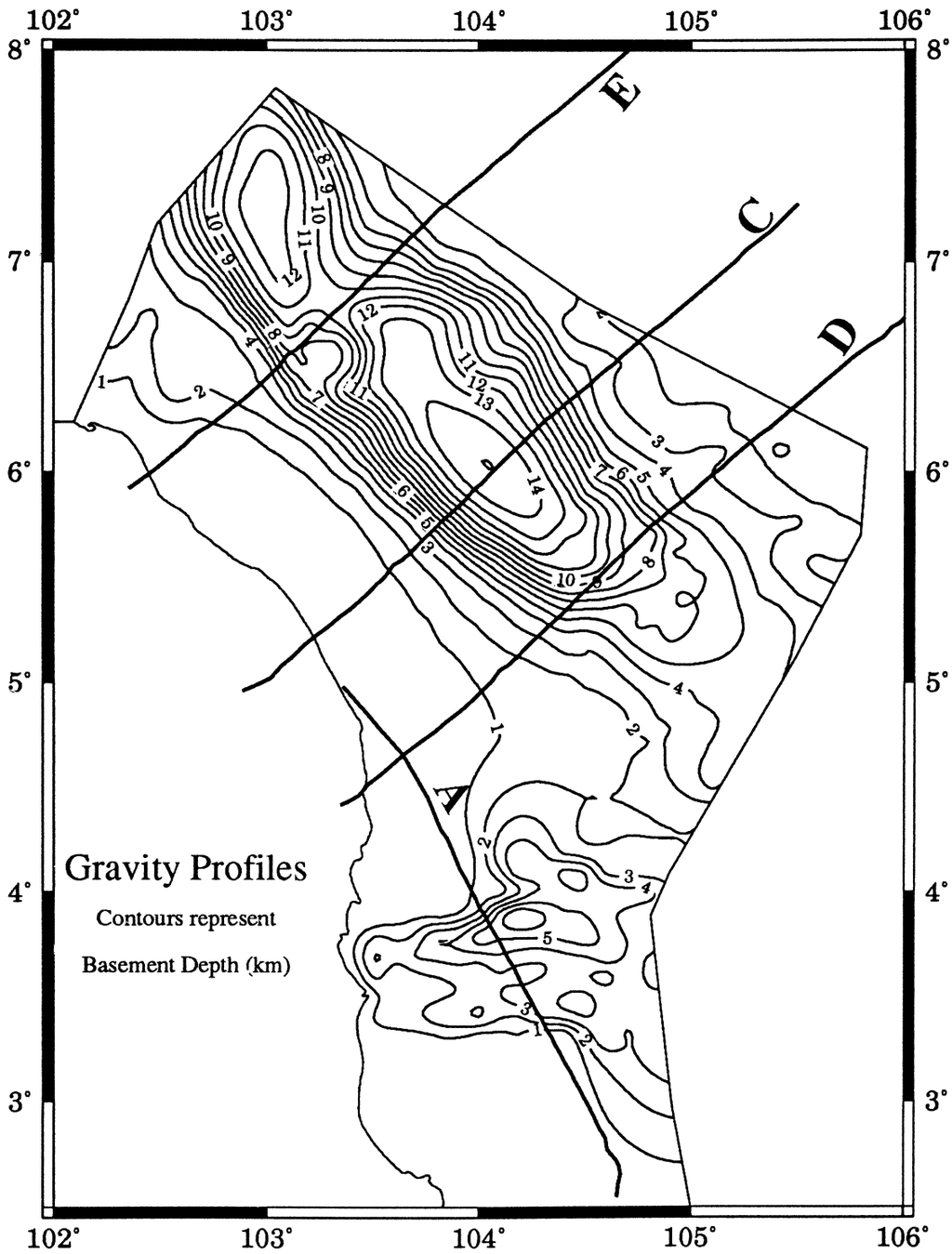

Figure 5.3. Location of profiles used in the gravity modelling. The contours represent the depth to pre-rift basement, *i.e.* the basin depth, based on a compilation of unpublished basement depth map for the Malay Basin and the Horizon 8 depth map (Fig. 3.4, p. 48) for the Penyu Basin. The Malay Basin data are based on a 1985 compilation by Esso Malaysia (obtained from PETRONAS). Depth contoured at 1 km intervals. Note that the maximum depth of 14 km in the Malay Basin is somewhat greater than that previously published by Hamilton (1979) (~10 km).

5.1 Data Preparation

To analyse the tectonic subsidence, the total sediment thickness in the Malay and Penyu Basins was compiled from various sources. The data for the Penyu Basin was obtained from the present study (Chapter 3) while the data for the Malay Basin is based on a compilation of unpublished maps supplied by PETRONAS. Figure 5.3 shows the basement depth map of the study area based on this compilation. The map shows that the Basin is up to 15 km deep. Water depth in the area is generally less than 70 m. Intuitively, we would expect a very large amplitude free-air gravity anomaly over the Basin; negative if totally uncompensated or positive otherwise. Free-air gravity data of the Southeast Asian region has been compiled by Watts *et al.* (1978) in the Geological Society of America Map MC-25. The compilation included a substantial amount of data from the South China Sea but only a limited number of gravity measurements from the Gulf of Thailand and offshore Peninsular Malaysia. The data of Watts *et al.* (1978) shows a large region of negative gravity anomaly of about -20 mGal over the Gulf of Thailand and offshore Peninsular Malaysia where the major Tertiary basins (Malay and Thai Basins) are situated. This is an interesting observation, and not what we would expect for a 15 km-deep sediment-filled basin. The thick sediment pile requires large amount of crustal thinning, which should give rise to a significantly positive anomaly as a result of the mantle contribution to the gravity effect. On the other hand, if the Basin is a pure strike-slip basin, a large negative would result. In the North Sea, for instance, a $+20$ mGal free-air anomaly occurs over the Viking and Central Grabens, where the crust has been thinned by a factor < 2 (see Thorne and Watts, 1989, fig. 15). The Moray Firth Basin, which is probably a strike-slip dominated basin (Roberts *et al.*, 1990), shows a large negative anomaly of up to -40 mGal.

The dataset published by Watts *et al.* (1978), some of which were supplied by the U.S. Defence Mapping Agency (DMA), comprises point measurements of bathymetry and free-air gravity anomalies. For this study, a digital copy of the

DMA dataset, covering the whole of Southeast Asia, was obtained from Dr. Steven Harder (University of Texas at El Paso). Because of the sparse gravity data in the study area, the DMA dataset is supplemented with data derived from satellite altimetry. Sandwell and Smith (1992) have, recently, compiled and published a gridded database of free-air anomalies of the oceans derived from satellite data, including SEASAT, GEOSAT, and ERS-1. For this study, a portion of Sandwell and Smith's dataset was extracted over the study area, between 2°-10°N and 102°–106°E. Figure 5.4 shows the free-air anomaly map of the area based on that gridded data. To show the overall shape of the anomaly, the data have been regridded onto 1 min × 1 min blocks and smoothed by averaging over 20 min blocks. The map shows two regions of negative/low gravity anomaly: one over the Malay Basin with maximum amplitude of ~25 mGal, and another corresponding with the Penyu Basin with a lower amplitude of ~5 mGal. For the gravity modelling, several profiles were chosen along which the gravity and sediment thickness data were sampled.

5.2 Modelling Technique

5.2.1 Flexural Backstripping

To analyse the tectonic subsidence/uplift that occurs during the development of sedimentary basins, we need to isolate and remove the effects of sediment loading. The subsidence/uplift obtained after these effects have been removed represents the tectonically-driven subsidence. Flexural (or 2D) backstripping is a technique used to restore basement depth by removing the sediment loads. However, unlike in one-dimensional (1D) backstripping (Watts and Ryan, 1976; Steckler and Watts, 1978), which uses an Airy isostatic scheme when unloading the basement at a particular point, such as a well location, flexural backstripping involves the removal of sediment loads by flexurally unloading the basement along a profile

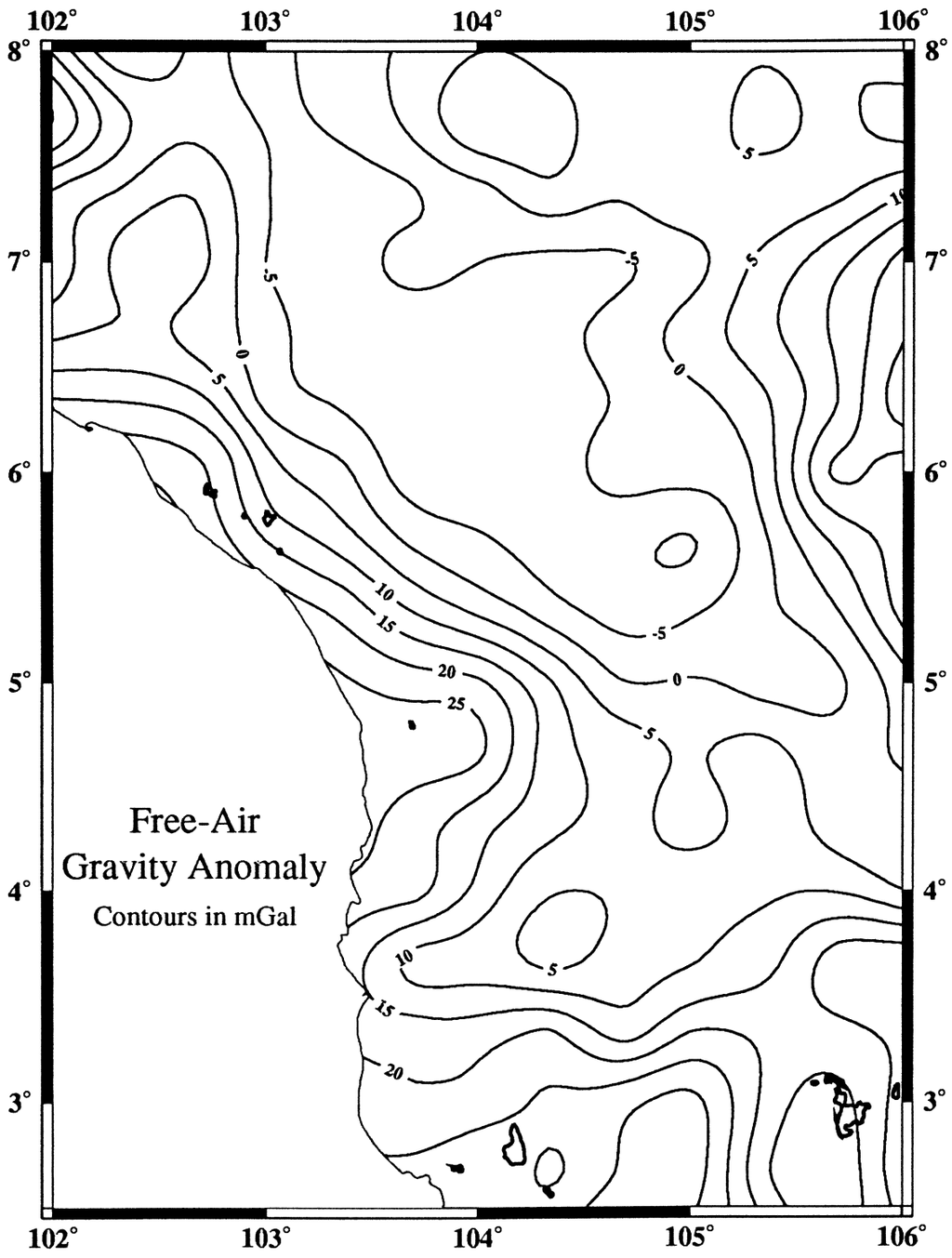

Figure 5.4. Free-air gravity anomaly map of study area based on the satellite-altimeter data published by Sandwell and Smith (1992). Gravity contours in mGal. To show the overall form of the anomaly, the original data have been smoothed over a 20-minute grid.

across the basin. The flexural backstripping technique has been described by Watts (1988), and is briefly explained below.

To flexurally unload the sediment from the basement, we need to compute the flexure of the lithosphere due to the sediment load. This is done by solving the fourth-order differential equation that relates flexure, w, of a thin elastic plate due to a vertical load distribution, $q(x)$, as a function of horizontal distance, x (Turcotte and Schubert, 1982; Watts *et al.*, 1982)

$$D\frac{\partial^4 w(x)}{\partial x^4} + (\rho_m - \rho_{infill})\, g\, w(x) = q(x) \tag{5.2}$$

where ρ_m, ρ_w, and ρ_{infill} are densities of mantle, water, and the material filling the deflection, respectively, and g is gravitational acceleration. Flexural rigidity, D, is assumed to be independent of x, *i.e.* it does not change laterally. For simple load geometries, and given the appropriate boundary conditions, equation 5.2 may be solved algebraically (Turcotte and Schubert, 1982). Consider, for example, a simple cosinal load of the form $y\cos(kx)$, where y is the height of the load and k is the wavenumber, which is related to load wavelength, λ, by $k = 2\pi/\lambda$. We would expect the flexure solution to be harmonic also, and is given by:

$$w(x) = w_o \cos(kx) \tag{5.3}$$

where w_o represents the flexure at $x = 0$, found by substituting 5.3 into 5.2 and solving for w:

$$w_o = \Phi\, y \left[\frac{\rho_s - \rho_w}{\rho_m - \rho_{infill}}\right] \tag{5.4}$$

ρ_s being the density of the load and Φ is the *basement response function*, which governs the flexural response of the lithosphere for a given flexural rigidity and load wavelength, and is given by

$$\Phi = \left[1 + \frac{Dk^4}{(\rho_m - \rho_{infill})\, g}\right]^{-1} \tag{5.5}$$

For arbitrary load shapes, an approximate solution is obtained in the wavenumber domain by taking the Fourier transform of both sides of 5.3. For example, if

the load is specified by some function $y(x)$, the load distribution represented in the wavenumber domain is thus $\mathrm{Q}(k) = \mathcal{F}\{(\rho_s - \rho_w)\, g\, y(x)\}$, where $\mathcal{F}$ is the Fourier transform operator. The solution to equation 5.2 in the wavenumber domain then becomes

$$\mathrm{W}(k) = \Phi(k)\ \mathrm{Y}(k) \left[\frac{\rho_s - \rho_w}{\rho_m - \rho_{infill}}\right] \tag{5.6}$$

where $\mathrm{W}(k)$ and $\mathrm{Y}(k)$ are the flexure and load in the wavenumber domain, respectively. To obtain the flexure, w, in the space domain, we take the inverse Fourier transform ($\mathcal{F}^{-1}$) of the product of the basement response function and the load spectrum

$$w(x) = \mathcal{F}^{-1}\left\{\Phi(k)\ \mathrm{Y}(k) \left[\frac{\rho_s - \rho_w}{\rho_m - \rho_{infill}}\right]\right\} \tag{5.7}$$

The application of equation 5.7 in flexural backstripping is described below. Equation 5.5 shows that the lithosphere behaves rigidly for short-wavelength loads ($\lambda \ll y$) because when k is large, $\Phi(k)$ is small and, hence, there is little deflection. For wide loads, *i.e.* when λ is large and, hence, $k \to 0$, the rigidity term in the basement response function (equation 5.5) becomes insignificant and $\Phi(k) \to 1$, so that the flexural behaviour approaches that of Airy isostasy. In an Airy-type situation, therefore, the flexure solution given by equations 5.3 and 5.4 reduces to

$$w = y\left(\frac{\rho_s - \rho_w}{\rho_m - \rho_{infill}}\right)$$

The total depth that results from loading is thus $S^* = y + w$, which depends on the value of ρ_{infill}. To find the water-filled deflection due to the total load S^*, we replace y by S^* in the above equation and assume $\rho_{infill} = \rho_w$, and obtain

$$w = S^*\left(\frac{\rho_s - \rho_w}{\rho_m - \rho_w}\right)$$

Because the total sedimentary thickness, S^*, is the sum of the load and the flexure, *i.e.* $S^* = y + w$, the water-filled tectonic subsidence is given by $y = S^* - w$. Hence,

$$\begin{aligned} y &= S^* - S^*\left(\frac{\rho_s - \rho_w}{\rho_m - \rho_w}\right) \\ &= S^*\left(\frac{\rho_m - \rho_s}{\rho_m - \rho_w}\right) \end{aligned} \tag{5.8}$$

which is the water-filled subsidence for Airy isostasy (Steckler and Watts, 1978). Hence, to calculate the water-filled tectonic subsidence by flexural backstripping, we need to compute, first, the flexure due to the total sediment load using equation 5.7, with $\rho_{infill} = \rho_w$, and then subtract the flexure from the total sediment thickness (Fig. 5.5A).

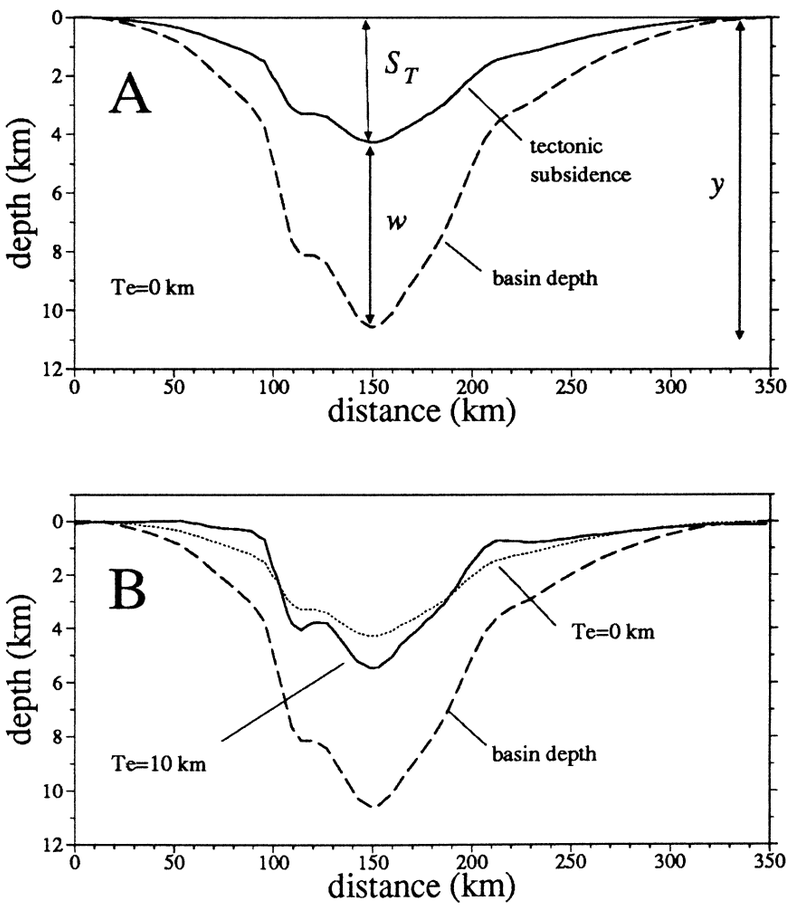

Figure 5.5. Examples of flexural backstripping of (A) sedimentary basin filled with sediment of thickness y to obtain the tectonic subsidence, S_T. w represents the flexure due to sediment loading. $T_e = 0$ km. (B) the same basin in A backstripped using $T_e = 10$ km (solid line) for comparison with subsidence for $T_e = 0$ km (dotted line). In both examples, sediment density, ρ_s, is 2400 kg m^{-3} and $\rho_{infill} = \rho_w = 1030$ kg m^{-3}.

Suppose that the sediment thickness is now $y(x)$, the water-filled tectonic subsidence, S_T, is given by

$$S_T(x) = y(x) - \mathcal{F}^{-1}\left\{\Phi(k)\,\mathrm{Y}(k)\left[\frac{\rho_s - \rho_w}{\rho_m - \rho_w}\right]\right\} + W_d(x) \qquad (5.9)$$

where W_d is the the present-day water depth. For a basin fill comprising n layers, backstrippping may be done layer by layer to obtain the total tectonic subsidence, thus

$$S_T(x) = \sum_{i=1}^{n} \left(y_i(x) - \mathcal{F}^{-1} \left\{ \Phi(k)\, \mathrm{Y}_i(k) \left[\frac{\rho_{si} - \rho_w}{\rho_m - \rho_w} \right] \right\} \right) + W_d(x) \qquad (5.10)$$

where $y_i(x)$ and $\mathrm{Y}_i(k)$ are the thicknesses of layer i in the space and wavenumber domain, respectively, and ρ_{si} is its density.

In flexural backstripping, the flexural rigidity, D, is determined by a T_e value in equation 5.1, using the constants listed in Table 5.2 (p. 196). Two-dimensional Airy backstripping is equivalent to flexural backstripping with $T_e = 0$ (Fig. 5.5A). When $T_e > 0$, the tectonic subsidence is greater than that when $T_e = 0$ km at the centre of the basin while the opposite is true at the margins (Fig. 5.5B).

5.2.2 Modelling Procedure

The gravity modelling procedure follows the method of Watts (1988). For the purpose of calculation, the gravity anomaly of a 2D basin is considered to be the sum of anomalies resulting from crustal thinning ("rifting anomaly") and from sedimentation ("sedimentation anomaly") (Fig. 5.6A). The rifting anomaly is associated with density contrasts resulting from crustal thinning, and is the combined gravity effect of the water-filled subsidence and the Moho topography at the end of rifting. The sedimentation anomaly is the sum of gravity effects of sediment replacing water and loading the crust. The calculation is done as follows:

1. Compute the tectonic subsidence, S_T, by flexural backstripping the sediment thickness. The tectonic subsidence represents, essentially, the water depth at the end of rifting.

2. Restore the crustal structure at the end of rifting. The depth to the "backstrip Moho", z_m, is defined as the base of the restored crustal structure in

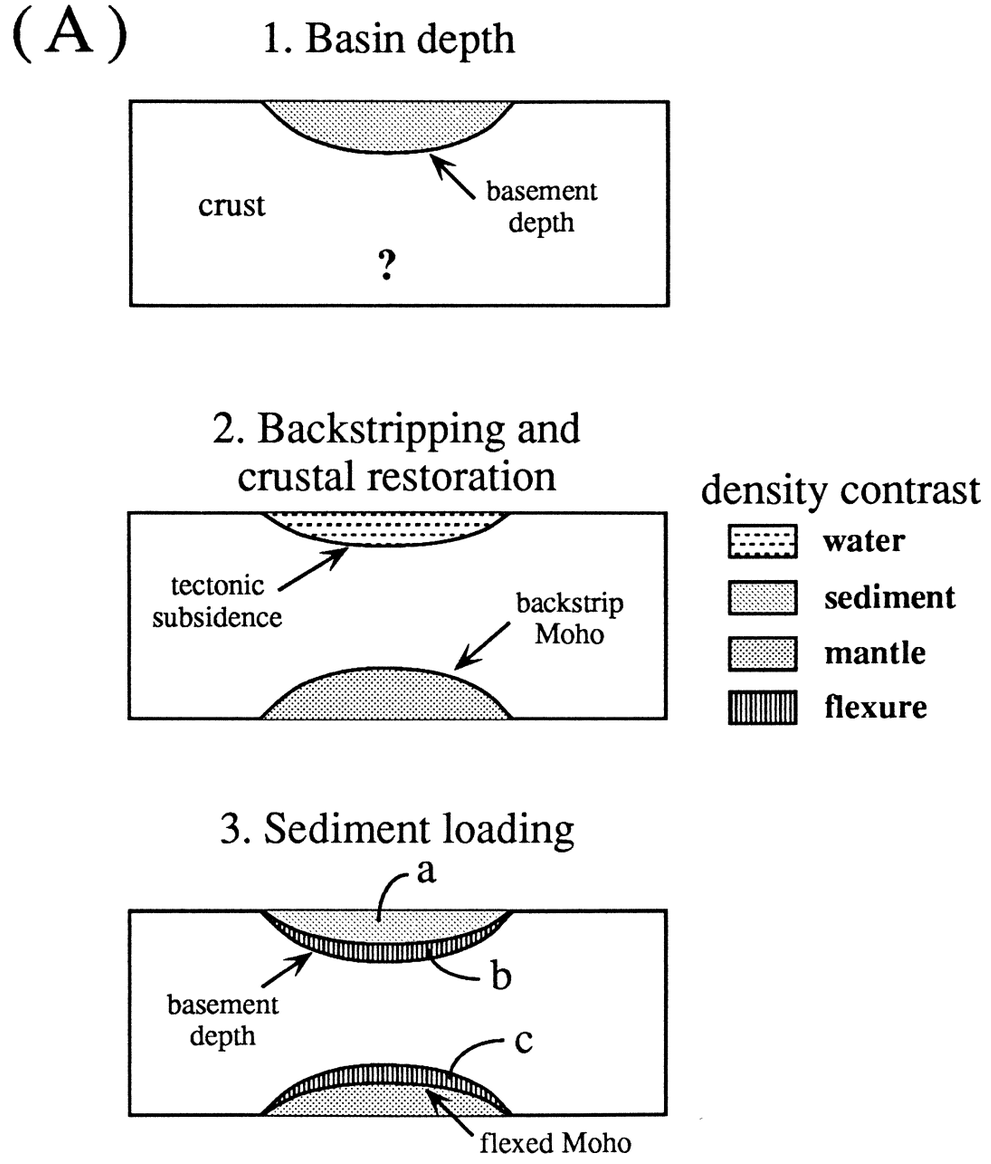

Figure 5.6. Procedure for the calculation of gravity anomaly of a hypothetical rift basin. (A) Backstripping and crustal restoration: **1.** Starting basin configuration. **2.** Tectonic subsidence obtained by backstripping, representing water depth at end of rifting. **Backstrip Moho** represents the Moho depth at the end of rifting in the absence of sediment loading (Watts and Torné, 1992) and is calculated by assuming Airy isostasy. **Rifting anomaly** is the sum of gravity effects of water and mantle. **3.** Sediment loading: replace water with sediment and compute flexure of basement and Moho. The **flexed Moho** is the backstrip Moho that has been depressed as a result of sediment loading (Watts and Torné, 1992). **Sedimentation anomaly** computed from the density contrasts between (a) sediment and water, (b) sediment and crust, and (c) crust and mantle. Continued next page...

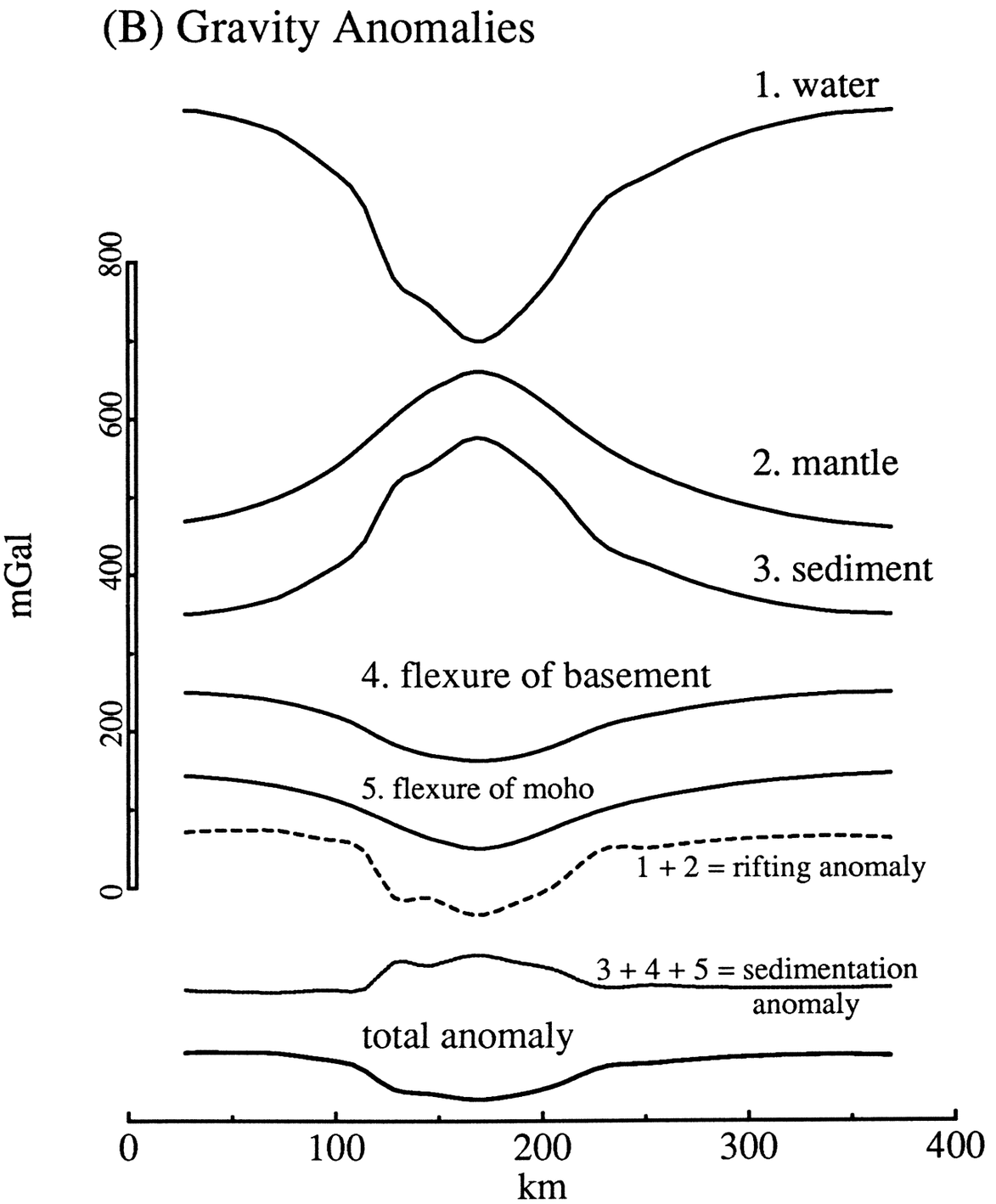

Figure 5.6 cont. (B) Example of the results of modelling Line E, to show the general form of the various anomalies calculated through the steps described in Fig. 5.6A. The vertical scale in mGal does not represent any one curve but is shown to indicate the relative magnitudes of the different components of the total anomaly. Notice that the main contribution comes from water (*i.e.* tectonic subsidence), mantle, and sediment.

the absence of sediment loading, which represents the Moho depth at the time of rifting (Watts and Torné, 1992). Without prior knowledge of the flexural rigidity of the lithosphere, we make an initial assumption that the lithosphere is infinitely weak ($T_e = 0$) and, hence, any load is compensated locally. Also, because T_e is assumed to be zero during rifting, the flexural effect of lithospheric necking (Braun and Beaumont, 1989; Kooi *et al.*, 1992) is ignored. Assuming Airy isostasy, therefore, z_m is obtained by balancing the water-loaded crust with a column of unstretched crust of thickness y_c and uniform density ρ_c:

$$z_m = y_c - S_T \left[\frac{\rho_c - \rho_w}{\rho_m - \rho_c} \right] \tag{5.11}$$

3. The rifting anomaly, ΔG_R, is calculated by adding the negative gravity effect of water filling the basin and the positive gravity effect from the backstrip Moho topography.

4. Sediment is "put back" into the basin and the "sedimentation anomaly", ΔG_S, is calculated from the effects of the sediment displacing the water and the flexure of the basement and Moho. The gravity effect of the sediment is positive, whereas the effects flexure of the sediment-basement interface and the backstrip Moho are negative (Fig. 5.6B).

5. The total anomaly is $\Delta G_{calc} = \Delta G_R + \Delta G_S$.

Because of the many steps involved in the gravity calculation, the above procedure was implemented in a single computer program that combines flexural backstripping, crustal restoration, and gravity calculation, so that input variables such as T_e, sediment density *etc.* can be changed easily from one model to another. To quantify the "fit" between the observed and calculated anomalies, we use the standard deviation (σ_g) of the calculated with respect to the observed gravity anomaly (ΔG_{obs}):

$$\sigma_g = \sqrt{\frac{\Sigma(\Delta G_{calc} - \Delta G_{obs})^2}{n}} \tag{5.12}$$

where n is the number of points along the profile. The best-fit calculated anomaly is one that shows the minimum σ_g.

In the modelling technique described above, we are making some simplifying assumptions about the process of basin formation. Basically, the technique separates the different components of the gravity anomaly (Fig. 5.6B), which are assumed to be the result of two main processes during basin evolution — crustal thinning and sediment loading. The tectonic subsidence, obtained by backstripping, is assumed to be solely the result of local (Airy) isostatic adjustment following instantaneous crustal thinning (rifting). This is done to simplify the calculation when restoring the crustal structure at the time of rifting (in step 2 above). The use of Airy compensation implies that the lithosphere is infinitely weak (*i.e.* no rigidity) during rifting, as suggested by some studies of passive margins (Watts, 1988; Fowler and McKenzie, 1989), although other workers have found higher T_e values in places such as the East African Rifts (Ebinger *et al.*, 1991).

The assumption of Airy isostasy ignores the fact that the density of mantle changes following rifting. Watts and Torné (1992) have shown that, for a young rift basin whose age is less than the thermal time constant of the lithosphere (~60 Ma), the backstrip Moho depth calculated using the Airy scheme (equation 5.11) will always be overestimated. This is because the lithosphere is still cooling and has not reached its equilibrium thermal state. Because the Malay Basin is only ~35–40 Ma old and could still be undergoing thermal subsidence, the backstrip Moho depth calculated using the Airy model may be deeper than expected. Figure 5.7 shows the relationship between tectonic subsidence and the backstrip Moho depth, calculated using (1) Airy model with a "normal" mantle density (ρ_m = 3330 kg m^{-3}) and (2) the thermal model of McKenzie's (1978) evaluated for 35 and 40 Ma-old basins— considered to be the minimum and maximum ages of the Malay and Penyu Basins. The same densities for water and crust (ρ_w = 1030 kg m^{-3}, ρ_c = 2800 kg m^{-3}) were assumed in all the calculations. The diagram

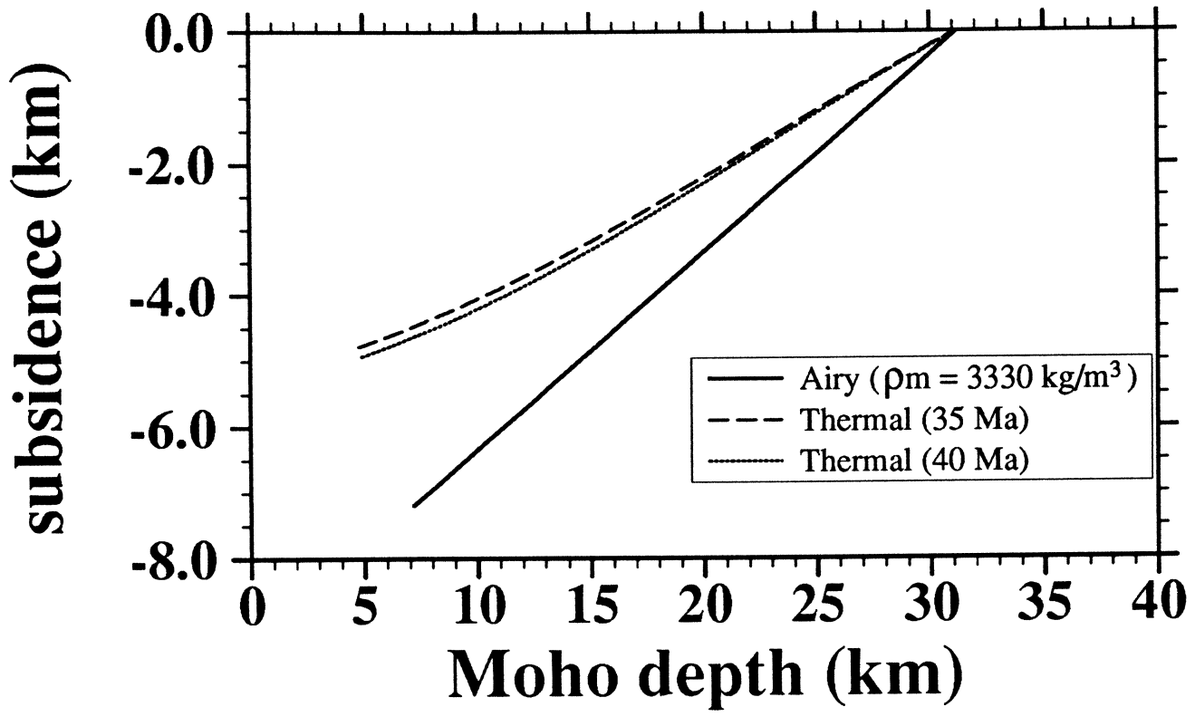

Figure 5.7. Plot of tectonic subsidence vs depth to Moho based on Airy (mantle density ρ_m = 3330 kg m^{-3}) and thermal models of crustal thinning. The latter has been evaluated for 35 and 40 Ma, representing the minimum and maximum ages of the Malay and Penyu Basins.

shows that, given the tectonic subsidence, the backstrip Moho depth based on the thermal model is always shallower than that based on the Airy model. There is no significant difference between the two thermal models based on different basin ages. Hence, if thermal isostasy is incorporated in the gravity modelling, the mantle contribution to the total anomaly will be greater because the mantle density would be less than in the Airy case.

We assume, also, that all the sedimentation occurs instantaneously following rifting. Although, it is sufficient to consider the final rifting anomaly, corresponding to the end of rifting, the sedimentation anomaly should, ideally, be calculated incrementally because of possible changes in load geometry and loading response of the lithosphere during the postrift phase. This is important, particularly, in passive margins, where lateral progradation of sediment is an important process

(Watts and Marr, 1995). The assumption made in this study is justified because we are dealing with a roughly symmetrical rift basin whose simple geometry does not seem to have changed significantly during its postrift evolution.

5.2.3 Gravity Modelling

Gravity modelling in two dimensions involves, essentially, calculating the sum of the gravity effects of all known density contrasts at depth and comparing the calculated anomaly with the observed. In the simplest situation, the density contrasts associated with a rift basin occur in two places: one at the surface resulting from the basin fill (sediment and water) and the other at the base of the crust because of the Moho topography (Fig. 5.1). The most common and simplest method used to calculate the gravity effect of a constant-density 2D body is the line-integral method (Talwani *et al.*, 1959; Bott, 1973), in which the body is determined as a series of polygons whose sides are specified by the x-z coordinates of the basement or Moho.

In this study, a line-integral program based on Talwani's method was used in the gravity modelling. However, to incorporate the effects of non-uniform density constrasts, *e.g.* due to sediment compaction, the gravity calculation technique has to be modified. For this study, a Fast Fourier Transform (FFT) technique based on Parker (1972) and modified by Cowie and Karner (1990) was used in the calculation of the gravity effect due to the sediment filling the basin. Calculations of the gravity effects resulting from Moho topography and flexure of the basement and Moho were carried out with the line-integral method. Figure 5.8 compares the results of the two calculation techniques applied to a hypothetical basin. The figure shows that the two methods gave almost the same result when uniform density is assumed; the maximum discrepancy between the two is < 2.5 mGal.

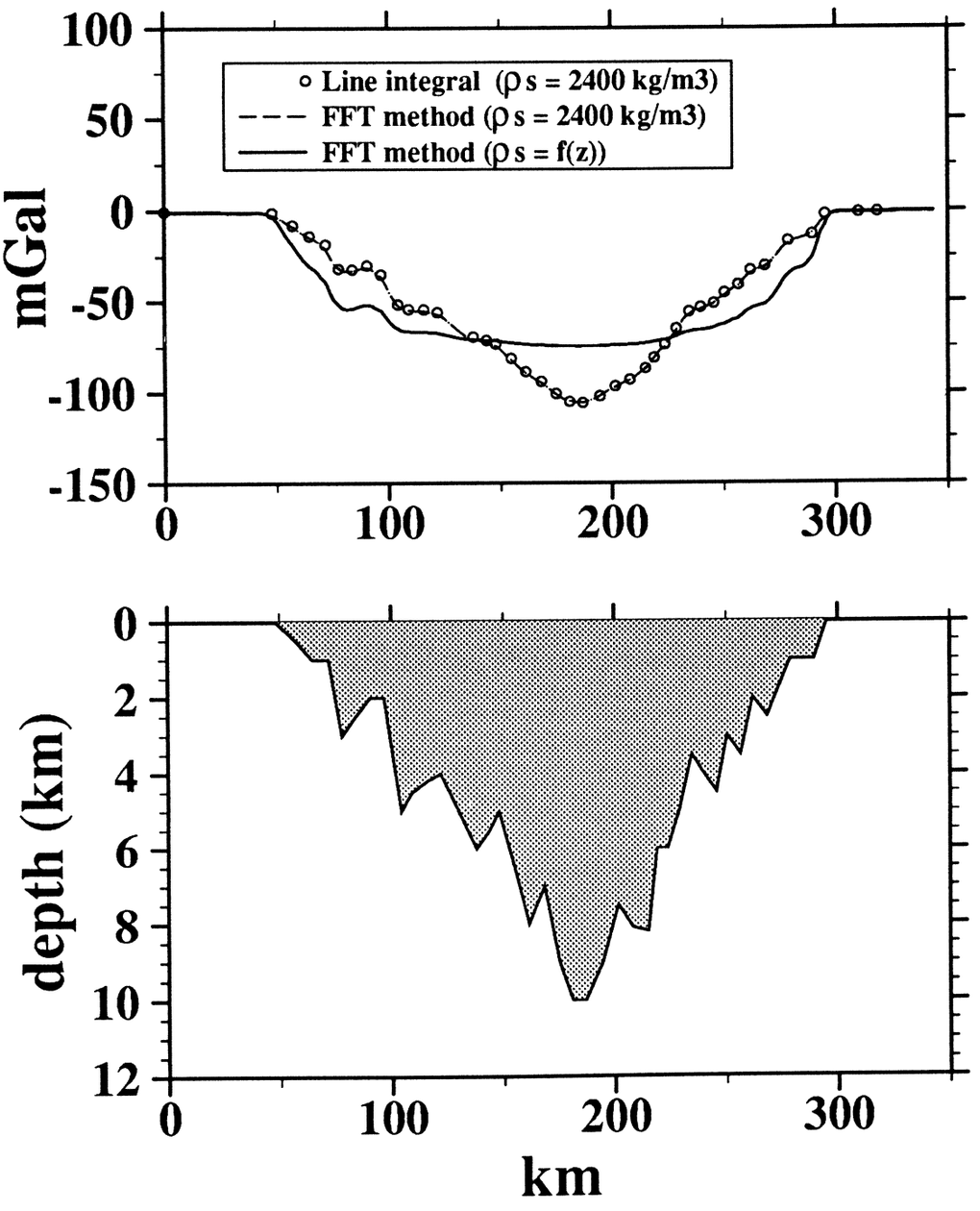

Figure 5.8. Comparison between line integral and FFT method for calculating the gravity effect of a hypothetical basin. Top graph shows the gravity anomalies; $f(z)$ represents depth-varying density given in equation 5.14 with grain density ρ_g = 2680 kg m^{-3}. Bottom graph is the basement profile.

Effect of sediment compaction Cowie and Karner (1990) have shown that density changes due to sediment compaction in sedimentary basins can have a significant effect on the gravity anomaly. Figure 5.9 shows the difference in the gravity effect of the sediment in Line E computed using uniform sediment density (2400 kg m^{-3}) and a depth-varying density function that is linked with an exponential porosity equation (Athy, 1930)

$$\phi(z) = \phi_o e^{-cz} \tag{5.13}$$

where z is the vertical depth coordinate, ϕ_o is the porosity at the depositional surface $z = 0$, and c is the exponential decay constant. For the Malay and Penyu Basins, the values of ϕ_o and c were determined from porosity and sonic logs (Appendix A.2): $\phi_o = 0.55$ and $c = 0.50$ km^{-1}. The density contrast between sediment and water is given by (Cowie and Karner, 1990)

$$\Delta\rho(z) = -(\rho_g - \rho_w)\,\phi_o\, e^{-cz} \tag{5.14}$$

where ρ_g is the grain density (2680 kg m^{-3}).

The equations for calculating the gravity anomaly are given in Cowie and Karner (1990). The gravity anomaly at the Earth's surface, $\Delta G(x, z = 0)$, resulting from a density constrast $\Delta\rho(x', z)$ is given by

$$\Delta G(x,0) = 2\gamma \int_{-\infty}^{\infty} \int_{0}^{h(x)} \frac{(z+d)\,\Delta\rho(x',z)\,dx'\,dz}{(x-x')^2 + (z+d)^2} \tag{5.15}$$

where x and x' are the horizontal coordinates, z is depth (positive downwards), γ is the universal gravitational constant, and $h(x)$ is the thickness of the sediment layer containing the density variation, measured relative to a reference plane at a depth d below the surface. $\Delta G(x, z = 0)$ is obtained by solving 5.15 in the Fourier domain, with the reference plane redefined as h_{max} — the base of the sedimentary layer containing the density variation (Cowie and Karner, 1990, p. 143):

$$\Delta G(x,0) = \mathcal{F}^{-1}\left[2\pi\gamma\, e^{-k\,h_{max}} \sum_{n=0}^{\infty} \frac{k^n}{n!}\, \mathcal{F}\left\{\int_{h_{max}-h(x)}^{h_{max}} u^n\, \Delta\rho(x,u)\,du\right\}\right] \tag{5.16}$$

where $u = (h_{max} - z)$. In the redefined coordinate system, the density structure (equation 5.14) is now given by

$$\Delta\rho(u) = -(\rho_g - \rho_w)\,\phi_o\, e^{-c\,(h_{max}-u)} \tag{5.17}$$

For implementation in the computer program, the solution to 5.16 as given by equation 7a in Cowie and Karner (1990, p. 144) is used.

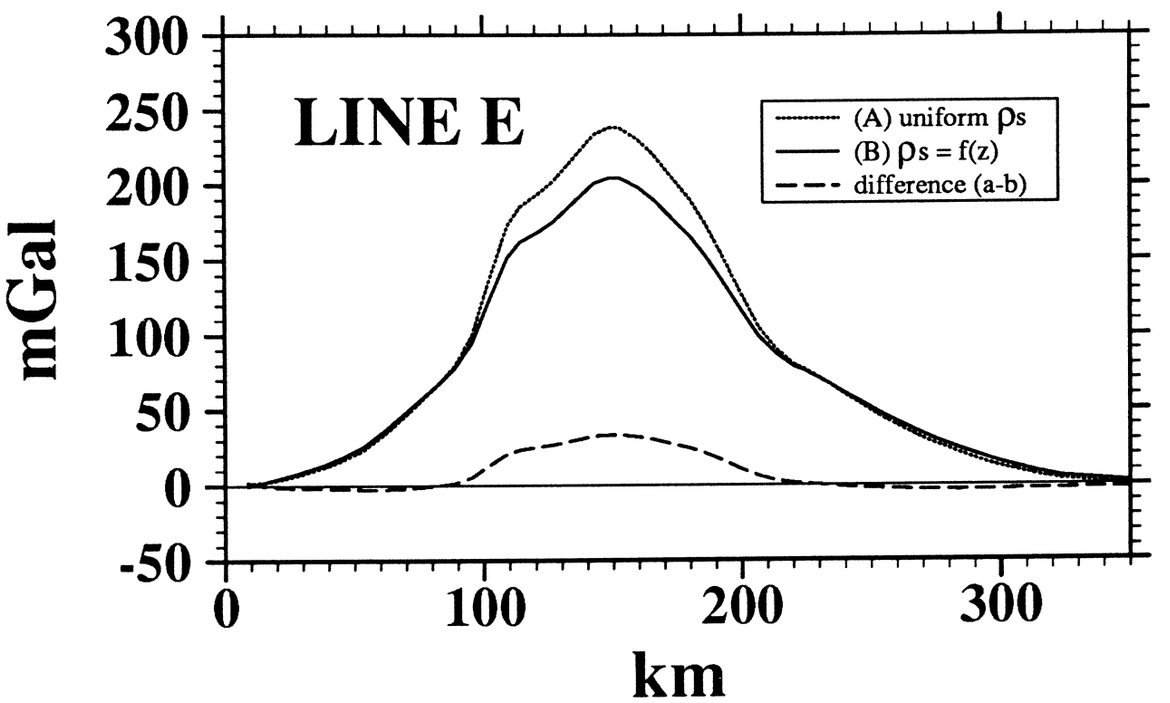

Figure 5.9. Gravity effect of sediment computed in line E using (A) uniform density of 2400 kg m^{-3} and (B) an exponential density-depth function (equation 5.14). Calculation using Fourier method (Cowie and Karner, 1990).

The result in Fig. 5.9 shows that, at the centre of the Basin where the sediment is thicker, the depth-dependent density model gives a lower amplitude but slightly wider anomaly than the uniform density model. This is because compaction in the deeply-buried sediment results in sediment density that approaches that of the basement ($\Delta\rho \rightarrow 0$) whereas less compaction of sediments on the basin flanks enhances the density contrast. Figure 5.9 shows that the error introduced by ignoring compaction effects is as high as 33 mGal (16%).

Compaction affects also the value of tectonic subsidence obtained by backstripping because the sediment density is no longer uniform and, hence, the load distribution, q, can not be represented simply in terms of the total sediment thickness. To remove compaction effects in the backstripping calculations, the load distribution has to be specified as the equivalent thickness, y', of sediment grains in a column of sediment. This is done by integrating the porosity equation (5.13) over the thickness of the sediment column, S^*, giving

$$y' = S^* - \frac{\phi_o}{c}(1 - e^{-cS^*}) \tag{5.18}$$

Because water does not contribute to the deflection ($\rho_{infill} = \rho_w$ and $\Delta\rho = 0$), the load distribution is now simply

$$q(x) = y'(x)\,\rho_g\,g \tag{5.19}$$

where ρ_g is the average sediment grain density and y' is the equivalent thickness of sediment grains. Lateral variation in lithology is ignored. Note that in the computation of S_T in equation 5.10 the equivalent thickness of water is implicitly incorporated in the term $y(x)$. We are, effectively, subtracting the flexural effect of the sediment grains from the bulk sediment thickness.

Figure 5.10 illustrates the effect of including compaction in the backstripping with $T_e = 0$. Because there is more compacted sediment at the centre of the Basin and, hence, more sediment grain per unit thickness, the flexure is enhanced, thereby reducing the tectonic subsidence slightly. The opposite is true on the margins because the sediment there is less compacted. A small change in the tectonic subsidence, however, produces a significant change (more than three times) in the backstrip Moho depth (see equation 5.11). Hence, significant errors in the calculation of gravity anomaly may result if the effects of sediment compaction are neglected in the backstripping and gravity modelling. These errors could be reduced by flexural backstripping layer by layer of different densities (Watts, 1988) (see equation 5.10, p. 156). The use of a continuous depth-porosity profile, in this study, is equivalent to backstripping an infinite number of layers of different densities.

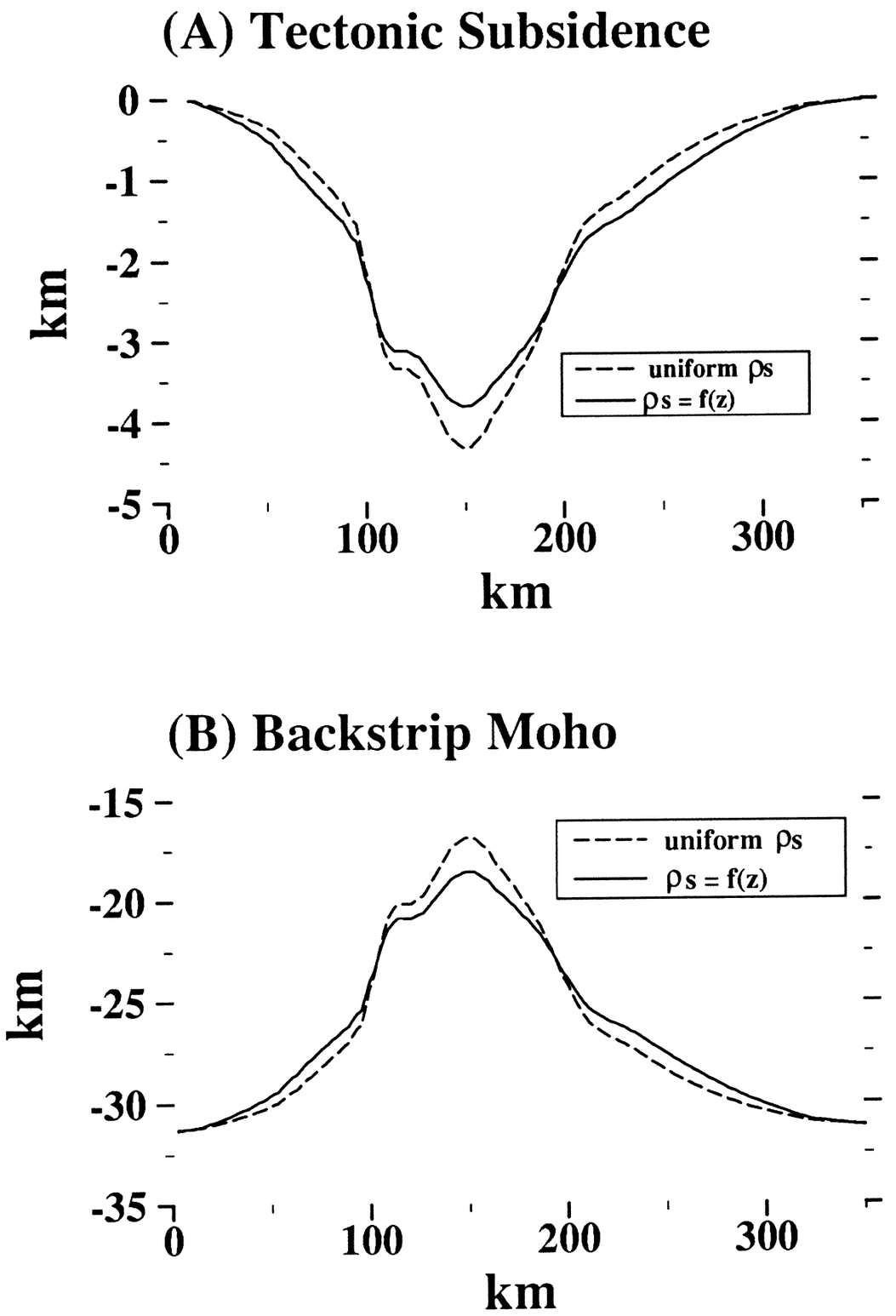

Figure 5.10. Comparison of the results of flexural backstripping Line E using uniform sediment density and depth-varying density (equation 5.14). $T_e = 0$ is assumed. (A) The effect of compaction on tectonic subsidence to is to decrease it slightly at the basin centre while increasing it slightly at the margins. (B) Depth to backstrip Moho based on the tectonic subsidence in (A). Note that the Moho depth is greater when depth-dependant density is used, which will have a significant effect on the gravity anomaly.

5.3 Results

5.3.1 Malay Basin

Line E is located at the northeastern end of the Basin (Fig. 5.3). The maximum sediment thickness along this profile is about 10 km. The result of gravity modelling for T_e = 0 km (*i.e.* Airy isostasy) is shown in Fig. 5.11. If a uniform sediment density of 2400 kg m^{-3} is assumed (Fig. 5.11A) the calculated anomaly is narrower and more negative by ~15–20 mGal relative to the observed. Hence, the density contrast from the sediment appears to have been overestimated.

In Fig. 5.11B, the gravity anomaly has been re-calculated using the depth-varying density model and shows a strong positive anomaly instead of a negative, which is still unacceptable. We now have to consider the possibility of T_e >0 to explain the observed gravity. To determine whether or not a finite T_e would give a better solution, the anomaly is calculated using several values of T_e and uniform sediment density (Fig. 5.12). The results show that by increasing T_e, the positive effect of the sediment and mantle contribution to the total anomaly is increased (see Fig. 5.6) because a higher T_e means a greater tectonic subsidence and a shallower backstrip Moho depth. When compaction is included in the calculations none of the model for T_e >0 can match the observed gravity anomaly (Fig. 5.13). All the above calculations assume Airy rather than thermal isostasy. If thermal isostasy is used, however, the backstrip Moho depth would be shallower for the same tectonic subsidence (Fig. 5.7), resulting in an even greater disagreement between the observed and calculated gravity anomaly. It is concluded, therefore, that the observed gravity anomaly along Line E is best explained by a very low T_e that approaches zero. The positive anomaly that results from using T_e = 0, however, suggests that the sediment load is only *partially compensated* by crustal thinning; in other words, the Moho depth is deeper than the *isostatic Moho*, *i.e.* the Moho depth that is expected for perfect Airy compensation.

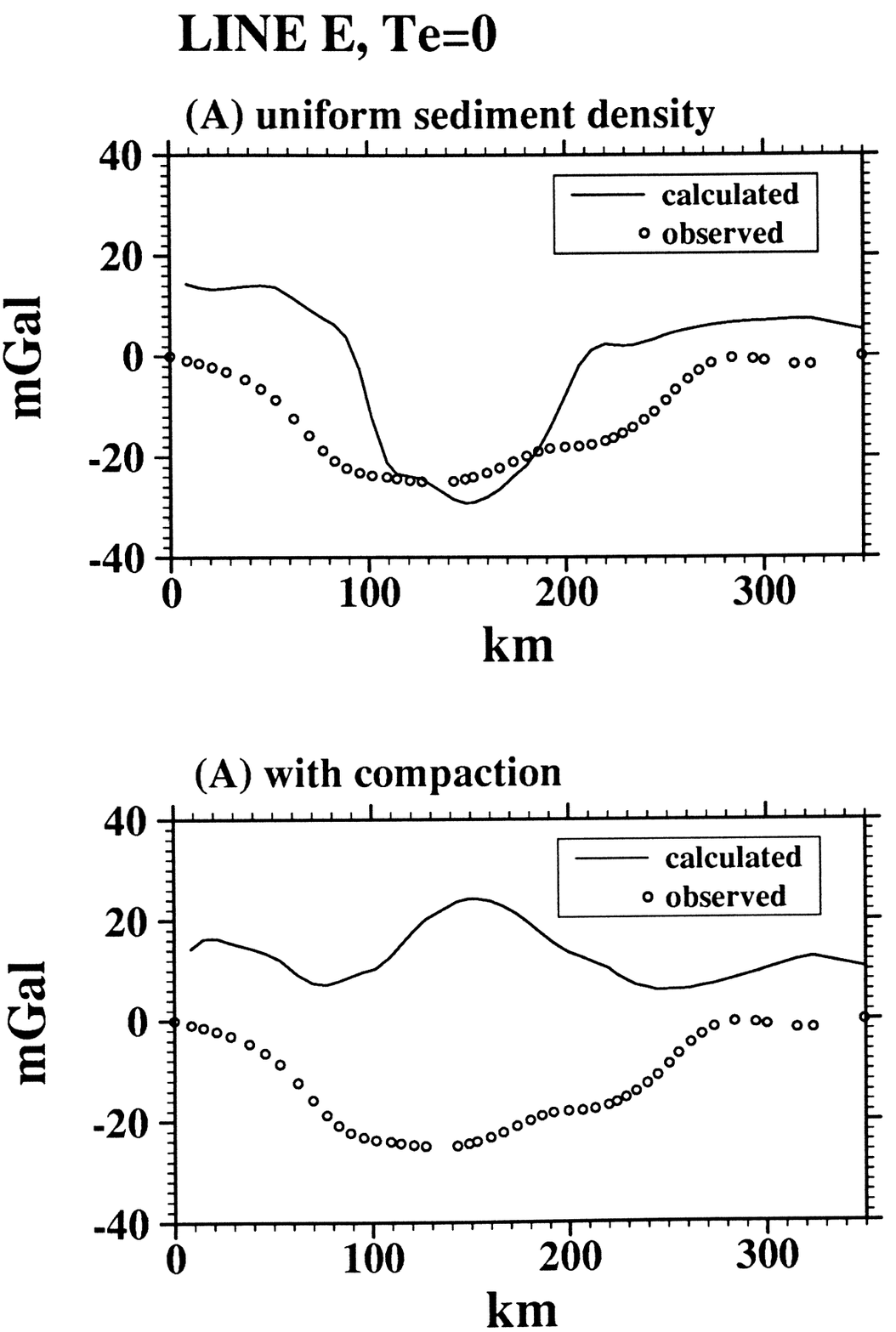

Figure 5.11. Result of gravity modelling Line E for $T_e = 0$. (A) Uniform sediment density of 2400 kg m^{-3} is assumed. (B) Exponential density function is assumed to account for compaction.

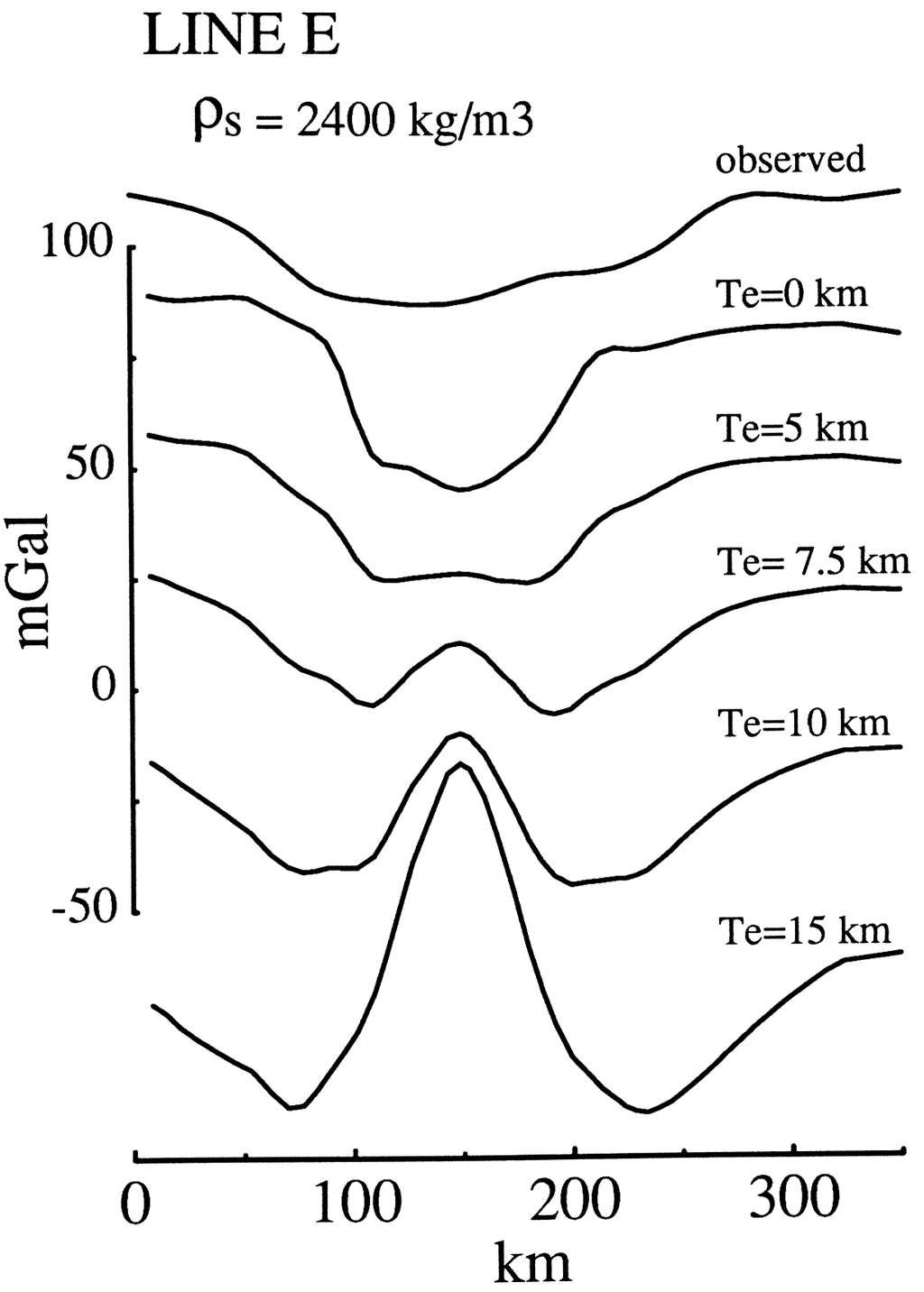

Figure 5.12. Gravity anomalies in Line E for various T_e values, using uniform sediment density.

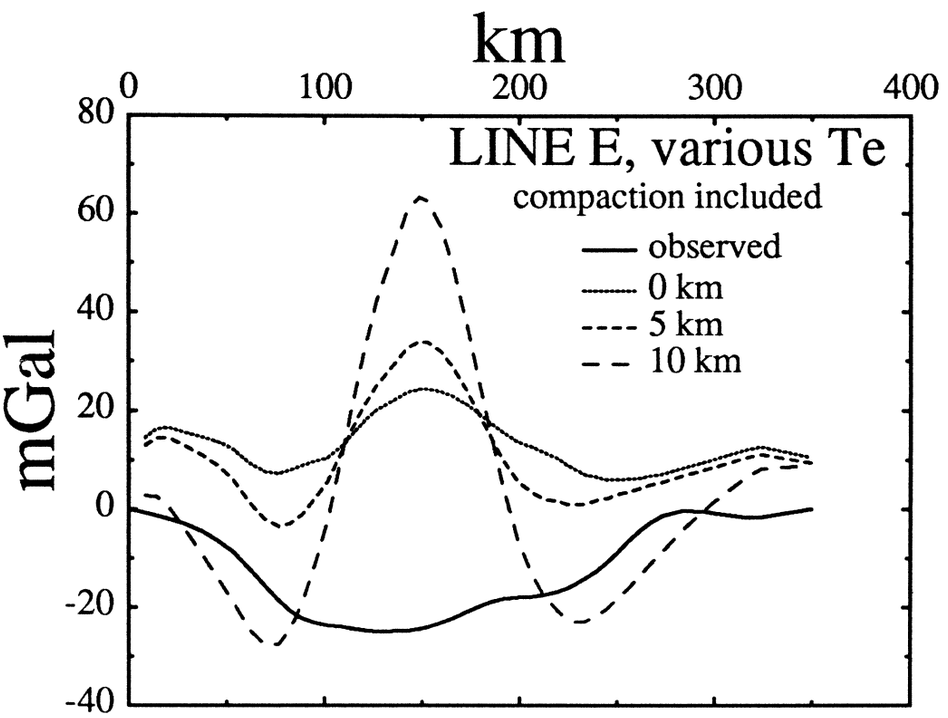

Figure 5.13. Gravity anomalies in Line E for various T_e values, using depth-varying density function. A close fit to the observed is obtained for $T_e = 5$ km.

To model the gravity effect of "partial compensation", the quantity C_m is introduced as a measure of the degree of mantle compensation (Fig. 5.14), which is defined as the ratio of the Moho elevation for partial compensation to that of perfect Airy compensation, both measured relative to the compensation depth, *i.e.* the base of the unstretched crust. The value of C_m, therefore, ranges from 0 for an uncompensated basin to 1 for a fully compensated basin. The new depth z_p to the Moho used to calculate the gravity effect of the mantle for a partially compensated basin is thus

$$z_p = y_c - C_m(y_c - z_m) \tag{5.20}$$

Figure 5.15 shows the result of modelling the gravity assuming the basin is compensated by a fraction of the isostatic Moho depth. From the best-fit calculated anomaly, it was found that $C_m = 0.77$, *i.e.* the Moho is 23% lower than the expected isostatic Moho. The results suggests that about a quarter of the to-

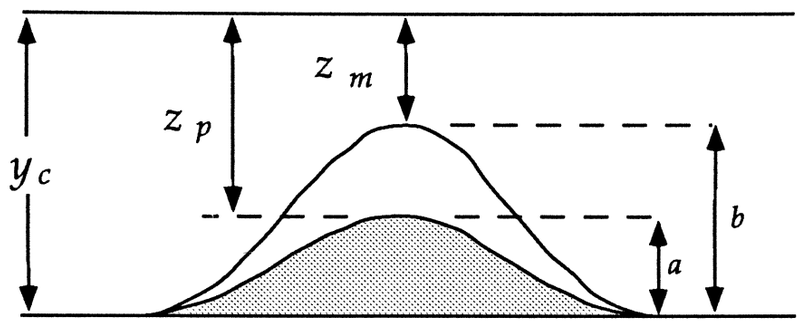

$$C_m = a \div b$$

$$= \frac{y_c - z_p}{y_c - z_m}$$

Figure 5.14. Model for Moho elevation above compensation depth, at the base of the unstretched crust, for partial compensation, a, defined as a fraction of the isostatic Moho elevation b determined from backstrip Moho z_m. The degree of compensation C_m is defined as the ratio a/b, expressed in terms of depths measured relative to the surface.

tal subsidence in the Basin is not compensated by crustal thinning, leading to undercompensation.

We now examine Line D in the far south of the Basin, to see if the data is consistent with the findings in Line E. Following the same procedure as before, the result for Line D (Fig. 5.16) shows that the observed gravity anomaly is best explained by a model of partial compensation with $C_m = 0.71$ which, interestingly, is comparable to the value obtained from Line E. These results strongly suggest that the lithosphere appears to be weak ($T_e = 0$) and the basin is only partially compensated. To investigate the effect of T_e on the result from line D, the anomalies for $C_m = 0.71$ were calculated using several values of T_e. The results (Fig. 5.17) indicate that for T_e values greater than 5 km, the central positive due to the mantle contribution becomes unacceptably high. When a lower C_m is used to reduced the effect of the mantle, the amplitude of the anomaly becomes too large. It seems, therefore, that a model with $T_e = 0$ best explains the gravity anomaly along Line D.

We now look at Line C in the central and deepest part of the Malay Basin,

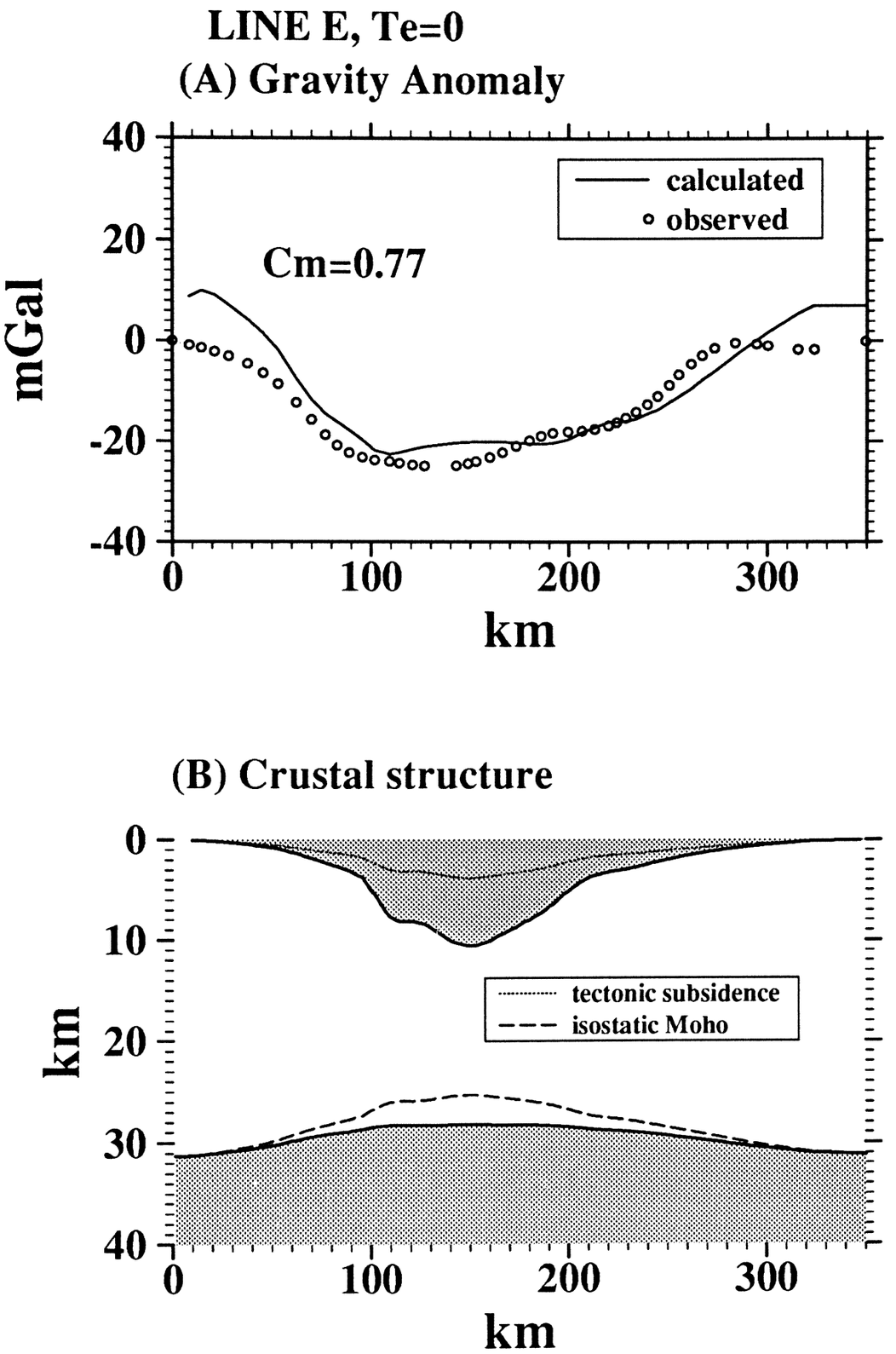

Figure 5.15. Result of gravity modelling of Line E. (A) Best-fit calculated anomaly representing $C_m = 0.77$. $T_e = 0$ km. (B) Crustal structure deduced from the best-fit model of $C_m = 0.77$. Note that to explain the gravity anomaly, we require the Moho to be deeper than the isostatic Moho ($C_m = 1.0$).

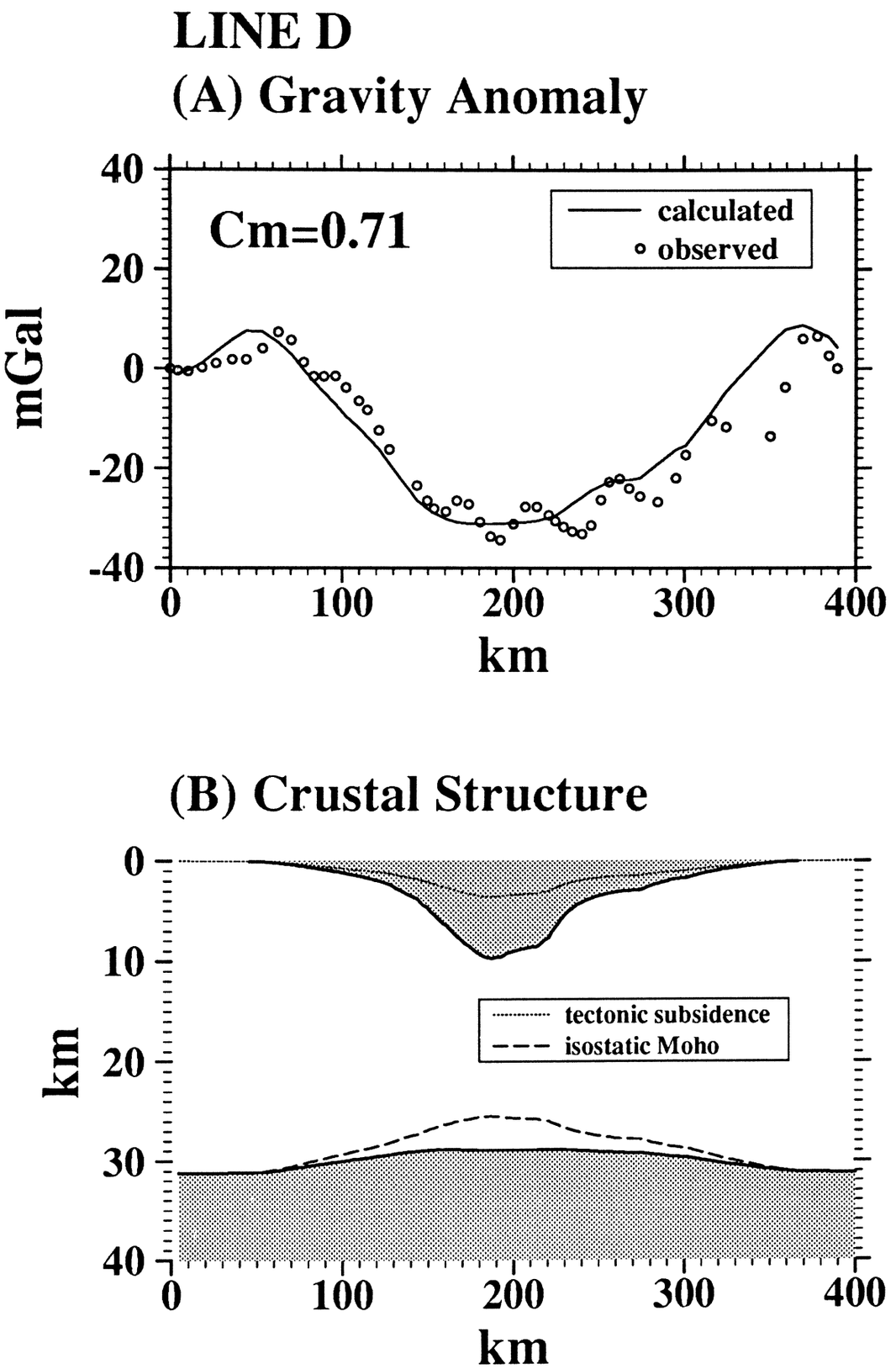

Figure 5.16. Modelled gravity anomalies and crustal structure for Line D. (A) The best fit line requires $C_m = 0.77$, comparable to the result in Line E (Fig. 5.15). (B) Restored crustal structure based on best-fit model of $C_m = 0.77$ and $T_e = 0$ in (A). Compare the predicted Moho and the isostatic Moho.

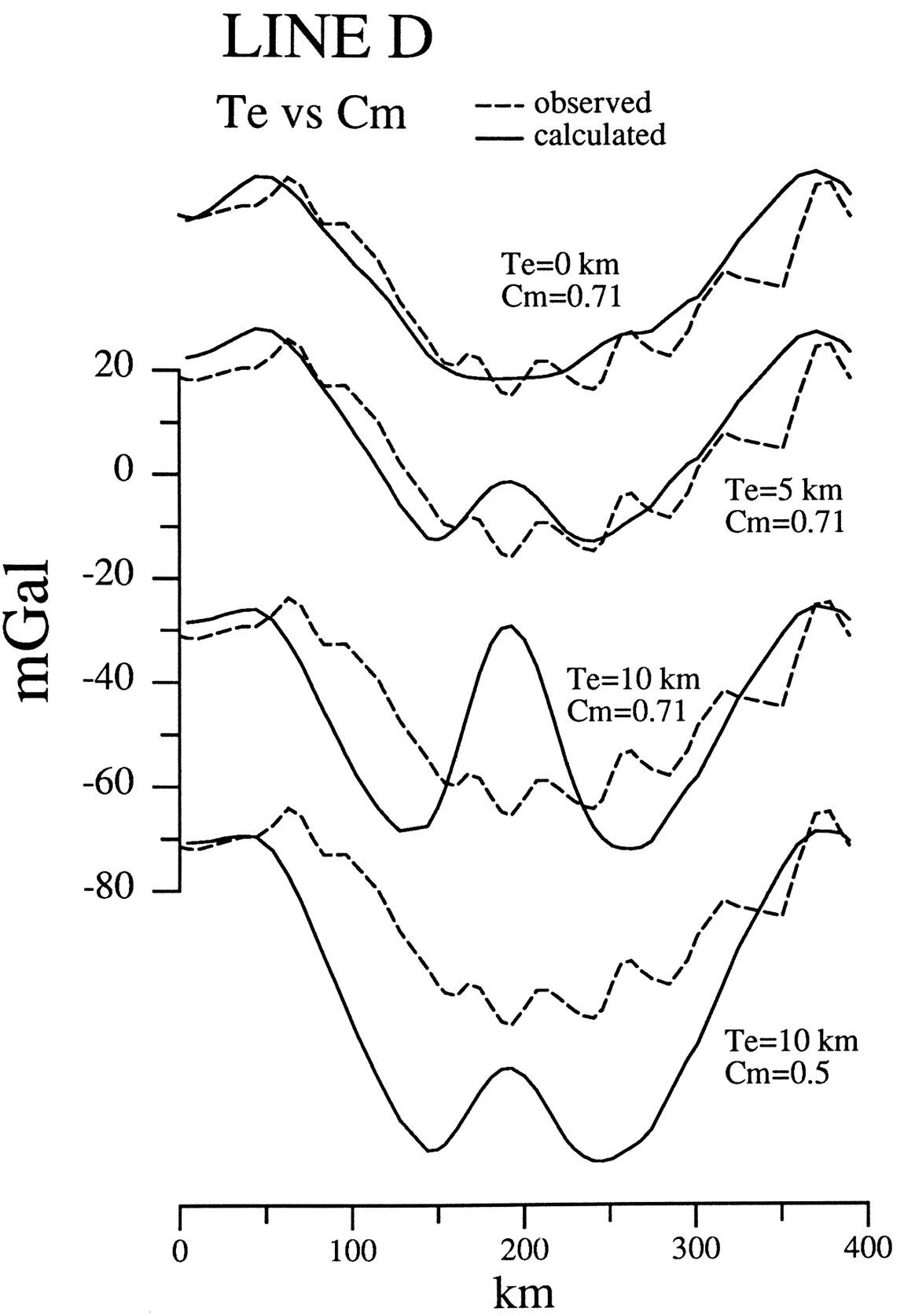

Figure 5.17. Gravity model for Line D for various T_e and $C_m = 0.71$. The results show that by increasing T_e, the mantle effect is increased, which is manifest in the central positive, as shown for cases where $T_e = 5$ km and $T_e = 10$ km. If the value of C_m is reduced to 0.5, the amplitude of the whole anomaly becomes too large.

where the maximum sediment thickness is perhaps greater than 15 km. Figure 5.18 shows the result of modelling Line C. The best-fit model suggests $T_e = 0$ and partial compensation at the 75% level, which is comparable with the previous two profiles. The result in Figure 5.18 shows that discrepancy still exists between the observed and calculated anomalies at the margins, although the amplitudes are well matched. A positive residual ($\Delta G_{calc} - \Delta G_{obs}$) at the margins indicates apparent mass deficiency underneath the flanks, which could be due to downward flexure of the Moho and implies that T_e may be finite but, probably, close to zero.

5.3.2 Penyu Basin

The Penyu Basin is a narrower and shallower basin; in Line A the basin is less than 200 km wide and ~6 km deep. Line A is a NNW–SSE profile across the Kuantan Graben, which contains more than 7 km of sediment. The profile shows a pronounced asymmetry, formed by a twin half-graben system with the main bounding faults dipping in opposite directions towards the basin centre. The northern graben is deeper than the southern one, and a prominent basement ridge separates the two half-grabens.

The results from modelling Line A are shown in Fig. 5.19. As was done previously, modelling was done by assuming, initially, $T_e = 0$ and a depth-varying density function to see the effect these have on the anomalies (Fig. 5.19A). Generally, the form of the calculated anomaly is similar to that of the observed but a major discrepancy arises due to the outward-sloping edge effects that are absent in the observed anomaly. By excluding the mantle contribution, the edge effect was completely removed but resulted in a very low negative anomaly. The positive residuals above the basin flanks suggest mass deficiency underneath them, which could be caused by downward flexure of the crust and/or partial compensation. The apparent flexural effects suggest that $T_e > 0$.

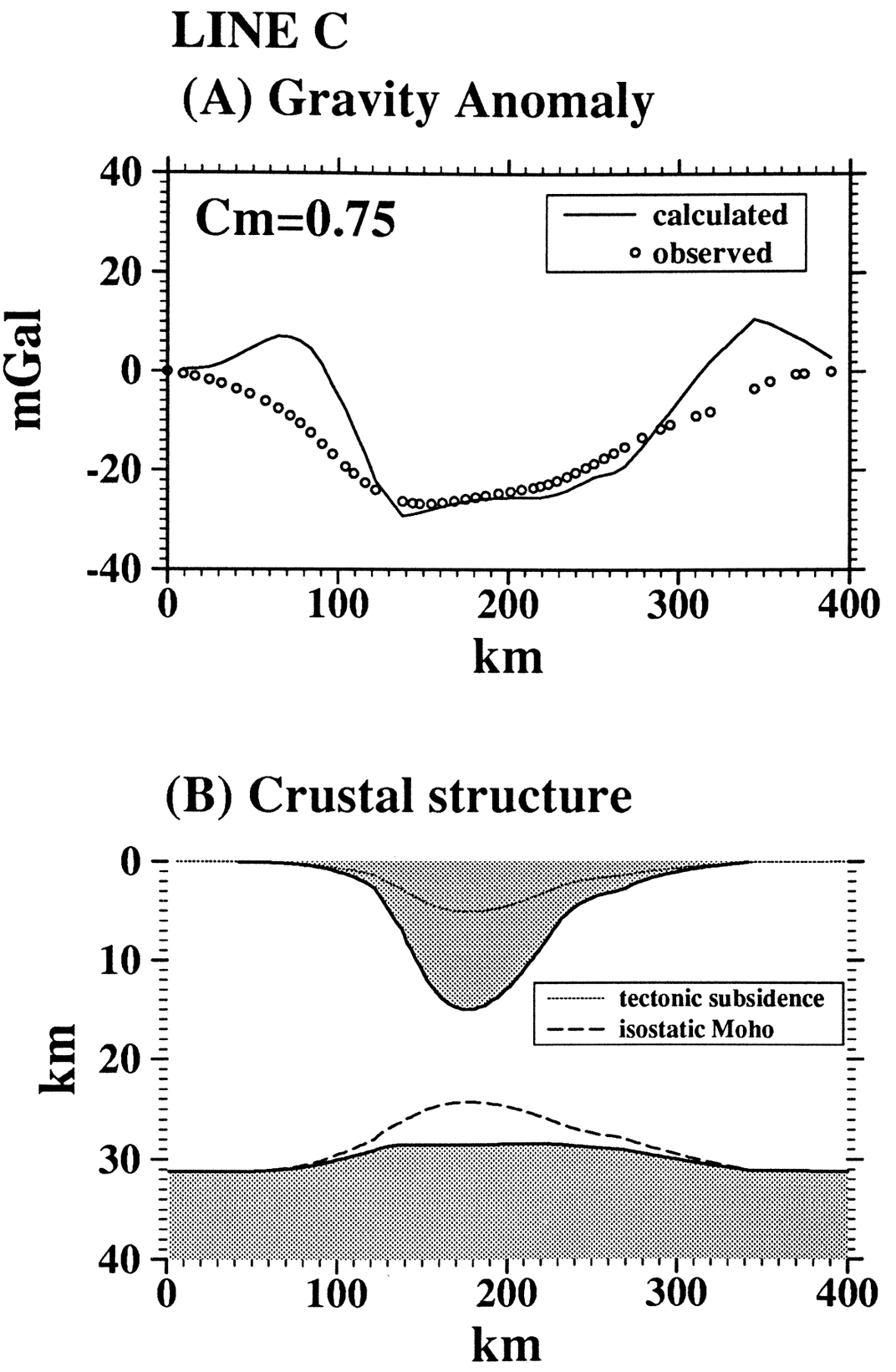

Figure 5.18. Result of gravity modelling for Line C. (A) The best-fit model is for C_m = 0.75. Note there is still significant positive residuals at the margins, suggesting that there is mass deficiency underneath the flanks, probably the result of downward flexure of the crust. (B) Restored crustal structure based on best fit model C_m = 0.75. Note the large deviation of the restored Moho from the isostatic Moho.

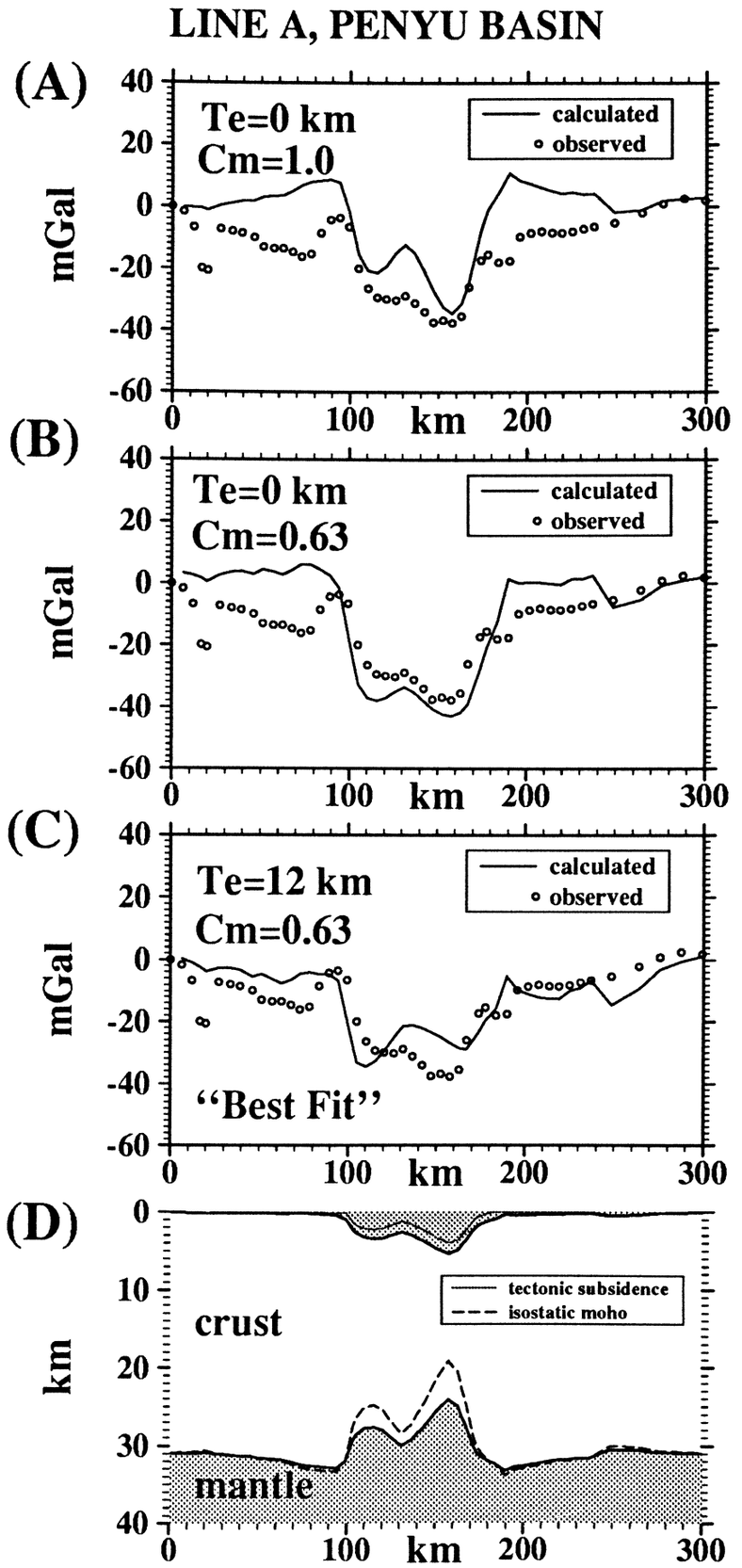

Figure 5.19. Results of gravity modelling Line A, Penyu Basin. (A) Initial modelling assuming $T_e = 0$ km and full isostatic compensation ($C_m = 1.0$). Exponential depth-density function is assumed. (B) Model for $T_e = 0$ km, but assuming partial compensation. A best-fit value for C_m was found to be 0.63. (C) Best overall fit: C_m at 0.63, $T_e = 12$ km. (D) Restored crustal structure based on the best-fit model in (C). Note the marked flexure of the crust-mantle boundary underneath the flanks, which gave rise to the inward-sloping anomaly of the observed.

To investigate the effect of T_e as well as partial compensation, Line A was modelled, first, by finding C_m that corresponds to the minimum value of σ_g. This turned out to be 0.63 (Fig. 5.19B). By invoking partial compensation, the *amplitude* of the anomaly and the edge effects were reduced. Figure 5.19B shows a reasonable fit between the observed and calculated anomalies at the centre of the Basin but rather poor fit at the edges. To minimize the residuals due to the edge effects, σ_g was determined again for various T_e values while maintaining C_m at 0.63. The effect of increasing T_e is to, essentially, flatten out the anomaly and thus achieving a better fit at the edges. σ_g was found to be minimum when T_e = 12 km (Fig. 5.19C). Note, however, that a poorer fit is observed at the centre of the Basin. This could indicate that T_e may not be uniform but changes laterally across the Basin, from 0 at the centre to 12 km on the basin flanks. Figure 5.19D shows the restored crustal structure based on the best-fit model of uniform T_e = 12 km and C_m = 0.63. The important feature in this reconstruction is the downward flexure of the crust underneath the margins, which explains the mass deficiency that is reflected in the inward-sloping observed anomaly (*cf.* Fig. 5.19A).

5.4 Discussion

5.4.1 Crustal Structure

Modelling the gravity anomalies using simple models of isostasy and crustal thinning has enabled us to predict the depth to the Moho underneath the Basins and reconstruct the crustal structure at the time of rifting. The predicted Moho depth as constrained by the best-fitting gravity model is, however, generally flat and deeper than the isostatic Moho. At present, no seismic refraction or deep reflection data is available to confirm the prediction. The compilation of refraction measurements in the region by Hayes *et al.* (1978) shows no measurements within the region north of the Natuna Islands.

We have no data to constrain the pre-stretching crustal thickness in the area. Hence, in the modelling study, it was assumed that the pre-stretching crustal thickness was 31.2 km, to conform with the thickness of a normal crust that is in isostatic balance with the mid-ocean ridge. There seems to be some evidence, however, that suggests a greater than "normal" crustal thickness in the region, which is not unlikely, considering that the region is part of the great Indosinian Orogen. Zhang *et al.* (1989) showed a map of crustal thickness in the South China Sea Basin and surrounding region. The crust at centre of that basin is about 10–12 km thick and increases to 30–34 km in the continents. They also showed a map of crustal thickness of Asia based on 1° × 1° mean gravity data which indicate that the crust beneath Thailand and Indochina has a thickness of 38–42 km, averaging ~40 km. Seismic modelling studies of the crust and upper mantle structure of the Eurasian continent by Feng and Teng (1983) also suggests an average crustal thickness of ~40 km in this region. Figure 5.20 shows the results of gravity modelling assuming that the initial crustal thickness was 40 km instead of 31.2 km. It was found that assuming a greater initial crustal thickness of 40 km does not change the results of the study: a model of partial compensation was still needed to explain the observed gravity, with $C_m = 0.78$, almost the same as that obtained by assuming 31.2 km initial crustal thickness (*cf.* Fig. 5.15).

5.4.2 Geological Implications of "Partial Compensation"

In the modelling study, the concept of partial compensation was introduced so that the backstrip Moho depth can be calculated based on a physical principle, rather than attributing the misfit in the anomalies to an unspecified mass deficiency. The geological meaning of partial compensation, however, requires further thought.

The gravity modelling results suggest that both the Malay and the Penyu Basins are not in complete isostatic equilibrium. Based on a simple model of crustal thinning, it was found that the Moho is deeper by ~25% than that expected if the Basins are in perfect isostatic equilibrium. Note that, we have assumed

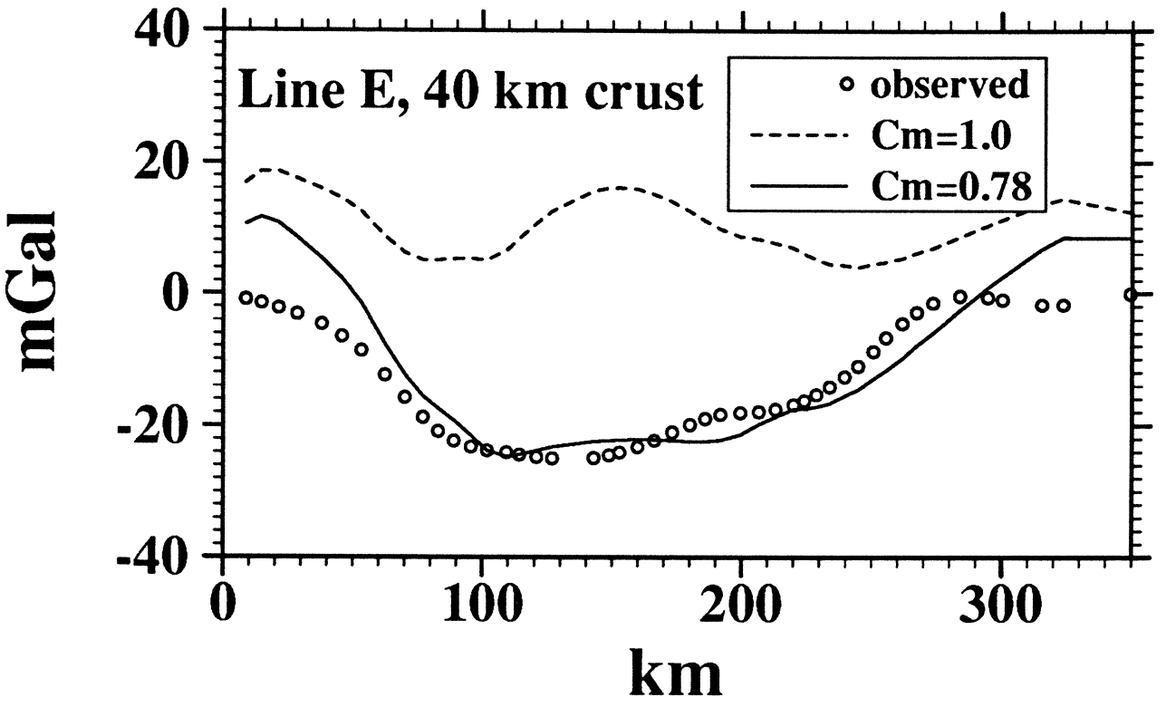

Figure 5.20. Result of gravity modelling Line E assuming an initial crustal thickness of 40 km instead of 31.2 km (*cf.* Fig. 5.15). Shown against the observed gravity are two modelled curves; $C_m = 1.0$ for full compensation and $C_m = 0.78$ representing the best-fitting partial compensation model.

Airy isostasy for all the calculations of backstrip Moho depth. The Moho depth would be shallower if a thermal model had been used when restoring the crustal structure, which would need an even lower value of C_m to explain the gravity anomaly. Hence, in the Airy model, the value of z_m derived from the best-fitting C_m value represents the minimum depth to the backstrip Moho.

There are two possible causes of deeper-than-expected Moho: (1) magmatic underplating or, (2), uncompensated subsidence due to strike-slip or detachment faulting. Although in-plane stress of reasonable magnitudes (a few kbars) can cause deflections in the order of a few tens of metres and may have important influence on the stratigraphy and relative sea-level changes (*e.g.* Cloetingh and Kooi, 1992), it is unlikely to have caused the additional ~1.5 km of subsidence in the Malay/Penyu Basins. The two possible causes are discussed below.

Magmatic underplating A deeper than expected Moho could be the result of the addition of relatively low-density material at the base of the crust, a phenomenon referred to as "underplating" (Cox, 1993). Possible examples of underplating have been described from other extensional basins, such as those around the British Isles (Brodie and White, 1994). Underplating is caused by partial melting in the asthenosphere as it rises adiabatically during stretching (McKenzie and Bickle, 1988; Bown and White, 1995a). When continental lithosphere is stretched, hot asthenosphere rises adiabatically underneath an area of thinned crust. Basaltic melt is generated when the adiabatic upwelling curve intersects the solidus; for a given lithospheric thickness and stretching factor, β, the extent of melting depends on the stretching rate and mantle potential temperature (T_p). Because basaltic melt has a lower mean density than the asthenosphere (< 3000 kg m^{-3}, White and McKenzie, 1989), it is likely to be emplaced at the base of the crust, effectively increasing the crustal thickness. According to McKenzie and Bickle (1988), this process may take place within 1 Ma or so since the start of rifting. This implies that, where underplating is involved, the amount of crustal thinning, or the crustal stretching factor, will always be underestimated because of the addition of low-density material to the crust during extension. Hence, the stretching factor based on the partially compensated Moho depth, z_p, represents the "apparent stretching factor", β_{app}, which is given by

$$\beta_{app} = \frac{y_c}{z_p - S_T} \tag{5.21}$$

where y_c is the unstretched crustal thickness and S_T is the tectonic subsidence from backstripping. From the results, the maximum β_{app} is 2.3 in Line C, which crosses the central deepest part of the Basin.

If stretching of the Malay Basin involved underplating, the difference between the isostatic and predicted Moho depths ($h = z_p - z_m$) (Figs. 5.15, 5.16, 5.18 and 5.19D) must represent the approximate thickness of the underplating material. The maximum value of h for each of the modelled profile is listed in Table 5.1, which suggests that up to 4 km of material may have been underplated beneath

Modelled profile	E	D	C	A
C_m	0.77	0.71	0.75	0.63
stretching factor, β	2.12	1.98	3.36	2.27
discrepancy in Moho depth, h (km)	2.9	3.4	4.2	4.0
anomalous subsidence (km)	0.87	1.03	1.26	1.49

Table 5.1. Maximum stretching factor, discrepancy in the Moho depth, and anomalous subsidence for the gravity profiles.

the Malay Basin.

Figure 5.21 is reproduced from McKenzie and Bickle (1988, fig. 22a) to show the relationship between melt thickness and β for various values of the asthenosphere potential temperature, T_p, and the thickness of the mechanical boundary layer. In this diagram, β represents the "true" stretching factor which is related to β_{app} by

$$\beta_{app} = \frac{y_c}{h + y_c/\beta} \tag{5.22}$$

where y_c is the initial crustal thickness and h is the thickness of the underplating material. Alternatively, β may be calculated using equation 5.21 but with the isostatic Moho depth, z_m, instead of z_p:

$$\beta = \frac{y_c}{z_m - S_T} \tag{5.23}$$

If the underplating hypothesis is correct, the maximum β in Line C, (Fig. 5.18) is 3.36. The maximum β values in the other profiles are shown in Table 5.1. Using Fig. 5.21, we should be able to estimate the thickness of melt generated during lithospheric extension based on the derived β values and compare with the discrepancy in the Moho depth (Table 5.1).

The most important control on the melt thickness during stretching is the asthenospheric potential temperature, T_p, which is the temperature of the asthenosphere on the adiabatic gradient projected to atmospheric pressure (McKenzie and Bickle, 1988). McKenzie and Bickle (1988) noted that the generally uniform thickness of oceanic crust (6–7 km) implies that a uniform asthenospheric tem-

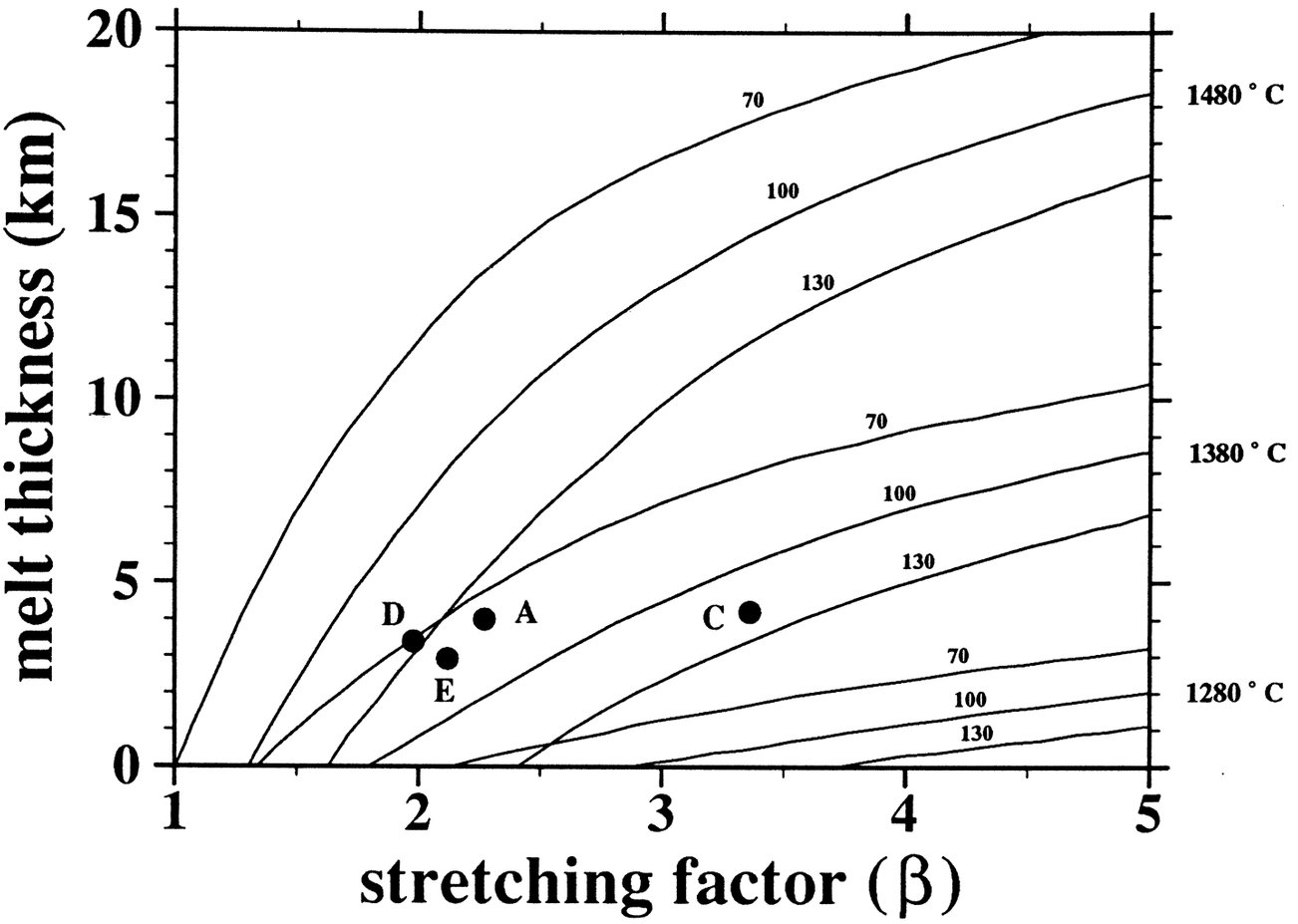

Figure 5.21. Graph of melt thickness *vs* stretching factor (Redrawn from McKenzie and Bickle, 1988). The three sets of curves represent different asthenospheric potential temperatures, T_p. Numbers on the curves represent the thickness of the lithospheric mechanical boundary layer in km. Solid circles correspond to β and discrepancy in Moho depth, h, based on the gravity modelling results (Table 5.1).

perature exists everywhere at a given depth, and that upwelling of asthenosphere with $T_p = 1280°C$ would give the observed 6–7 km of ocean crust. The value of 1280°C is, therefore, considered as "normal" asthenospheric potential temperature (McKenzie and Bickle, 1988). It follows, also, that in regions of thick crust, such as Iceland, where the crust is about 27 km thick, T_p is much higher, about 1480°C (White and McKenzie, 1989), which is usually attributed to a hot mantle plume. Figure 5.21 shows that a "normal" asthenospheric T_p of 1280 °C is expected to produce 6–7 km of ocean crust when β is about 6. If the same T_p is assumed, the maximum β (3.4) observed in the Malay Basin would produce a negligible thickness of melt and, thus, can not explain the discrepancy in the Moho depth, which is ~4 km (Table 5.1).

Significant amounts of melt could be generated, however, if T_p was higher, *i.e.* for example, when a hot mantle plume was involved. Indeed, the Malay and Penyu Basin data (Table 5.1) plot within a higher T_p field in Fig. 5.21, suggesting that underplating is a viable explanation but only when T_p is greater than normal. Note, however, that the graph in Fig. 5.21 is based on an instantaneous uniform stretching model (McKenzie and Bickle, 1988). Bown and White (1995b) have shown that, when rifting occurs over a finite duration, vertical and horizontal heat conduction reduce significantly the amount of melt generated, even for a rifting duration of a few million years. From their calculations (Bown and White, 1995b, their fig. 13), a stretching factor β of 4 attained over a period of 10 Ma, which is the estimated rifting duration for the Malay Basin (Chapter 6), would give no melt. Hence, it seems extremely unlikely that the discrepancy in Moho depth could have been the result of magmatic underplating.

Another strong argument against underplating is that it causes permanent uplift of the basin because the density of the underplating material is lower than that of the mantle. If the lithosphere has a significant rigidity, the uplift would have been resisted by flexure. However, because the lithosphere here is found to be weak, the addition of low-density material at the base of the crust should have resulted in uplift. Assuming Airy isostasy for a weak lithosphere, the amount of uplift, U, depends on the thickness of melt, h, added to the crust:

$$U = \left(\frac{\rho_m - \rho_x}{\rho_m - \rho_w} \right) h \tag{5.24}$$

where ρ_m, ρ_w, and ρ_x are the densities of mantle (3330 kg m^{-3}), water (1030 kg m^{-3}) filling the basin, and the underplating material or melt, respectively. The results of gravity modelling (Table 5.1) suggest that up to about 4 km of material may have been added to the base of the crust. The addition of 4 km of melt with a density of say, 2900 kg m^{-3}, would have resulted in at least 0.75 km of uplift. This uplift must have occurred during or immediately after the stretching phase (*i.e.* prior to 25 Ma) because the subsidence history of the Malay Basin (Chapter 6) shows no sign of significant uplift later than 25 Ma. Theoretically, uplift by

underplating results in a negative shift of the subsidence curves (Fig. 5.22) but does not affect the general form of the thermal subsidence significantly although the final subsidence (*i.e.* when $t \rightarrow \infty$) will be less than expected (see Bown and White, 1995a). This suggests that, if the underplating hypothesis is correct, the subsidence at the centre of the Basin may have been underestimated by as much as 0.75 km. This is unlikely because an even higher stretching factor would be required to explain the tectonic subsidence.

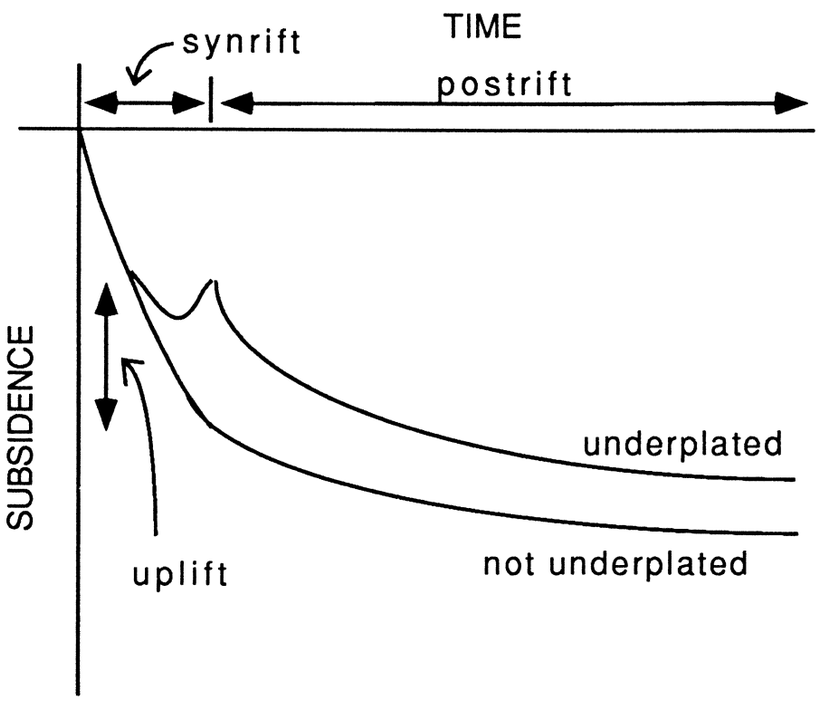

Figure 5.22. Effect of underplating on subsidence curve. Underplating during synrift phase results in negative shift of curve, but the shape of the thermal subsidence curve not affected.

Combination of strike-slip and stretching The results suggest that the Malay and Penyu Basins are isostatically undercompensated (Fig. 5.23A) because the Moho is deeper than expected, given the amount of observed tectonic subsidence. An alternative interpretation would be to view the total (observed) tectonic subsidence as the sum of two components: compensated subsidence resulting from stretching and uncompensated subsidence caused by some other tectonic process. As shown in Fig. 5.23B, we can calculate these two components of subsidence by

assuming that the backstrip Moho depth constrained by gravity modelling represents the upwelled mantle topography caused by stretching. Hence, only that portion of subsidence that is in isostatic balance with the Moho topography could have resulted from the stretching process. This portion of the observed subsidence is the compensated subsidence (Fig. 5.23B), which is less than the observed subsidence for an undercompensated basin. The difference between the observed and the compensated subsidence is, therefore, the uncompensated subsidence.

The subsidence from lithospheric stretching, *i.e.* the compensated subsidence, can be derived from equation 5.11 with z_p in place of z_m. Hence, we find that 23–37% (0.8–1.5 km) of the observed tectonic subsidence in the Malay and Penyu Basins is uncompensated and unaccounted for by the crustal thinning (Table 5.1). Note that, because the basin age is probably less than the thermal time constant of the lithosphere and that the Airy model was used to calculate the backstrip Moho, the compensated subsidence represents the maximum tectonic subsidence (S_∞) that can result from the crustal thinning. If the thermal model had been used, a larger proportion of the total subsidence would be uncompensated.

We need to explain the reason for the uncompensated or "anomalous" subsidence. In some basins around the British Isles, for example, anomalous subsidence have been attributed to an earlier phase of stretching (Hall and White, 1994). If the anomalous subsidence in the Malay and Penyu Basins was caused by an earlier phase of lithospheric stretching, that component of crustal thinning should be manifested in the gravity anomaly. It is, therefore, unlikely that an earlier phase of stretching had affected the Basin.

One possible explanation for this part of the subsidence may have been the result of extension in the upper brittle crust which is detached from the lower crust and mantle. In terms of the block model (Fig. 4.16, p. 139), we may perceive the crustal blocks within the shear zone as being afloat above a fluid layer representing the relatively ductile lower crust and mantle. If strike-slip basins and rift basins represent two end-members in terms of their state of isostasy (Fig. 5.1), the

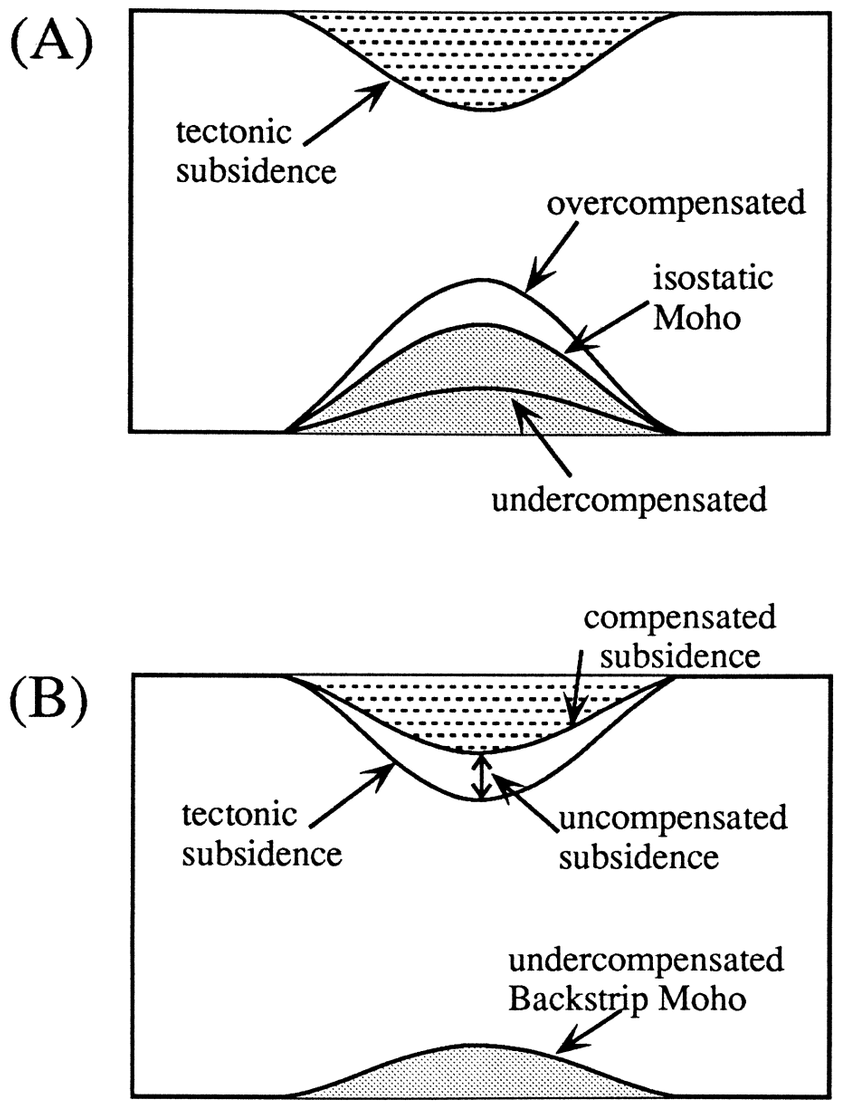

Figure 5.23. Interpretation of partial compensation. (A) From tectonic subsidence obtained by backstripping, the backstrip Moho configuration is constrained gravity modelling. The degree of compensation is defined relative to the isostatic Moho which, theoretically, represents perfect Airy compensation. Hence, a departure from the isostatic Moho results in over or undercompensation. (B) Alternatively, the tectonic subsidence that would have been compensated fully by the best-fit Moho topography, here referred to as "compensated subsidence", may be derived from the partially compensated Moho depth, z_p (Fig. 5.14). The difference between the backstripped tectonic subsidence and the compensated subsidence represents the "uncompensated" subsidence.

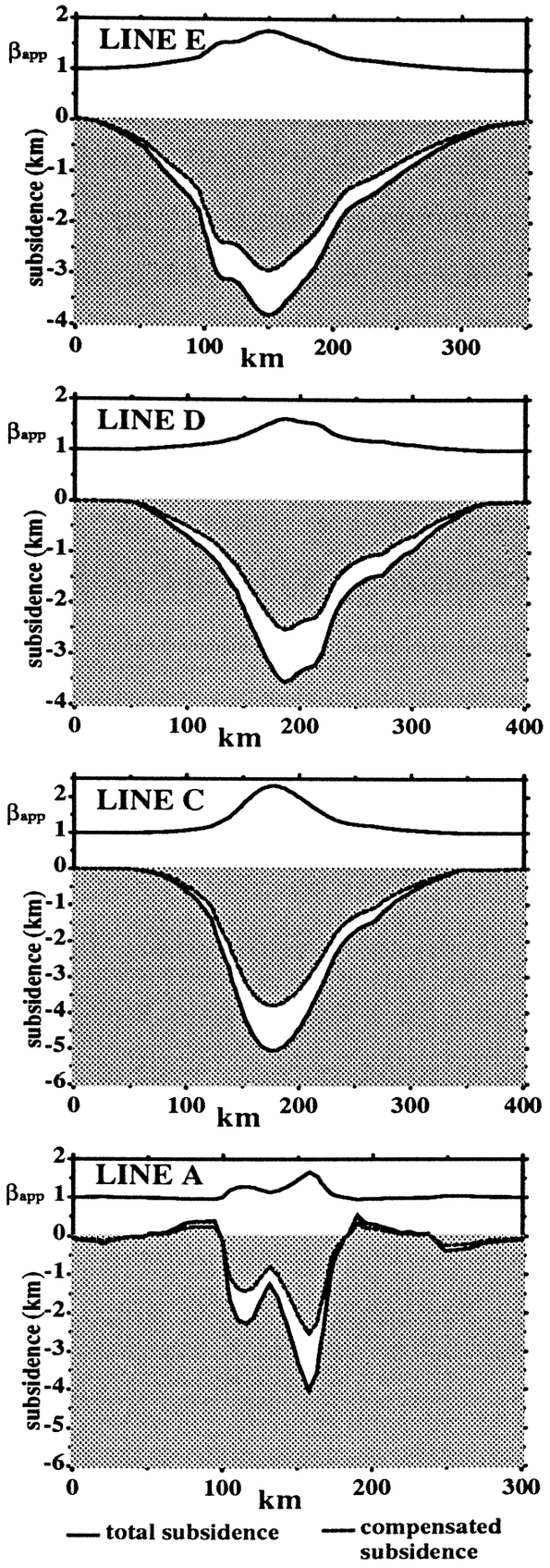

Figure 5.24. Backstripped tectonic subsidence along the four modelled profiles. The lower part of each plot shows the total subsidence S_T obtained by flexural backstripping and the subsidence inferred from the value of C_m indicated by the best-fit gravity model. The difference between the two (unshaded area) represents uncompensated subsidence that is unaccounted for by lithospheric stretching. Also shown in each plot is a profile of β_{app} calculated based on the predicted Moho depth.

results suggest that the Malay and Penyu Basins are some sort of "hybrid" basins that were formed by a combination of upper-crustal faulting and whole-lithosphere stretching. The total tectonic subsidence, S_T, obtained from backstripping, thus comprise two components: one that is compensated by crustal thinning and results from lithospheric stretching, and the other uncompensated component that could be a consequence of upper crustal "flaking" (Yeats, 1983) and strike-slip tectonics. Figure 5.25 shows schematically the concept of a "hybrid" basin formed by a combination of upper crustal detachment faulting and whole-lithospheric stretching. "Thin-skinned" crustal extension results in an isostatically uncompensated basin with a large negative anomaly whereas "thick-skinned" or whole-lithospheric extension results in a basin whose subsidence is compensated by mantle upwelling and characterised by a positive gravity anomaly. Here, the term "uncompensated" refers to the state of isostasy within the perimeter of the basin although compensation is probably displaced laterally and, therefore, occurs outside the basin. A combination of the two processes would result in an undercompensated basin in which the tectonic subsidence is greater than can be accounted for by crustal thinning. Such a basin is characterised by a low-amplitude free-air gravity signature. Note that, in such basins, analysis of tectonic subsidence by 1D backstripping to estimate stretching factor is not straight-forward (Chapter 6). This is because the total subsidence history is a combined result of two processes whereas in the lithospheric stretching model, we are usually concerned only with the subsidence/uplift associated with "thick-skinned" mantle-involved extension.

5.4.3 Effective Elastic Thickness, T_e

Unlike oceanic lithosphere, the continental lithosphere does not show a simple relationship between T_e and plate age. There is still disagreement as to whether flexural rigidity should be taken into account in subsidence analysis, as has been shown, for example, in the North Sea (White and Latin, 1993). It is widely established from oceanic flexure studies that oceanic T_e follows the depth to 450

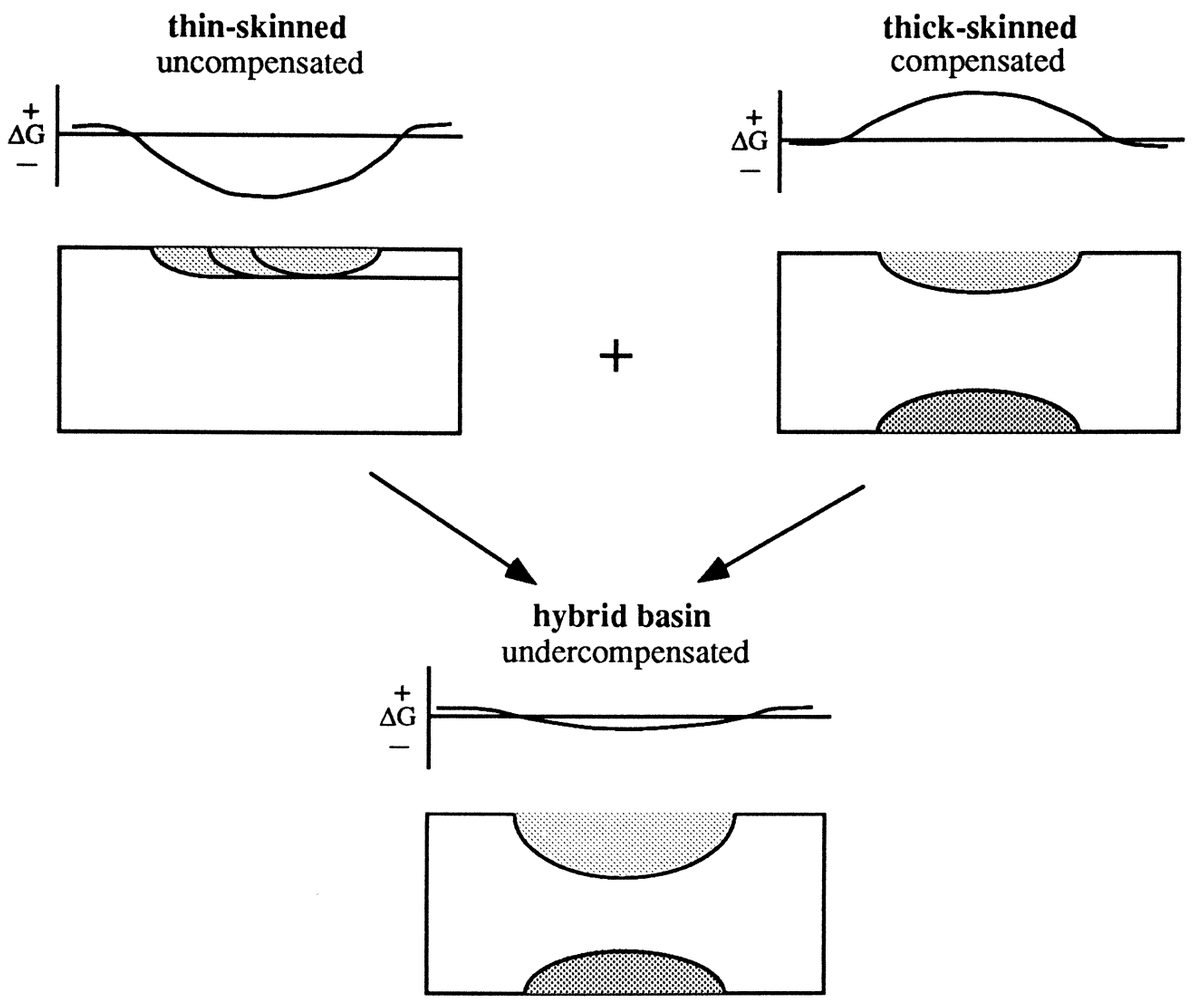

Figure 5.25. Model for combined thin-skinned and thick-skinned extensional basins and their free-air gravity signatures. Thin-skinned basin (left), forms by strike-slip and/or upper-crustal detachment faulting, is characterised by a large negative gravity anomaly, whereas a thick-skinned extensional basin (right) shows a positive anomaly because of the mantle topography. A "hybrid" basin (bottom), forms by a combination of the two processes, is isostatically undercompensated and is characterised by a relatively low-amplitude free-air gravity signature.

°C isotherm, suggesting that the plate progressively increases its rigidity while cooling (Watts, 1978, 1992). For some time, it was thought that continental T_e behaves in the same manner and the cooling-plate model was applied in studies of rift basins to explain, for example, coastal onlap patterns at passive continental margins and the formation of steer's head basins (Watts, 1982; Watts *et al.*, 1982; Karner, 1991). These authors have argued that the continental lithosphere should become increasingly rigid in response to sediment loading, although local isostasy may prevail during the rifting phase. In some areas such as the North Sea, T_e is generally small (< 5 km) (Barton and Wood, 1984), while in some rift settings such as in East Africa, T_e may exceed 20 km (Ebinger *et al.*, 1991). The Baikal Rift Zone was found to have $T_e = 50$ km (Ruppel *et al.*, 1993). Recent studies have found that continental T_e may be related more to compositional variations rather than the cooling history. There seems to be a strong link with the *present-day heat flow*; for example, in Africa, low T_e correlates with regions of high heat flow whereas high T_e correlates with regions of low heat flow (Hartley *et al.*, in press). Ruppel *et al.* (1993) suggested that the high T_e value found in the Baikal Rift may be a result of cold lithosphere. One explanation is that the mechanical behaviour may be controlled by the distribution of radiogenic heat-producing elements in the crust (Watts, 1992).

The results from the Malay Basin agree, in general, with the suggested correlation between T_e and heat flow. The high present-day heat flow (>84 mW m^{-2}) may explain the very low T_e, almost approaching Airy isostasy. We could not, however, determine the exact value of T_e based on the available data. It is difficult to resolve $T_e < 5$ km for wide basins such the Malay Basin, which is >300 km wide. Figure 5.26 shows the relationship between the basement response function, $\Phi(k)$, and load wavelength, λ. The figure suggests that, for $T_e < 12$ km, basins wider than about 200 km ($\lambda = 400$ km) should have $\Phi(k)$ approaching unity and will tend towards local (Airy) isostasy. The Penyu Basin, on the other hand, is only about 150 km wide ($\lambda = 300$ km) and, therefore, the lithosphere behaves slightly more rigidly to such a load. Φ is about 0.9 in the Penyu Basin (Fig.

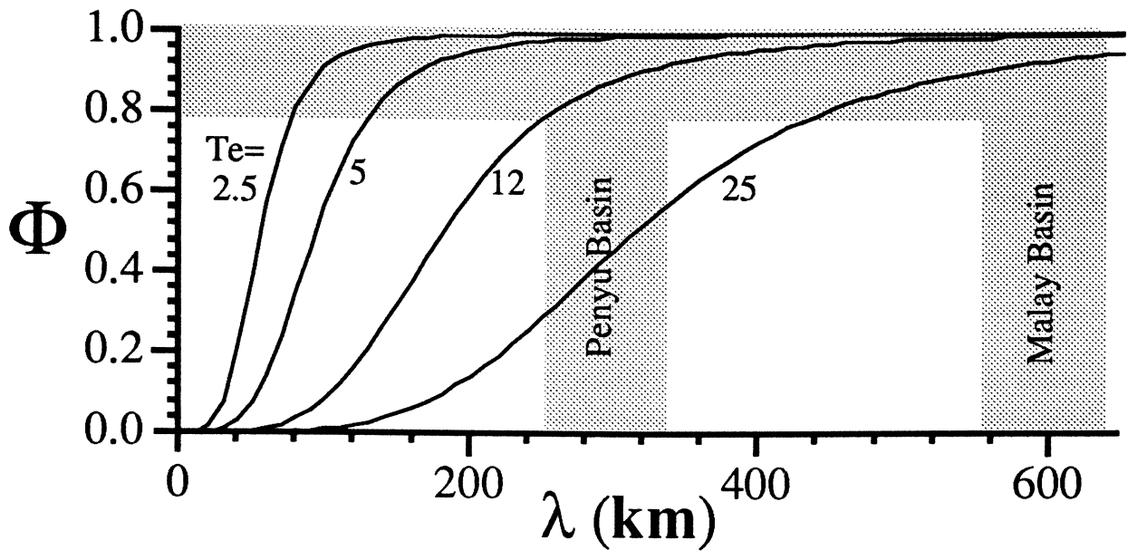

Figure 5.26. Basement response function, Φ, *vs* load wavelength, λ, plotted for various T_e values. ρ_{infill} is assumed to be $\rho_w = 1030$ kg m^{-3} (see equation 5.5). Shaded areas represent the approximate wavelengths and corresponding response function for the Malay and Penyu Basins.

5.26). Recent compilation by Watts (1992) showed that continental T_e can be anything between 5 and 110 km, with apparently bimodal distribution peaking at 10–20 km and 80–90 km. The value obtained from the Penyu Basin lies within the shallower range of T_e values. No previous determination of T_e has been made in the Southeast Asian region to make a comparison.

There may be other reasons why the Malay Basin shows very low T_e. The Basin is filled with more than 10 km of sediments mostly within a very narrow area. Hence, the plate is highly curved in the vertical plane by strong sediment loading, which must result in high bending stress. If the bending stress exceeds the failure criterion, the lower part of the lithosphere may decouple from the upper brittle layer, which will fail by brittle faulting and cause a drastic reduction in the elastic thickness (McNutt *et al.*, 1988).

The presence of strike-slip faults that penetrate the entire brittle crust, or even the lithosphere, could also result in weakening of the elastic layer, and will result in a "broken plate" behaviour. Depending on the value of T_e and the load geometry, flexure of a broken plate is roughly twice that of a continuous plate

of the same rigidity (Turcotte and Schubert, 1982). This could also explain the anomalous subsidence seen in the gravity modelling results.

5.5 Conclusions

The main conclusions derived from the gravity modelling study in this chapter are

1. Low-amplitude free-air gravity anomalies (−20 mGal) over the Malay and Penyu Basins were successfully modelled using flexural backstripping and gravity modelling techniques. The modelling results suggest that the Basins are underlain by relatively thinned crust, suggesting formation by a process that involved whole-lithospheric stretching.

2. Free-air anomaly and sediment thickness data showed that the Malay and Penyu Basins are not in complete isostatic equilibrium. The gravity anomaly can not be explained by a simple model of crustal thinning alone. The Moho topography required to compensate for the density contrasts due to the sedimentary basins is 20–30% deeper than that predicted by the Airy isostatic model.

3. Lower than expected Moho depth means that the crust beneath the Basins may not be as thin as expected, given that the total backstripped tectonic subsidence is >5 km. Two alternative explanations have been considered. One is that the apparent thickening of the crust may have resulted from magmatic underplating. To account for the discrepancy between the predicted and isostatic Moho depths, which should represent the thickness of the underplating material, underplating must have involved a greater-than-normal asthenosphere potential temperature (>1380°C), perhaps associated with a mantle plume. Underplating is considered unlikely, however, on the grounds that the anticipated uplift (about 0.75 km), which would have re-

sulted from the addition of less-dense material at the base of the crust, is not observed. The apparently low β ($\sim$2.5) is insufficient to have generated a large amount of melt. Even if the asthenosphere potential temperature was higher than normal, the effect of finite-duration rifting (Chapter 6) would have significantly reduced the chance of generating enough melt that can explain the apparent increase in crustal thickness.

A more plausible explanation is that part of the crustal extension, which caused the subsidence, did not involve stretching of the mantle lithosphere. The extension in the upper crust may have been detached from the lower crust and lithosphere ("thin-skinned") or associated with strike-slip faulting during the Basins' evolution, and resulted in subsidence that is uncompensated by mantle upwelling.

4. The stretching factor, β, was estimated from the crustal structure reconstructed from the gravity models. The value of this estimate depends, however, on the choice of model used to explain the partial compensation. If the underplating model is correct, β at the centre of the Basin is about 3.4. However, because the evidence is more in favour of the strike-slip hypothesis, the amount of crustal thinning, β, may be only about 2.3. These values represent the most likely range of β in the Basins.

5. The results show that the lithosphere here has a very low flexural rigidity (T_e $<$ 12 km). The Malay Basin, being a very wide basin, shows compensation that approaches Airy isostasy. Hence, the assumption of Airy isostasy in 1D-backstripping analysis in that Basin (Chapter 6) is justified. For the Penyu Basin, however, subsidence analysis has to take into account the T_e value of 12 km.

symbol	value	paramater
ρ_w	1030 kg m^{-3}	density of water
ρ_c	2800 kg m^{-3}	density of crust
ρ_m	3330 kg m^{-3}	density of mantle
ρ_s	2400 kg m^{-3}	density of sediment
ρ_g	2680 kg m^{-3}	average sediment grain density
y_c	31.2 km	initial crustal thickness
E	100 GPa	Young's modulus
ν	0.25	Poisson ratio
g	9.81 m s^{-2}	gravitational acceleration
α	3.28×10^{-5} °C^{-1}	thermal expansion coefficient
T_o	1330 °C	temperature of mantle
a	125 km	thermal thickness of lithosphere
$a^2/\pi^2\kappa$	62.75 Ma	thermal time constant
κ	8.0×10^{-7} m^2 s^{-1}	thermal difussivity of lithosphere
k_b	3.14 W m^{-1} K^{-1}	thermal conductivity of lithosphere
k_bT_o/a	33 mW m^{-2}	equilibrium heat flux
k_w	0.6 W m^{-1} K^{-1}	thermal conductivity of water
k_g	2.1 W m^{-1} K^{-1}	thermal conductivity of sediment grain

Table 5.2. Modelling parameters used in gravity and subsidence/heat flow modelling (Chapters 5 and 6).

Chapter 6

Subsidence and Heat Flow

This chapter discusses the subsidence and thermal histories of the Malay/Penyu Basins based on analysis of stratigraphic and temperature data compiled from previously unpublished sources, which include numerous unpublished reports, well-completion records, and maps. The analysis of subsidence involves the following

1. Compilation of temperature and heat flow data in the Basins to investigate the magnitude of the heat flow anomaly associated with lithospheric extension and for later comparison with thermal history modelling.

2. One-dimensional backstripping of well data, following the method described by Sclater and Christie (1980), to determine the tectonic subsidence history of the basement and for the estimation of stretching factors by comparing with theoretical curves from the stretching model (McKenzie, 1978).

Estimates of β obtained in the subsidence analysis are used in the modelling of the temperature history of the Basin. Basins that form by stretching of the lithosphere thermal boundary layer show, typically, heat flow that decays with time, which is related to cooling of the underlying asthenospheric thermal anomaly (McKenzie, 1978; Jarvis and McKenzie, 1980; Cochran, 1983), Fluctuations in heat flow anomalies can occur at any time during the basin's history, for example, as a result of a later stretching phase or a magmatic event, which may complicate the interpretation of heat flow history. Because the maximum temperature attained by sediment is governed by the basal heat input from the basement (basal

heat flow), the temperature history of the sediment contains useful information about the extent of lithospheric thinning/stretching in extensional basins. In a later section of this chapter, sediment maturation data from the Malay Basin are used to investigate its temperature history. Burial history curves generated by backstripping sediment column at selected well locations were used to calculate the time-temperature history of the sediment, which is compared with the results of subsidence and heat flow analyses.

6.1 Geothermal Gradient and Heat Flow

In this section, the temperature and heat flow data from the Malay and Penyu Basins, which are relevant to the present analysis, are reviewed. Present-day geothermal gradients in sedimentary basins are estimated, usually, from measurements of mud temperatures during logging runs (bottom-hole temperatures or BHTs) or measurements of formation-fluid temperatures during repeat formation tests (RFTs), drill-stem tests (DSTs) and production tests (PTs). Subsurface temperatures measured during DSTs and PTs are generally considered to be the most reliable (Hermanrud *et al.* 1990, 1991) and are normally used without further correction. Temperatures obtained by other methods need to be corrected to the true formation temperatures, using various correction techniques (*e.g.* Waples and Ramly, in press). The corrected subsurface temperatures are then used to calculate the geothermal gradients required for estimating surface heat flows.

Early estimates of the geothermal gradient in the Malay Basin were made by Matsubayashi and Uyeda (1980) based on BHTs in eight exploration wells. This was followed by the work of Wan Ismail (1984) who used a more extensive data base consisting of 49 wells and thermal conductivity measurements from over 650 core samples. In that study, temperature gradients were calculated from BHTs corrected using the "standard" method (*e.g.* Evan and Coleman, 1974). Later, Wan Ismail (1990) expanded the data base to include PT data from 23 wells.

The Malay Basin temperature data base was updated recently by Mohd Firdaus (1993).

Well	Geothermal gradient (° C km^{-1})	Heat flow (mW m^{-2})
Pari-1	37.3	71
Merchong-1	43.1	82
Rumbia-1	43.5	82
Rhu-1/1A	46.0	87
Cherating-1	46.8	89

Table 6.1. Present-day geothermal gradient and heat flow in six Penyu Basin wells, based on bottom-hole temperatures (BHTs). Average thermal conductivity of 1.9 mW m^{-2}, based on data from Wan Ismail (1984), was used in the calculation. From the data, the average gradient is 43.3 °C km^{-1} and average heat flow is 82 mW m^{-2}.

In this study, data from Wan Ismail (1984, 1990) and Mohd Firdaus (1993), and data from well-completion logs were compiled. If the BHT-derived data are compared with PT-derived data (Wan Ismail, 1990; his Table 3), we find that the normal method of correcting BHTs underestimates formation temperatures by as much as 20%. Recently, Waples and Ramly (in press) carried out a statistical analysis of all the available data in the Malay Basin and recommended that a standard correction of +16% be added to BHT-derived temperatures. Hence, when available, DST and PT data are used in preference to temperature measurements from other sources. Figure 6.1 shows examples of the temperature-depth plots using DST data from six wells in the southern Malay Basin. Temperatures from sources other than DST or PT were corrected upwards by +16% as recommended. Data from more than 110 wells were compiled. Figure 6.2 is a map of the geothermal gradient based on the compiled data set. Geothermal gradients are, generally, in the range between 45 and 60 °C km^{-1}, with some wells in the centre having values exceeding 70 °C km^{-1}. It should be emphasized that heat flow estimates derived from temperature measurements at well locations may be biased because they record abnormal temperatures in oil or gas-bearing structural highs, which are strongly influenced by convection of hydrothermal basinal fluids (see, for example, Jones and Majorowicz, 1987). Nevertheless, the results are comparable

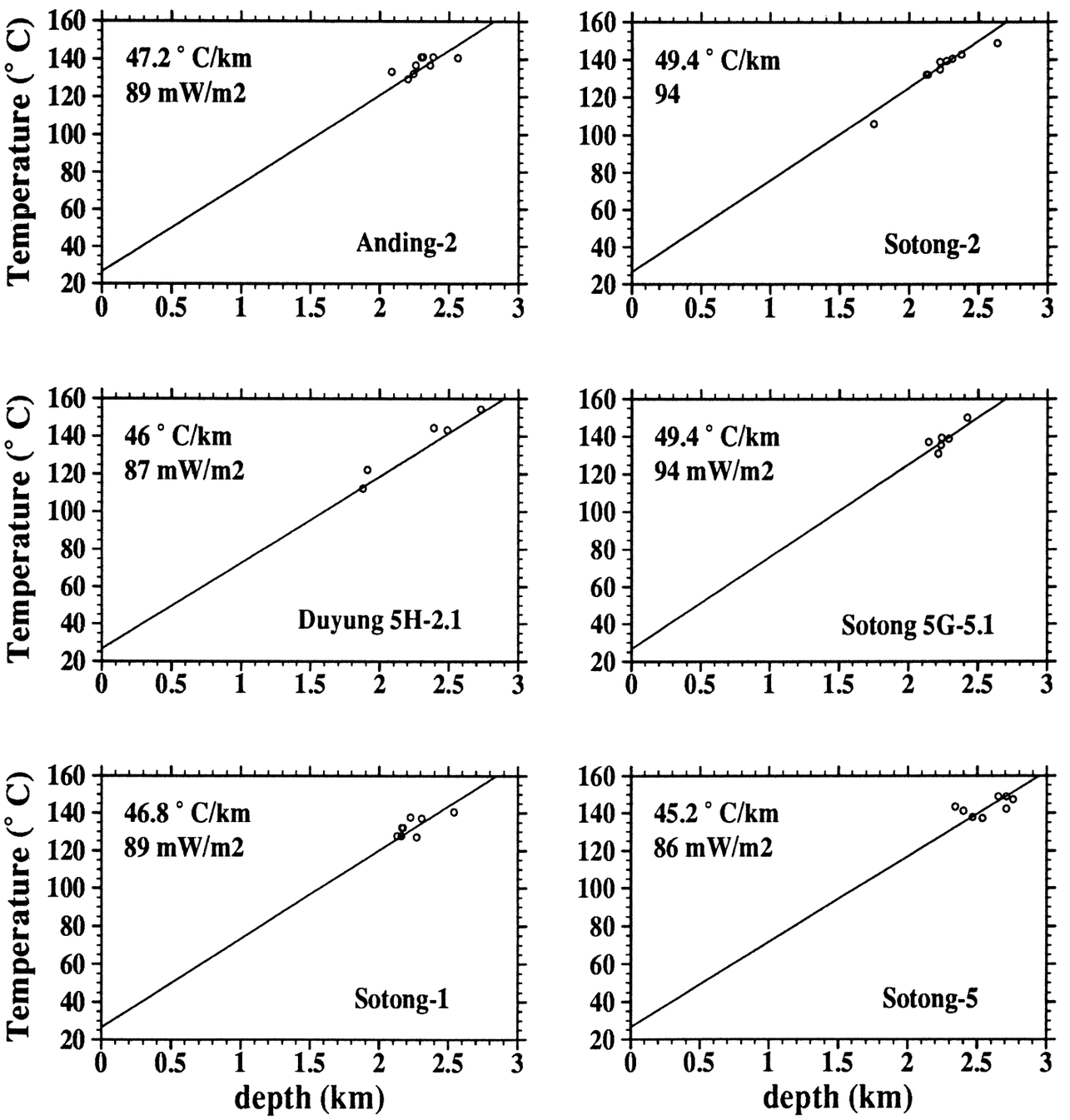

Figure 6.1. Geothermal gradient and heat flow in six wells in the Malay Basin, based on drill-stem test (DST) data. Heat flow was calculated using average thermal conductivity of 1.9 mW m^{-2}. A surface temperature of 26.6 °C is assumed, based on the mean annual surface temperature (Aadland and Phoa, 1981).

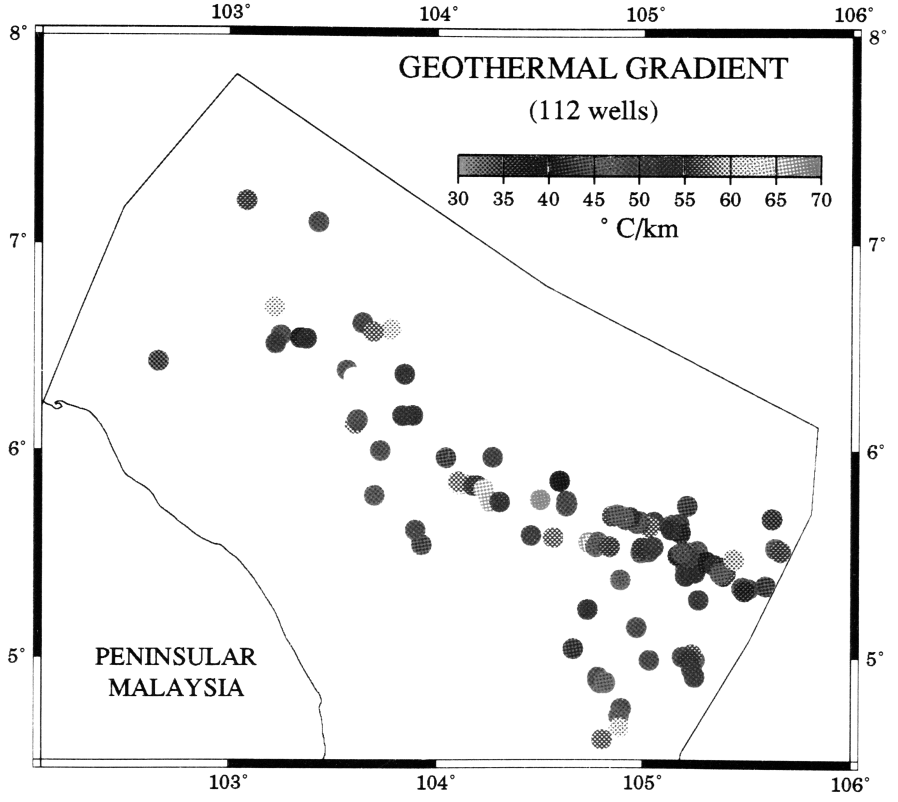

Figure 6.2. Temperature gradient in the Malay Basin. Data from 110 wells, compiled from various sources mentioned in the text.

with the regional heat flow pattern as reported in previous compilations of heat flow in the region (*e.g.* Aadland and Phoa, 1981; Rutherford and Qureshi, 1981). Hence, like other extensional basins of Southeast Asia (see Thamrin, 1985), the Malay Basin is characterised by abnormally high geothermal gradients, averaging 51 ± 8 °C km^{-1}, which corresponds to an average surface heat flow of about 96 mW m^{-2}.

For the Penyu Basin, BHTs in five wells, corrected using the same method as above, were used to calculate the average temperature gradient. Because no conductivity measurements exist for the Penyu Basin, the average thermal conductivity value for the southern Malay Basin is assumed when calculating the present-day heat flow. The results, tabulated in Table 6.1, show that the geothermal gradient is slightly lower than in the Malay Basin. The estimated heat flow in the Penyu Basin ranges between 71 and 88 mW m^{-2} and averages ~84 mW m^{-2}. For comparison, the average heat flow in the West Natuna Basin is 85 mW m^{-2} (Thamrin, 1985), while in the Pattani Basin (Gulf of Thailand) it is 93 mW m^{-2} (Hellinger and Sclater, 1983).

The surface heat flow observed in the Malay and Penyu Basin, and in the neighbouring basins, are significantly higher than the "global" average of ~67 mW m^{-2} (1.6 μcal $cm^{-2}s^{-1}$) (MacDonald, 1965). Such high heat flows are more typical of active back-arc, rift, or "thick-skinned" strike-slip basins rather than of a thermally-subsiding extensional basin such as the Malay Basin. Continental rift basins associated with mantle doming, for example those in East Africa (Wheildon *et al.*, 1994) and central Asia (Windley and Allen, 1993), are characterised by heat flows exceeding 100 mW m^{-2}. The Gulf of California, where present-day heat flow is about 110 mW m^{-2} (Sanchez-Zamora *et al.*, 1991), is probably a good example of a thick-skinned strike-slip basin formed by oblique plate convergence (Lyle and Ness, 1991), rather similar in terms of tectonic setting to the "back-arc" basins in Sumatra. However, because the Malay and Penyu Basins is <40 Ma old, the thermal anomaly caused by thinning of the lithosphere has not subsided

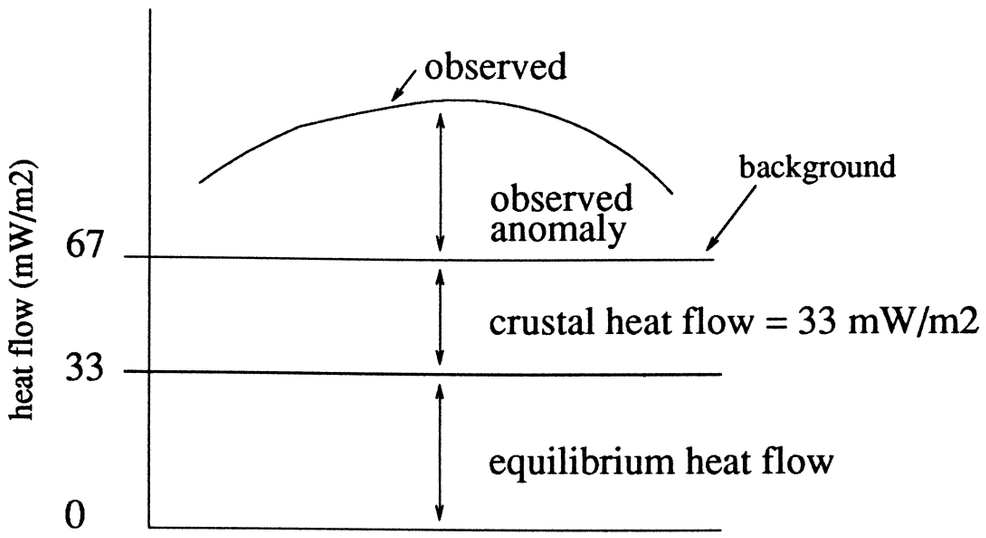

Figure 6.3. Schematic illustration between the various heat flow values.

completely.

This study attempts to explain the high heat flow in the Basins by examining the subsidence history of the Basins. The approach is to "forward-model" the heat flow using the stretching model and compare it with the observed heat flow. The observed present-day surface heat flow, Q_o, is considered to be the sum of several components

$$Q_o = Q_r + Q_c + \Delta Q \tag{6.1}$$

where Q_r is the "reduced" heat flow, *i.e.* the heat flow that would be observed in the absence of crustal heat production, Q_c is the crustal radiogenic heat flow, and ΔQ is the heat flow anomaly or excess heat flow resulting from lithospheric stretching. $Qr + Q_c$ may be regarded as "background" heat flow (Fig. 6.3). Because the theoretical heat flow calculated using the stretching model does not include the crustal contribution, we need to estimate the crustal heat flow, Q_c, and add it to the theoretical value before comparing it with the observed heat flow. The crustal heat flow can be estimated if the background heat flow is known.

To estimate the background heat flow, we require, ideally, heat flow data from regions outside the Basins where the lithosphere has not been stretched and, therefore, represents the pre-stretching background heat flow. Unfortunately,

Basin	°C km^{-1}	Basin	°C km^{-1}
South-west China	27	Sokong	56
South China shelf	41	NE Natuna	34
Gulf of Tonkin	40	West Natuna	38
Cagayan Valley	22	Penyu	38
Luzon Central Valley	24	Malay	45
Ragay-Samar	41	Gulf of Thailand	50
Visayan	31	South Andaman	33
Leyte	41	North Sumatra	47
Cotabato	18	Sibolga	24
Iloilo	21	Central Sumatra	61
South Mindoro	29	Bengkulu	24
West Palawan	22	South Sumatra	49
East Palawan	27	Sunda	46
Sandakan	28	Billiton	32
Tarakan	38	NW Java	46
Sabah	28	E Java	39
Baram Delta	28	Barito	36
Central Luconia	43	Kutei	32
Balingian	41	South Makassar	25

Table 6.2. Average geothermal gradient in Southeast Asian Tertiary basins, from Hutchison (1989a, p. 64). The data are used to estimate the "regional average" or background heat flow.

no data exists from the surrounding land areas or intrabasin structural highs. Even wells on the Tenggol Arch show high heat flow values, >84 mW m^{-2}. In previous compilations (*e.g.* Rutherford and Qureshi, 1981, Hutchison, 1989a), most of the heat flow data comes from the offshore basins, whose average heat flow depends on the tectonic setting and origin. Generally, extensional/back-arc basins such as the Pattani Trough and the Sumatra back-arc basins have very high heat flows of >80 mW m^{-2}, while the fore-arc and deltaic basins have low heat flows, <60 mW m^{-2}. In the absence of more reliable data, the background heat flow is estimated by taking the average temperature gradient of 38 basins in Southeast Asia compiled by Hutchison (1989a, his Table 3.1), excluding basins on the NW Australian continental margin. The data are reproduced in Table 6.2. The average temperature gradient derived from Table 6.2 is 35.4 °C km^{-1}. Using the average sediment conductivity for the Malay Basin (1.9 mW m^{-2}), we obtained a background heat flow of 67 mW m^{-2}. Hence, any deviation from this value in the Malay or Penyu Basin is interpreted as the heat flow anomaly, ΔQ, which should represent excess heat flow from lithospheric stretching. Because the equilibrium heat flow at the top of a 125 km lithosphere is 33 mW m^{-2} (assuming the parameters in Table 5.2, p. 196), the estimated crustal contribution, Q_c, to the background heat flow is about 33 mW m^{-2}. This value will be added to calculated heat flow when comparing with the observed heat flow (Fig 6.3).

6.2 Methodology

6.2.1 1D Backstripping

In this section, the method of backstripping used in the ensuing subsidence analysis is described. Backstripping (Watts and Ryan, 1976) is a technique used to quantify the tectonic subsidence of sedimentary basins by removing the effects of water and sediment loading. If the sedimentary fill is made up of a series of

sedimentary layers representing deposition during specific time intervals, backstripping enables the burial history of each layer in the sedimentary column and that of the basement to be traced through time. As each layer is "stripped" off, the thicknesses of the remaining layers are restored to their decompacted state by moving them up the porosity-depth curve. At every stage in the decompacting process, the depths to the top of the remaining sedimentary layers (palaeodepth) are calculated and recorded. The subsidence curve for the top of the basement so derived represents the basement subsidence resulting from a tectonic driving force, because the effects of water and sediment loading have been removed. This curve can then be compared with theoretical subsidence curves, such as those based on a model of lithospheric stretching (McKenzie, 1978), to estimate the amount of lithospheric thinning or stretching, β. The estimate of β is a useful parameter used in modelling the thermal history of the Basin (Section 6.5).

The backstripping equation is based on simple balancing of mass columns assuming Airy isostatic compensation (Fig. 6.4) and is similar to equation 5.8 (Chapter 5, p. 154). For a sediment layer of thickness Δh, the tectonic subsidence, ΔS, is given by (Steckler and Watts, 1978):

$$\Delta S = \Delta h \left(\frac{\rho_m - \rho_s}{\rho_m - \rho_w} \right) + W_d - \Delta d \left(\frac{\rho_w}{\rho_m - \rho_w} \right) \tag{6.2}$$

where W_d is paleowater depth, Δd is sea-level change, and ρ_m, ρ_w, and ρ_s are mean densities of mantle, water, and sediment, respectively. In the present study, because the Malay and Penyu Basins are, essentially, nonmarine throughout much of their history and because the sea-level history is unknown and is presumably unimportant, the effects of paleobathymetry and sea-level changes were ignored. Hence, the tectonic subsidence of a multilayered sedimentary column is

$$S_T = S^* \left(\frac{\rho_m - \rho_s}{\rho_m - \rho_w} \right) \tag{6.3}$$

where S^* is the total decompacted thickness of all the layers

$$S^* = \sum_i \left(\frac{1 - \phi_i}{1 - \phi_i'} \right) \Delta h_i \tag{6.4}$$

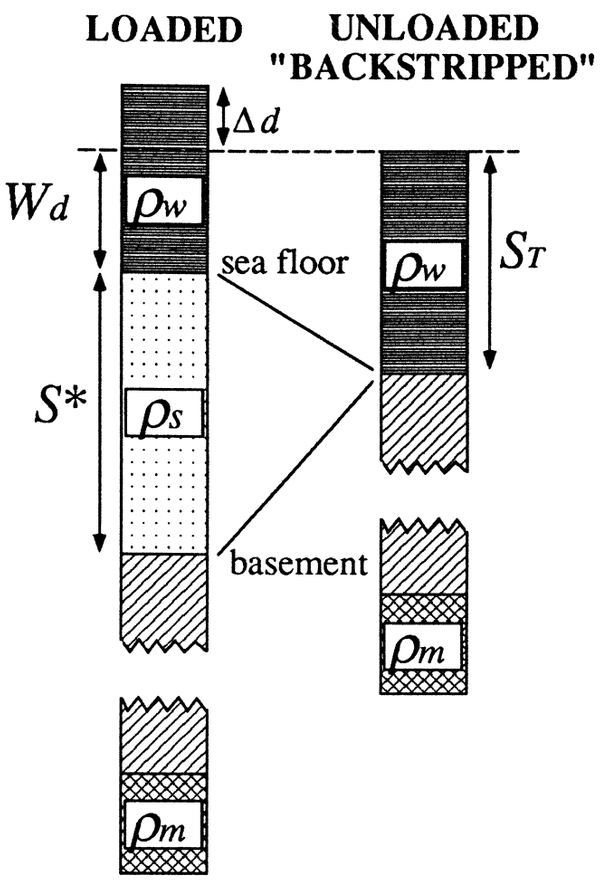

Figure 6.4. Illustration of the one-dimensional backstripping technique, which removes the loading effect of a sediment pile of thickness S^* and calculates the unloaded depth to the basement S_T. Symbols explained in the text. Redrawn from Steckler and Watts (1978).

Δh_i is the thickness of layer i, ϕ_i is its porosity before decompaction while ϕ_i' is porosity corrected for compaction. The average sediment density, ρ_s, is obtained by averaging the densities of the constituent sediment layers in the column at a particular time:

$$\rho_s = \frac{1}{S^*} \sum_i \left[\phi_i' \rho_w + (1 - \phi_i') \rho_g \right] \Delta h_i \tag{6.5}$$

where ϕ_i is the mean porosity of layer i and ρ_g is the mean sediment grain density (Table 5.2, p. 196). Note that, the value of S_T in equation 6.3 represents the elevation of the basement with respect to the present-day mean sea level. Hence, if the basement surface was initially above sea level, that part of subsidence that occurred above sea level is not recorded.

To calculate the thicknesses of sedimentary layers when unloading the base-

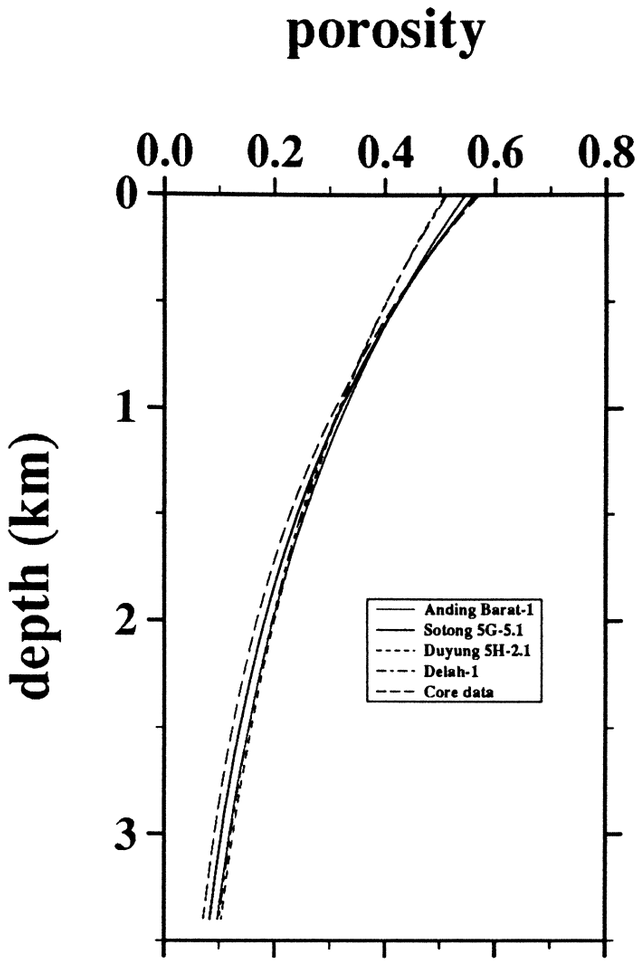

Figure 6.5. Porosity vs depth plot derived from sonic logs in four wells in the southern Malay Basin, using equation A.4. In all cases, $\Delta t_{ma} = 59\mu$/ft, $x = 2.095$. Core data are plotted for comparison. (Details given in Appendix A.2, p. 282).

ment, porosity reduction during burial is assumed to follow the exponential porosity-depth relationship (Athy, 1930):

$$\phi(z) = \phi_o e^{-cz} \tag{6.6}$$

where ϕ_o is the porosity at the surface and c is the porosity decay constant. The values $\phi_o = 0.55$ and $c = 0.51$ km^{-1} were empirically determined from sonic logs in a number of wells from the southern Malay Basin (Fig 6.5). Details are given in Appendix A.2. Sediment compaction is treated as one-dimensional in the vertical direction, *i.e.* no material movement in the horizontal direction. It is assumed also that basement rocks are fully compacted. This relationship is assumed to apply throughout the life of the basin and is independent of lithology.

6.2.2 Subsidence and Heat Flow Modelling

To calculate theoretical subsidence curves for comparison with the subsidence history obtained by backstripping, the one-dimensional uniform stretching model developed by McKenzie (1978) was used. The calculations were done using a computer program XRIFT, which is based on a modified stretching model that takes into account a finite rifting duration and, optionally, the effects of lateral heat conduction for modelling two-dimensional basins (Cochran, 1983). The basic feature of McKenzie's model was introduced in Chapter 1. A full description of the mathematical model and program structure is given in Appendix B.1. The core of the program calculates the temperature structure, $T(z,t)$, of the lithosphere following an instantaneous uniform stretching event (Fig. 6.6) by solving the one-dimensional heat flow equation:

$$\frac{\partial T}{\partial t} = \kappa \frac{\partial^2 T}{\partial z^2} \quad 0 \leq z \leq a \tag{6.7}$$

where z is the vertical coordinate measured positive downwards, t time, a the lithospheric thickness, and κ the thermal diffusivity of the lithosphere. The values of the relevant parameters are given in Table 5.2 (p. 196). For the finite rifting calculations, following the approach of Cochran (1983), the rifting period is treated as a series of instantaneous rifting events, each followed by a thermal relaxation period of 0.5 Ma duration. The subsidence and heat flow (equations B.7 and B.10, Appendix B.1) for finite-duration rifting are calculated in the same way as in the instantaneous model but the temperature structure of the lithosphere has to be evaluated after each short rifting event.

Examples of the theoretical (water-filled) subsidence for a range of β values are shown in Fig. 6.7A. The most important effect of a finite rifting duration is that a portion of the thermal subsidence occurs during the stretching phase, thus, enhancing subsidence during the stretching phase. Jarvis and McKenzie (1980) have found that the instantaneous rifting model is a sufficient approximation provided the rifting duration is less than ~20 Ma for β<2. They pointed out also

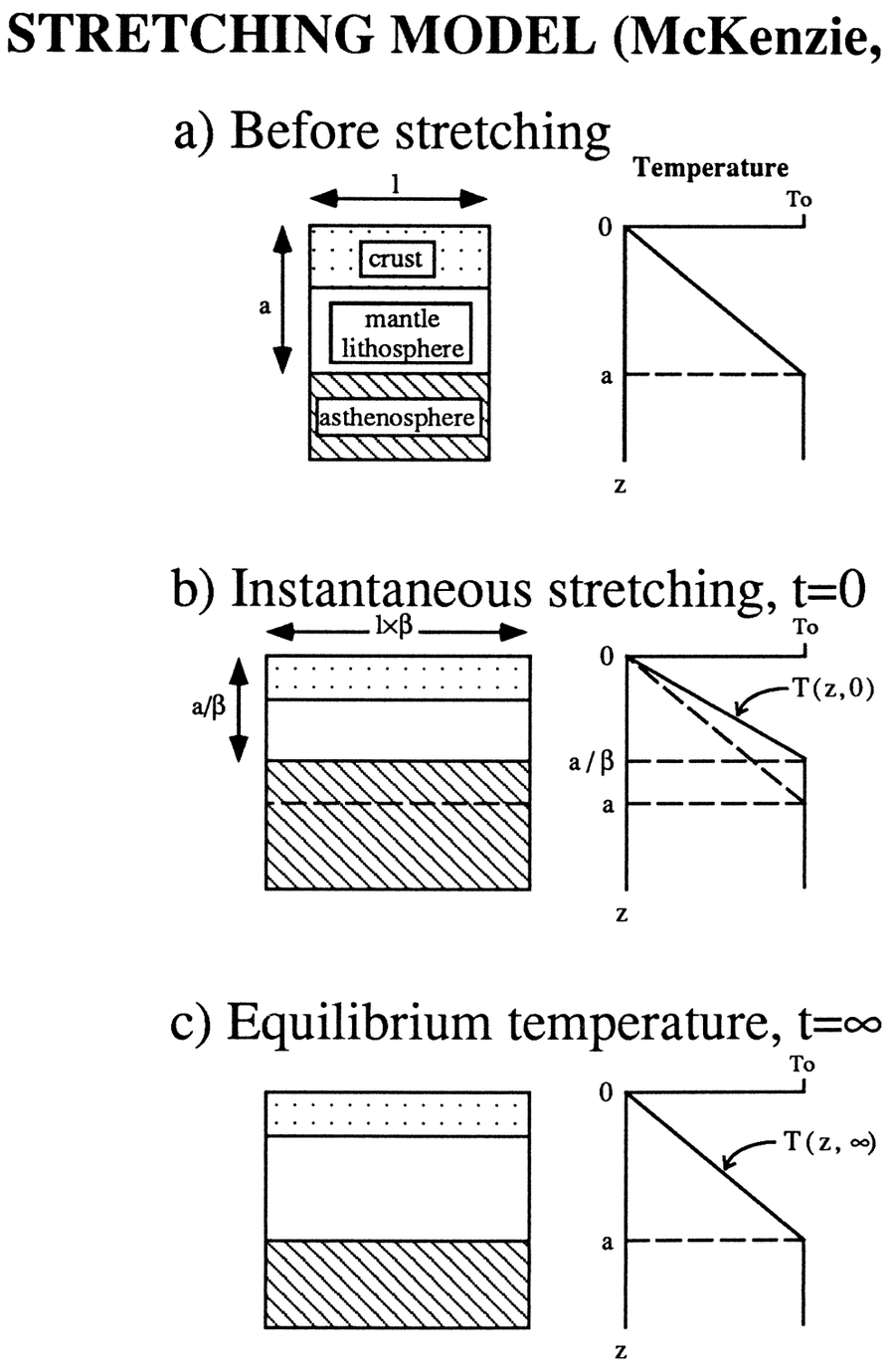

Figure 6.6. Simple model of lithospheric stretching and its effect on the temperature structure of the lithosphere (McKenzie, 1978). At time $t = 0$ (A), a segment of the lithosphere of length l is instantaneously extended to $l \times \beta$ (B). Graph shows schematically the higher temperature gradient as a result of thinning of the lithosphere to a/β. At time $\rightarrow \infty$ (C), the lithosphere relaxes to the its original pre-stretching temperature structure.

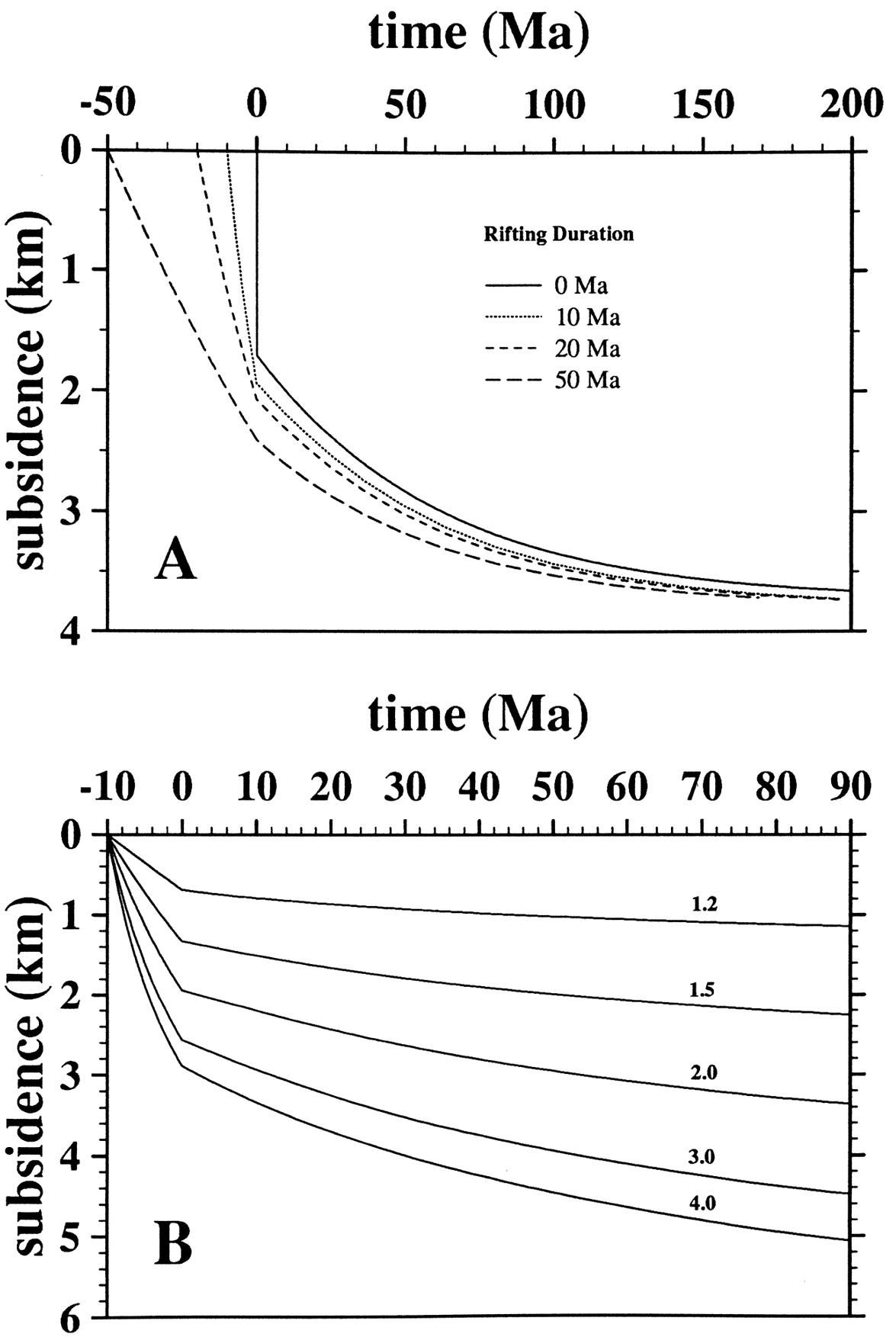

Figure 6.7. Theoretical subsidence *vs* time since end of rifting (0 Ma), based on finite-duration rifting model. (A) Various stretching duration for $\beta = 2$. (B) Various β for stretching duration of 10 Ma. Water is assumed to fill the basin in both cases.

that, if the heat flow history is also of interest, finite rifting duration needs to be taken into account as it may have a significant effect on the heat flow.

Figure 6.7B shows a series of subsidence curves calculated for various values of β and a stretching duration of 10 Ma, which is representative of the Malay and Penyu Basins. An important observation is made here. In the previous chapter, the maximum tectonic subsidence obtained by backstripping is ~5 km which, assuming an isostatic crustal model, corresponds to a crustal stretching factor of 3.4 (Fig. 5.23A, 188). From Fig. 6.7B, $\beta = 3.4$ gives only 3.6 km of water-filled subsidence after 25 Ma since rifting ended, 1.5 km less than the observed. Because it is unlikely that β can be higher than 3.4, this seems to support the hypothesis that part of the tectonic subsidence is uncompensated by crustal thinning, and could indeed be related to strike-slip tectonics.

6.3 Malay Basin: Results and Discussion

A total of 64 wells were chosen for analysis in the Malay Basin (Fig. 6.8). The stratigraphic data consists of depths to the top of seismic units; a complete list of the data is given in Appendix A.4. The chrono-stratigraphic ages of the units are based on the recent revision by Morley *et al.* (1994) (Table 6.3). There is relatively good well coverage of the southeastern and central parts of the Basin but poorer in the northeastern part because of less exploration activity there. Approximately a third of the wells shown in Fig. 6.8 penetrate the basement but most of them are located either on the Basin's flanks or in the shallower southeastern part of the Basin. For the majority of the wells, the depth to the basement is unknown and was estimated from the seismic-based depth map shown in Fig. 5.3 (p. 149). The age of the start of rifting in the Malay Basin is rather speculative, for no direct evidence from the oldest sediment is available. Published information from the West Natuna Basin (Daines, 1985) and comparison of the stratigraphy with other basins in the region suggests that the maximum age of the Basins is probably

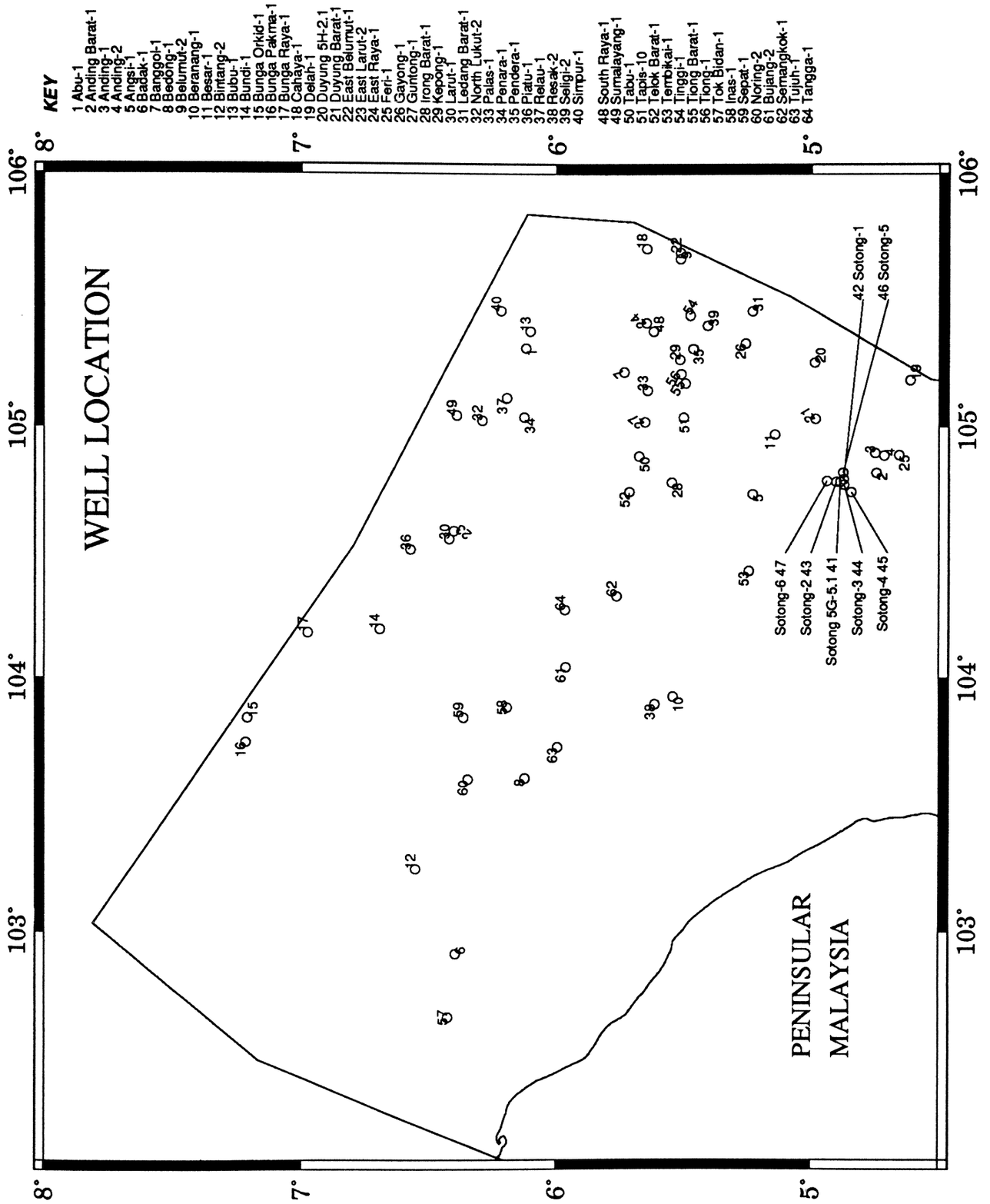

Figure 6.8. Location of wells for subsidence analysis in the Malay Basin. Wells are numbered in alphabetical order.

Top of Unit	Age (Ma)
A	0
D	7
E	8.7
F	12
H	15
I	17
J	19.3
K	20.9
L	24
M	26.3
Basement	35

Table 6.3. Age of seismic horizons in the Malay Basin (after Morley *et al.* 1994).

~40 Ma (late Eocene). This is probably a reasonable estimate, assuming that the Basin's formation was, in some way, related to the collision of India and Eurasia at ~45 Ma (Tapponnier *et al.*, 1982; Dewey *et al.*, 1989). Available biostratigraphic data (Rexilius *et al.*, 1992) also suggests that the oldest sediment (Unit M), is 35 Ma old (earliest Oligocene), which represents an upper bound on the age of the Basin. The end of rifting in the Malay Basin is roughly equivalent to the top of Unit M which, according to Morley *et al.* (1994), is 25 Ma. This is supported by seismic data (Fig. 4.18, p. 143), which shows that the end of fault-controlled subsidence and thickening of the half-graben fill corresponds with the top of Unit M. Hence, the rifting duration in the Malay Basins, based on the minimum and maximum possible ages of the start and end of rifting, is in the range of 10–15 Ma. This seems to be well within the time range acceptable for the instantaneous model (Jarvis and McKenzie, 1980).

To estimate the amount of lithospheric stretching (β), the backstripped subsidence curves were compared with theoretical curves calculated using the finite-duration rifting model, assuming rifting started at 35 Ma ago and lasted for 10 Ma. An initial crustal thickness, $y_c = 31.2$ km, was assumed such that the Basin was at sea level prior to stretching. The tectonic subsidence curve for each well is shown in Figs. 6.9 to 6.14. The results show that β lies generally between

~1.2 and 4.0. Wells on the northeastern flanks gave β values between 1.2 and 1.5, and, locally, as high as 2.0. Higher β values are found in the central-southeastern part of the Basin (Figs. 6.9, 6.10, and 6.12), where β is about 1.3 to 3.0. In the Sotong–Anding area, at the southwestern corner of the Basin, the value of β is rather consistent at about 1.35 (Fig. 6.13).

It is observed that the start of subsidence in wells located on the Basin's flanks does not coincide with the assumed age of rifting. Examples are Bunga Raya-1, Bubu-1 and Larut-1 (Fig. 6.9), where subsidence occurred at ~25 Ma, some 10 Ma after the start of rifting. This arises because the theoretical subsidence curves were constrained to pass through 35 Ma, which is assumed to be the time of rifting and is the minimum possible age for the Basin. We have also placed a constrain on the duration of rifting, which is 10 Ma, based on stratigraphic evidence. Figure 6.15 shows the subsidence curves for wells on both flanks of the Basin and the theoretical curves calculated without either of the two constrains. To fit the observed subsidence curves, a range of rifting ages, t_o, between 34 and 20 Ma B.P. and duration, dt, between 8 and 19 Ma, is needed. The maximum β however, is ~1.5, which is not significantly different from the results obtained when assuming a 35 Ma rifting age and a rifting duration of 10 Ma. It is concluded, therefore, that the errors involved in making these assumptions, which are based on stratigraphic evidence, is minimal.

6.3.1 Pre-Rift Crustal Thickening

If the assumptions discussed above are correct, we need to account for the delay in the subsidence for the wells on the flanks. As pointed out earlier in Section 6.2.1 (p. 205), backstripping gives the subsidence that occurs below sea level only. One possible reason for the apparent delay in subsidence is that the area might have been, initially, above sea level so that part of the subsidence occurred above sea level. This may have been the result of, either, thickening of the crust or thinning of the lithosphere prior to stretching 35 Ma ago. On isostatic grounds,

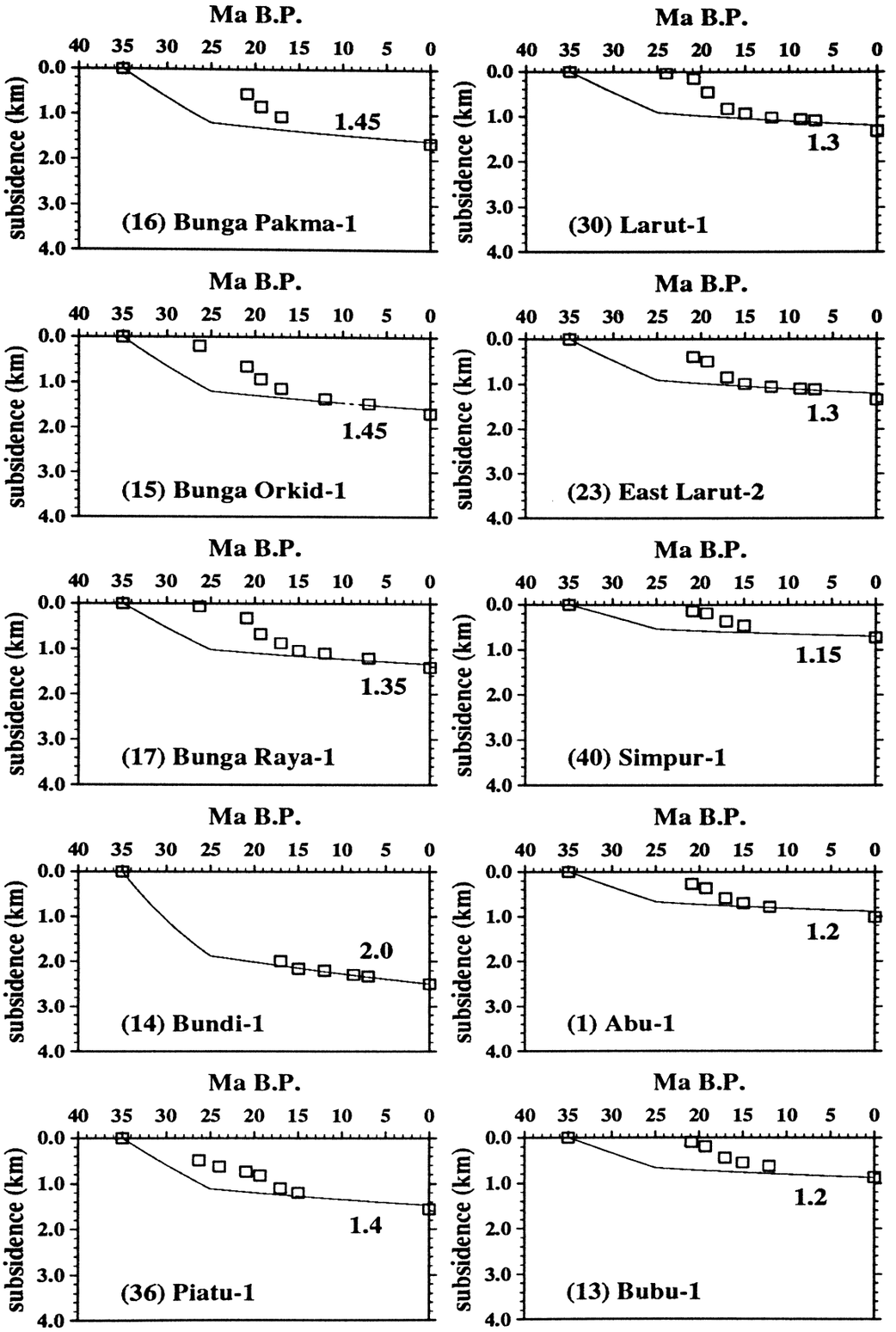

Figure 6.9. Backstripped tectonic subsidence (squares) for wells in the Malay Basin. Numbers in brackets refer to the well location in Fig. 6.8. Also plotted for each well is the best-fit theoretical curve with β value as indicated, assuming uniform stretching of the lithosphere at 35 Ma B.P. lasting for 10 Ma.

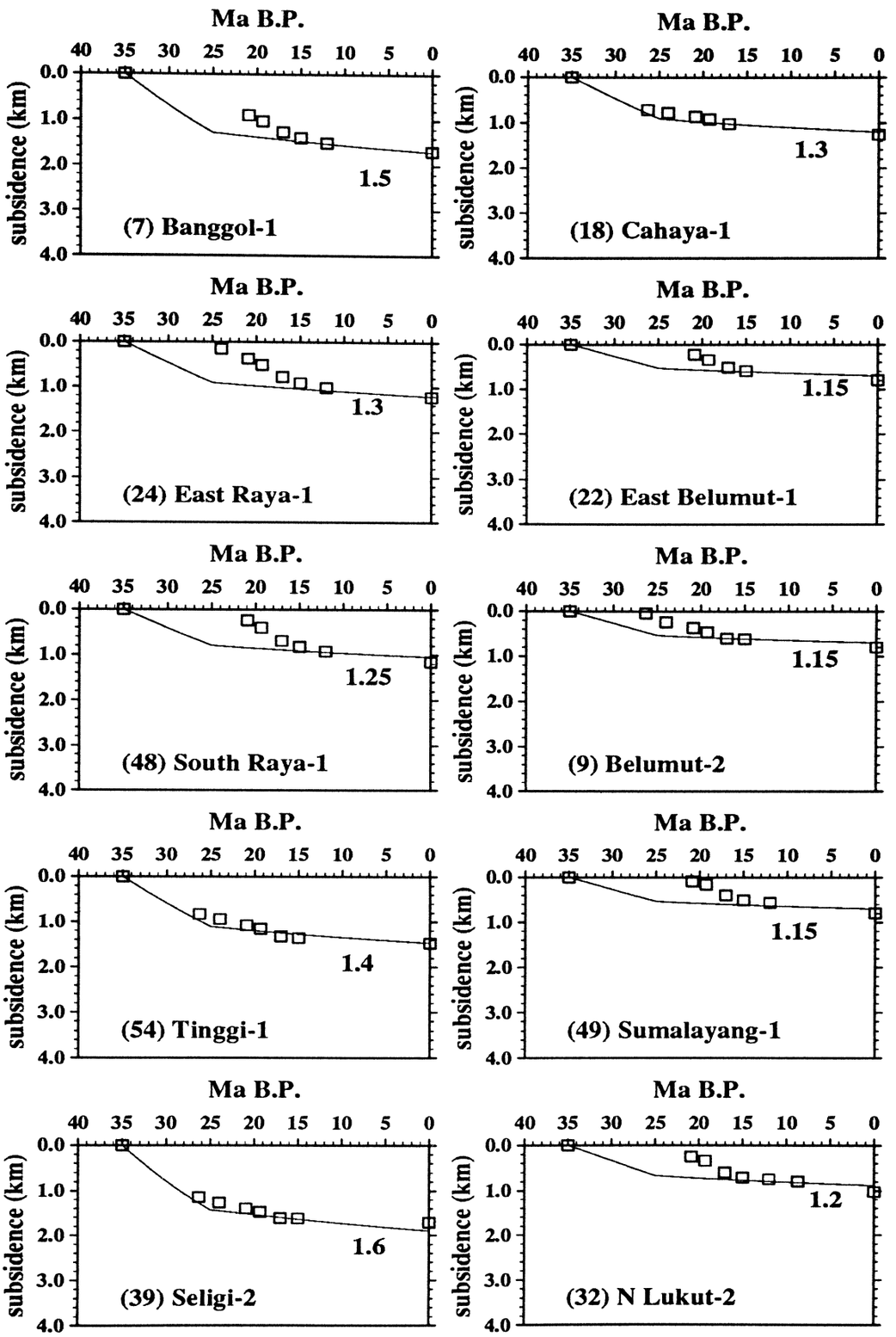

Figure 6.10. Backstripped tectonic subsidence (squares) for wells in the Malay Basin. Solid curve represents theoretical curve with β value shown. Numbers in brackets refer to the location in Fig. 6.8.

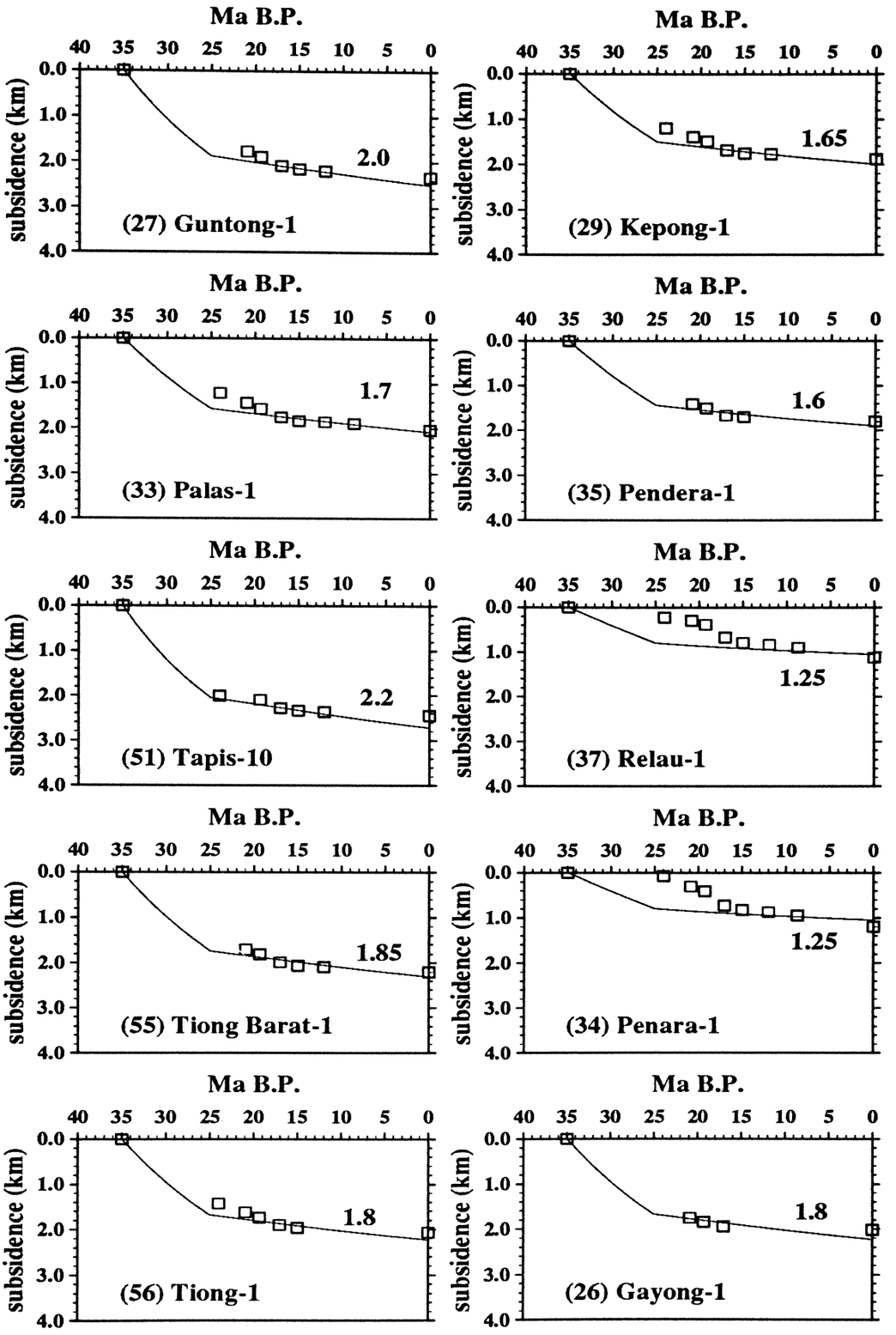

Figure 6.11. Backstripped tectonic subsidence (squares) for wells in the Malay Basin. Solid curve represents theoretical curve with β value shown. Numbers in brackets refer to the location in Fig. 6.8.

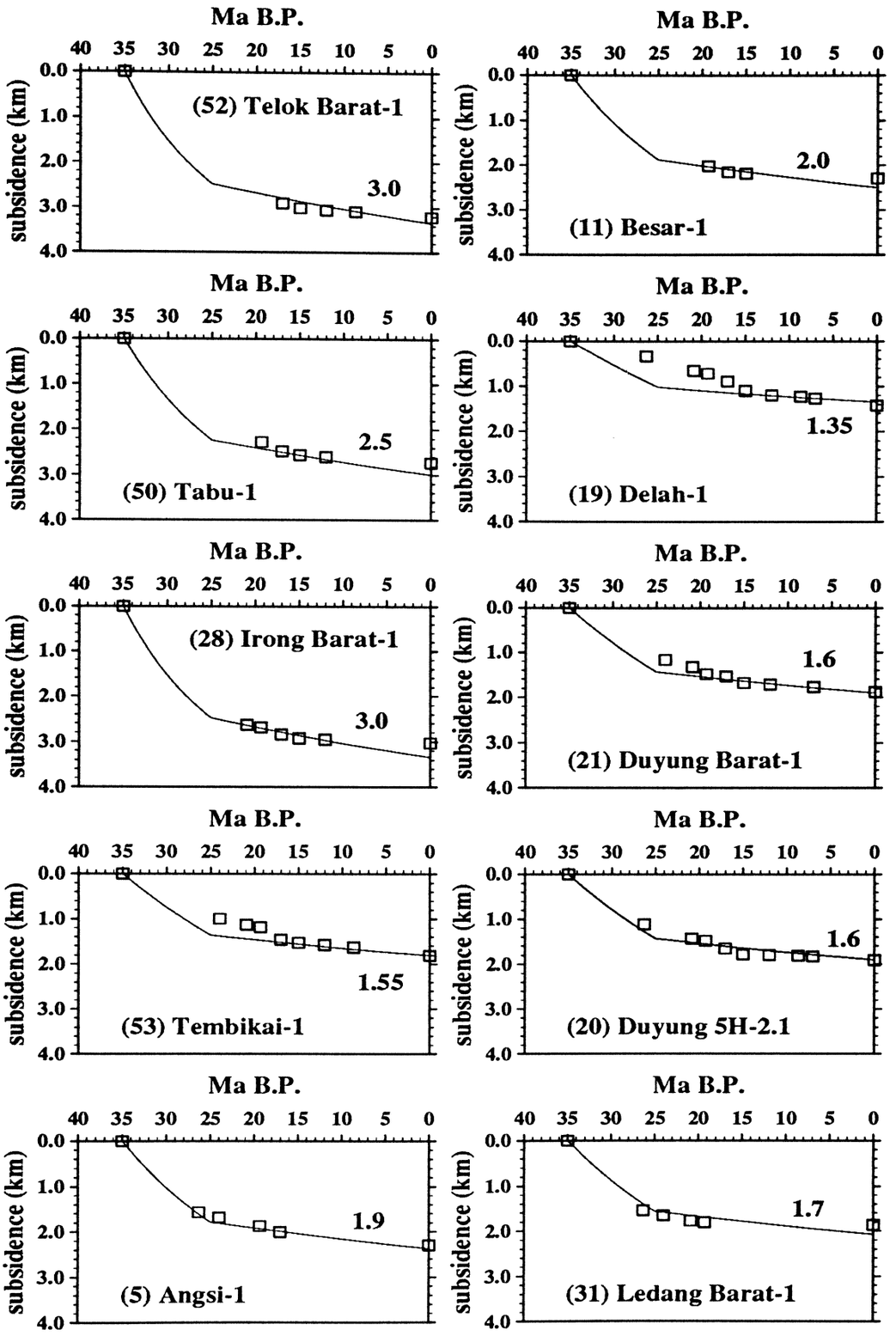

Figure 6.12. Backstripped tectonic subsidence (squares) for wells in the Malay Basin. Solid curve represents theoretical curve with β value shown. Numbers in brackets refer to the location in Fig. 6.8.

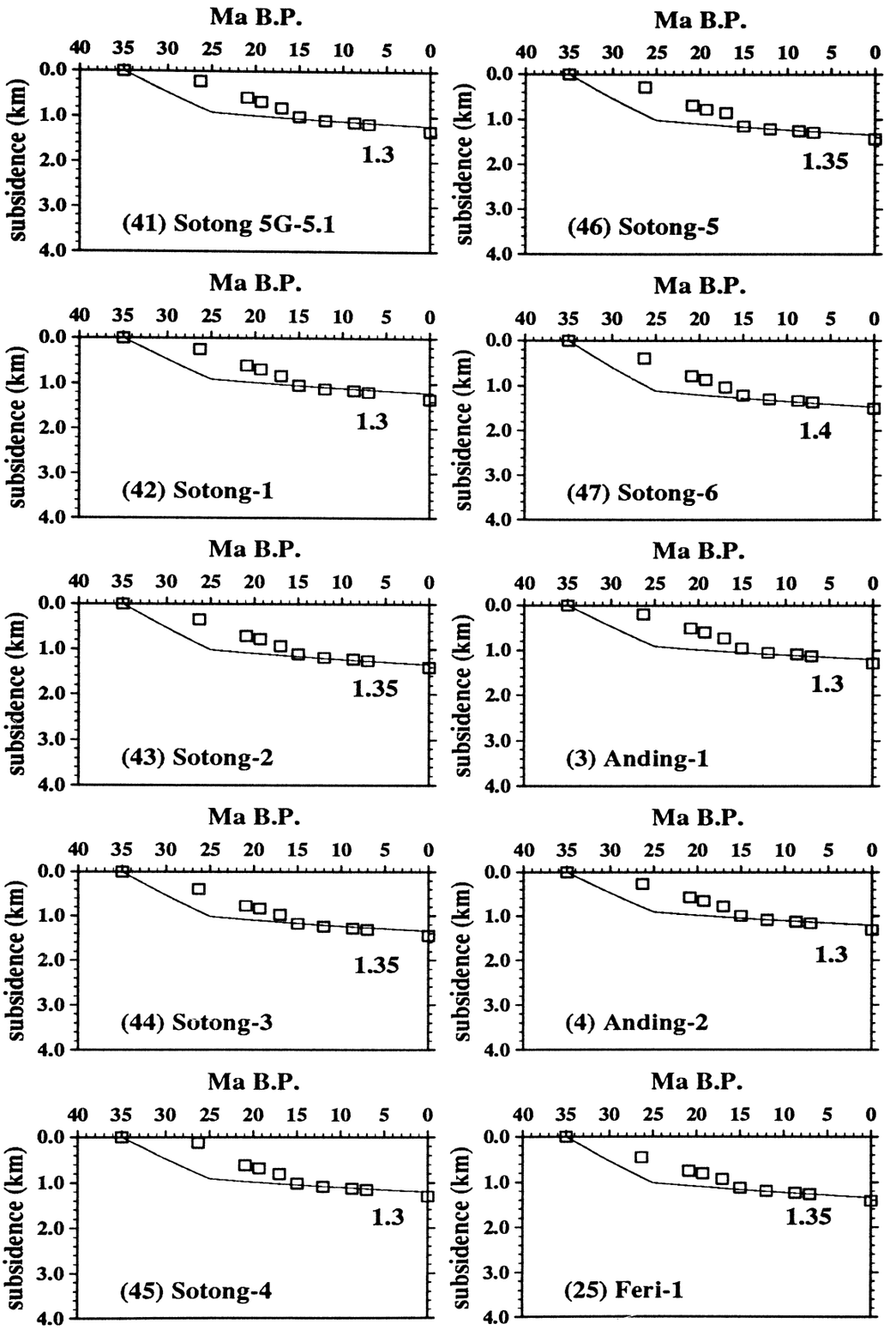

Figure 6.13. Subsidence curves in the Sotong Area. Solid curve represents theoretical curve with β value shown. Numbers in brackets refer to the location in Fig. 6.8.

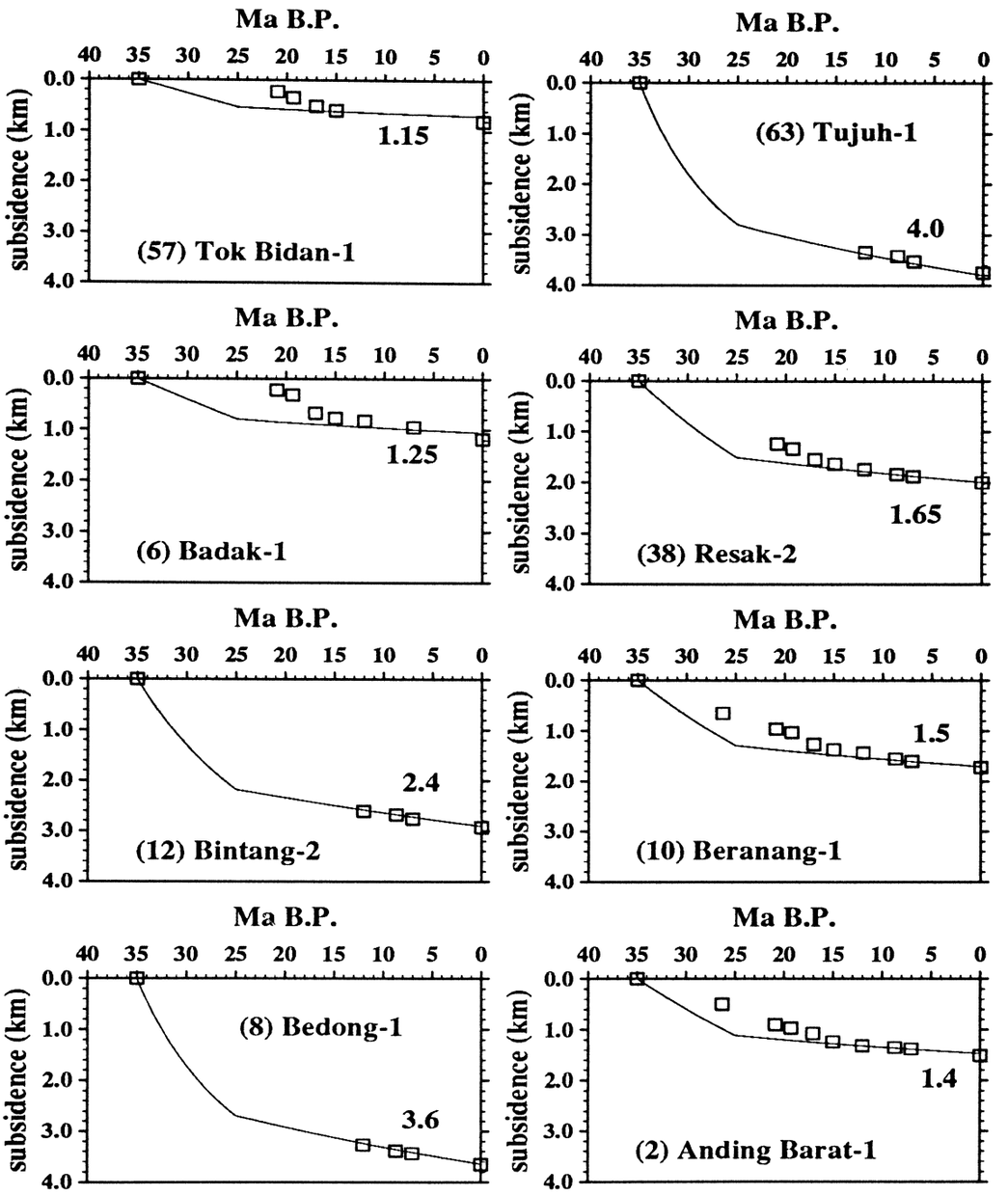

Figure 6.14. Backstripped tectonic subsidence (squares) for wells in the Malay Basin. Solid curve represents theoretical curve with β value shown. Numbers in brackets refer to the location in Fig. 6.8.

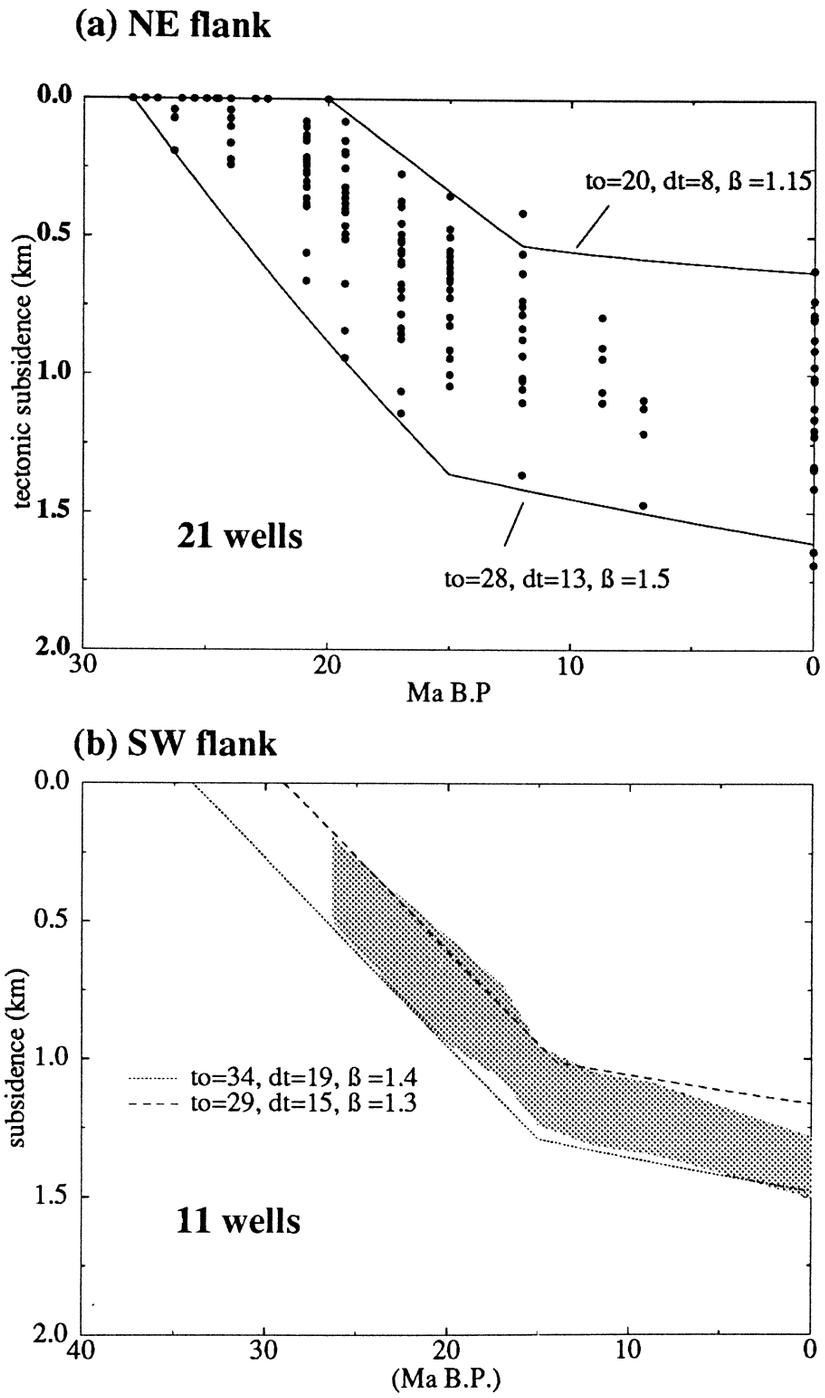

Figure 6.15. Subsidence curves from wells on the flanks of the Malay Basin. (A) NE flank (B) SW flank. Shown are the theoretical maximum and minimum finite-rifting subsidence curves calculated without *a priori* assumptions about the time of start of rifting, t_o, or the duration of rifting, dt. Results show t_o = 20–34 Ma B.P., dt = 8–19 Ma, β = 1.15–1.5.

a 40 km-thick crust and a 90 km-thick lithosphere would have a surface elevation of 1.17 and 0.55 km, respectively, relative to a normal crustal column that is in equilibrium with a mid-ocean ridge (Fig. 6.16). The regional geology (Chapter

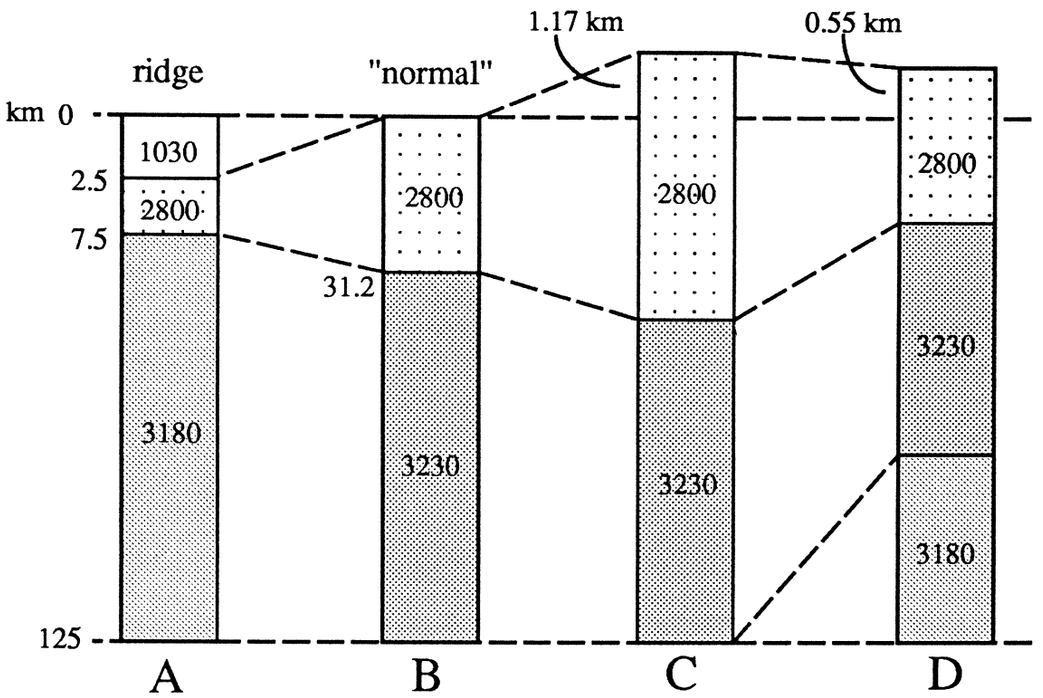

Figure 6.16. Elevation of lithospheric columns in isostatic balance with a mid-ocean ridge (A) with a 5 km-thick crust, 2.5 km below sea level. B respresents normal crust, C thickened crust of 40 km, and D thinned lithosphere of 90 km. Asthenosphere density (3180 kg m^{-3}) is calculated for a constant temperature T_o = 1330 °C, assuming density of basalt of 3330 kg m^{-3} at 0 °C and thermal expansion coefficient of 3.28 $\times 10^{-5}$ $°C^{-1}$.

2) suggests that the Sundaland region was the site of a major collisional orogeny and, thus, would be expected to have undergone crustal/lithospheric thickening. Hence, a model of crustal thickening seems to be the more plausible scenario. However, this would mean that the total subsidence, *i.e.* including the part which occurred above sea level, is greater by 1.2 km than that observed in the wells, and would require a higher β to explain it. For example, Fig. 6.17 shows the tectonic subsidence in Larut-1 compared with β curves calculated for a 40 km-thick crust whose initial surface elevation is 1.17 km. The figure shows that a higher β (= 1.5) is needed to fit the well data instead of 1.3 based on a normal crustal thickness of 31.2 km (dashed line). As suggested by the results of gravity modelling in Chapter 5, it is unlikely that the Basin's flanks had undergone such a high degree

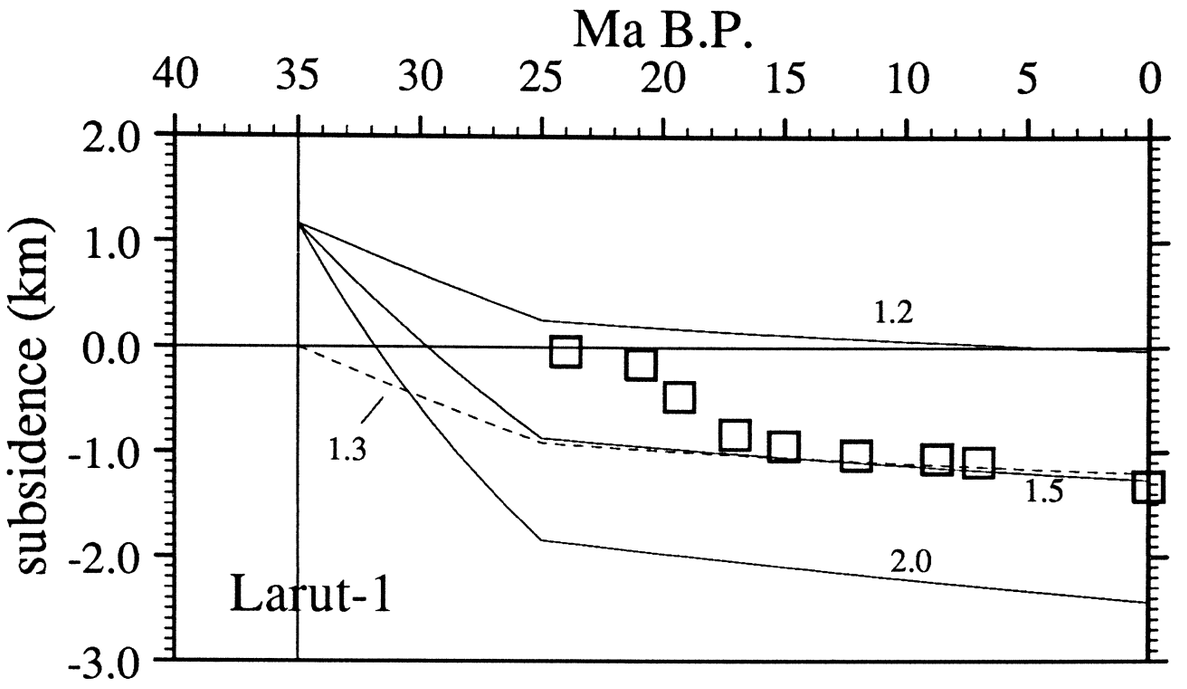

Figure 6.17. Subsidence model for initial crustal thickness of 40 km (solid curves) for Larut-1, compared with a "normal" model (dashed curve) that assumes 31.2 km initial crustal thickness. Boxes represent backstripped subsidence based on well data. Note that the initial surface elevation resulting from bouyancy of the thickened crust means that a higher β value is needed to explain the observed subsidence (1.5 as opposed to 1.3).

of crustal thinning.

6.3.2 Rift Flank Uplift

An alternative explanation is that the surface of the crust was at sea-level prior to stretching but the Basin's flanks were uplifted during the initial stretching phase while the central part of the Basin was undergoing subsidence. A number of processes could have caused uplift of the Basin's flanks during rifting, including non-uniform stretching of the lithosphere (Royden and Keen, 1980; White and McKenzie, 1988), flexural unloading in response to lithospheric stretching/necking (Braun and Beaumont, 1989; Weissel and Karner, 1989; Kooi *et al.*, 1992), and thermal

uplift arising from lateral temperature gradients due to stretching (Cochran, 1983; Steckler, 1985). Models involving flexural unloading of the lithosphere are unlikely because, as was found in Chapter 5, the flexural rigidity of the lithosphere is negligible.

Non-uniform stretching

If stretching in the mantle lithosphere is greater than that in the crust, relative uplift results because extra heat is being added to the crust. Using a two-layer instantaneous stretching model, Royden and Keen (1980, their fig. 3) showed that for "normal" thicknesses of lithosphere and crust (125 and 35 km, respectively) and a crustal stretching factor $\beta_c = 1.3$, initial uplift results if the mantle stretching factor is greater than about 3. This is because the greater mantle stretching results in a more elevated geotherm and, consequently, the thermal uplift exceeds the initial subsidence caused by the crustal thinning. In the Malay Basin, wells on the flanks show β values generally between 1.3 and 1.5, which agree with the gravity data. It is possible that these β values represent the crustal stretching factor, β_c, and that the subcrustal lithosphere may have been stretched by a larger amount.

Figure 6.18 shows a series of subsidence curves calculated using XRIFT for a rifting duration of 10 Ma but assuming a two-layer stretching model in the manner described by Royden and Keen (1980). β_c is fixed at 1.3, thought to be the average β on the flanks of the Basin, while β_m is varied to see its effect on the subsidence history. Because this is a 1D model, space problems associated with non-uniform stretching of the lithosphere is, for the time being, ignored. The figure shows that the subsidence during the early stages of rifting is significantly reduced as β_m increases, even after 100 Ma since the start of rifting. Uplift above sea level occurs during the rifting phase when β_m is greater than about 2.0–2.5. When β_m is about 3.0, subsidence below zero (sea level) is delayed by 10 Ma, which is similar to the observation in the Malay Basin.

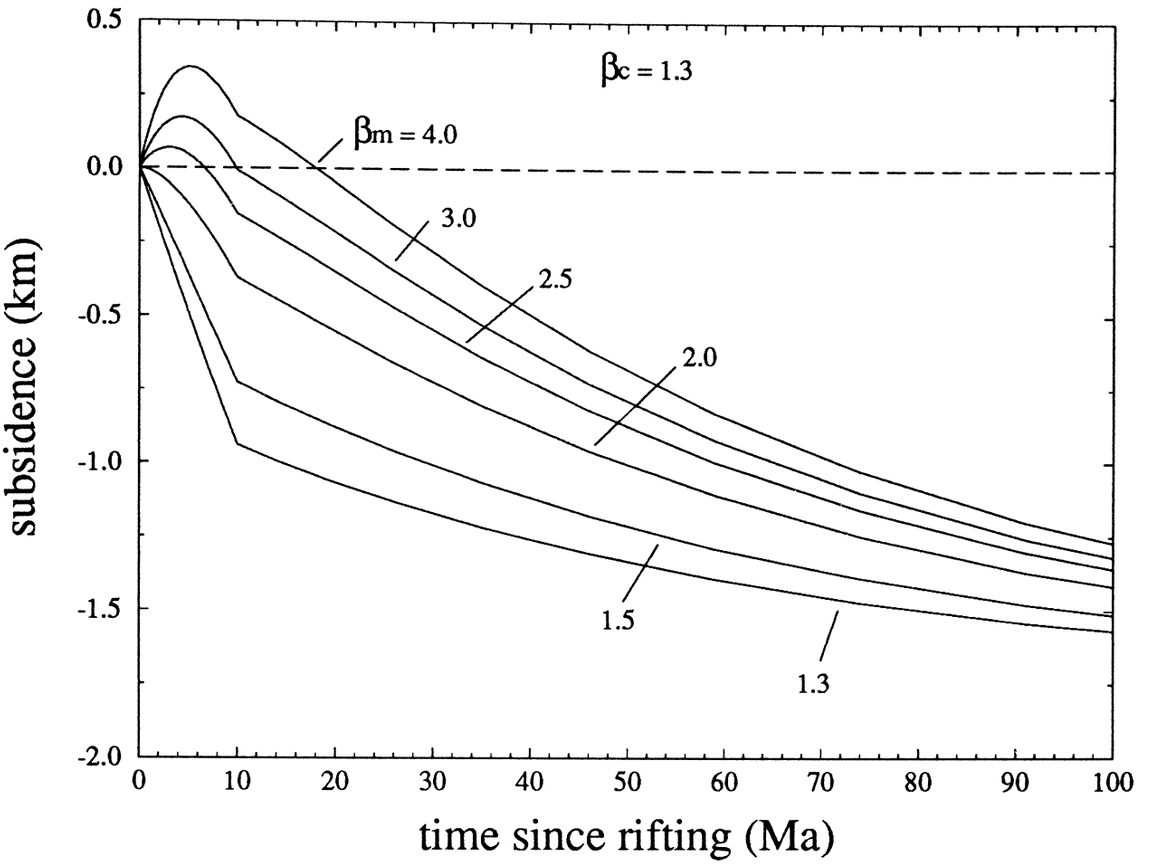

Figure 6.18. Theoretical subsidence curves for two-layer, finite-duration stretching model calculated for crustal stretching factor, $\beta_c = 1.3$ and various values of mantle stretching factor, β_m. Stretching duration is 10 Ma. Crustal thickness $y_c = 31.2$ km, lithospheric thickness, $a = 125$ km.

Figure 6.19 shows the results of the two-layer finite-duration stretching model applied to three wells on the flanks of the Basin. The same modelling parameters (Table 5.2, p. 196) were used. The results show that, to obtain a reasonable fit between the observed and calculated subsidence, the rifting duration had to be made longer (17–20 Ma) and the stretching factors much larger ($1.5 > \beta_c > 1.9$, $4 > \beta_m > 10$) than those obtained using the uniform stretching model, which is quite unlikely. Such high mantle stretching factors is geologically implausible because they result in "space problems", which would have to be explained by some form of large-scale relay that transfers part of the strain outside the region of stretching. It seems, therefore, that the two-layer stretching model can not explain the subsidence pattern in the Malay Basin wells.

Where the lithosphere has little rigidity, uplift of rift flanks was explained

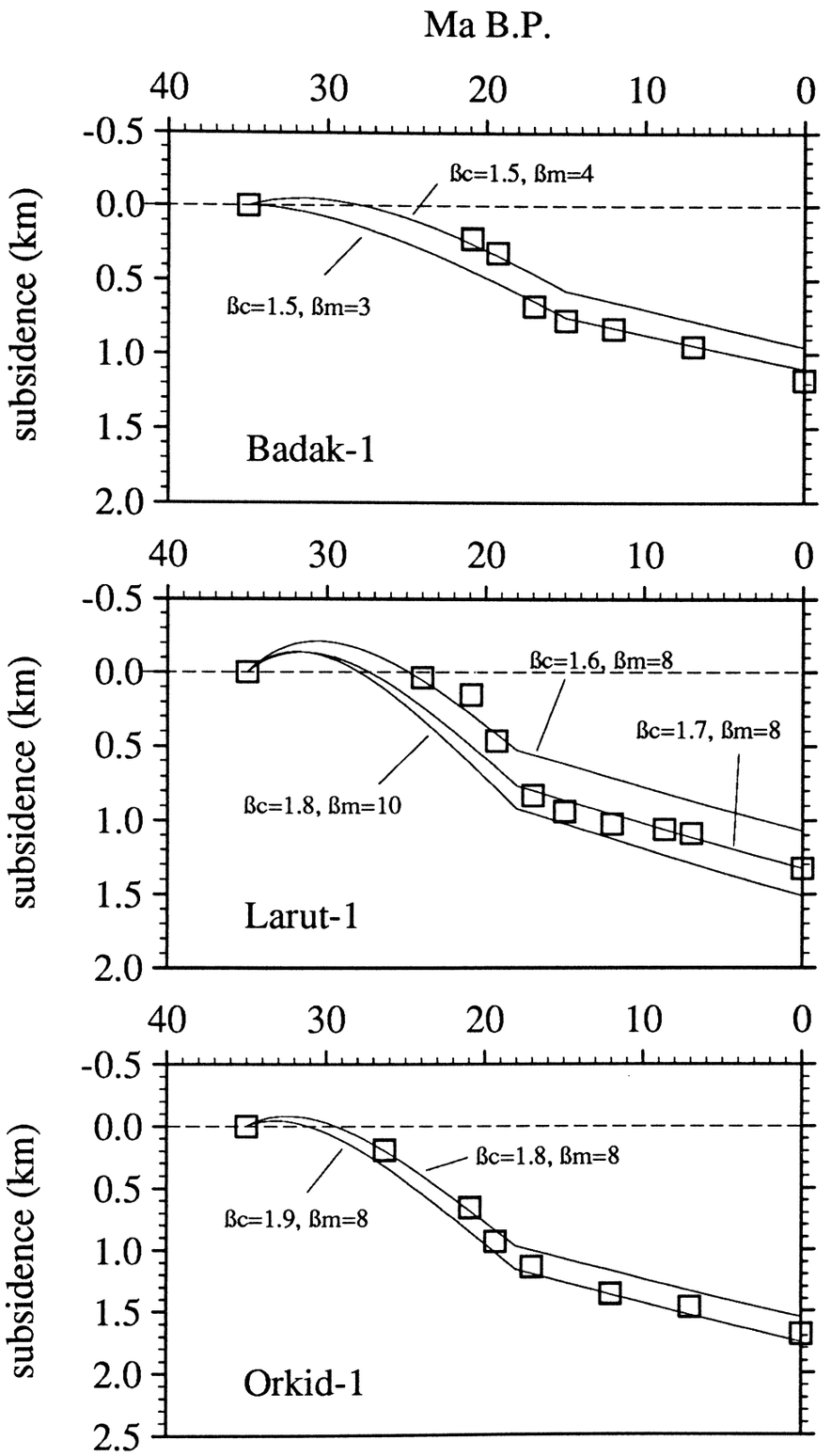

Figure 6.19. Results of two-layer stretching model for Malay Basin wells. Rifting duration is 20 Ma for Badak-1 and 17 Ma for Orkid-1 and Larut-1. β_m — mantle stretching factor, β_c — crustal stretching factor. Squares represent backstripped tectonic subsidence, curves represent water-loaded calculated subsidence.

by White and McKenzie (1988) using a 2D model of non-uniform stretching in which stretching in the crust and in the mantle part of the lithosphere are distributed differently but the total stretching is the same. Hence, in this model, mass is conserved during stretching. White and McKenzie (1988) showed that when stretching in the mantle lithosphere occurs over a wider region that that in the crust, uplift of the rift flanks results. In Fig. 6.20, the subsidence history of the Malay Basin is simulated using XRIFT, following the approach of White and McKenzie (1988) to try to explain the mechanism of rift flank uplift. The crustal stretching, β_c, and mantle stretching, β_m, as a function of distance, x, across the Basin are described as sine functions

$$\beta_c(x) = 1 + (\beta_{co} - 1)\,\sin(\pi x/W_c) \tag{6.8}$$

$$\beta_m(x) = 1 + (\beta_{mo} - 1)\,\sin(\pi x/W_m) \tag{6.9}$$

where β_{co} and β_{mo} are the respective maximum stretching factors at the basin centre, and W_c and W_m are the widths of the zone of stretching for crust and mantle, respectively. To conserve mass during stretching, the total stretching is made the same, *i.e.* the area under both curves is the same. Hence,

$$\int_0^{W_c} [\beta_c(x) - 1]\,\mathrm{d}x = \int_0^{W_m} [\beta_m(x) - 1]\,\mathrm{d}x \tag{6.10}$$

from which a relationship between β_{co} and β_{mo} is derived:

$$\beta_{mo} = 1 + (\beta_{co} - 1)\,W_c/W_m \tag{6.11}$$

The structural evidence (Chapter 4) and gravity data (Chapter 5) suggest that the zone of crustal stretching in the Malay Basin (W_c) is about 100 km wide. The maximum crustal stretching factor, β_{co}, is assumed to be 2.5, based on the gravity modelling results. W_m is assumed to be twice of W_c (200 km), and hence $\beta_{mo} = 1.75$ (Fig. 6.20A). The duration of rifting is assumed to be 10 Ma. Figure 6.20B shows the calculated water-filled subsidence during the postrift phase. Note that, by the end of rifting (after 10 Ma), the basin flanks were uplifted to ~0.7 km

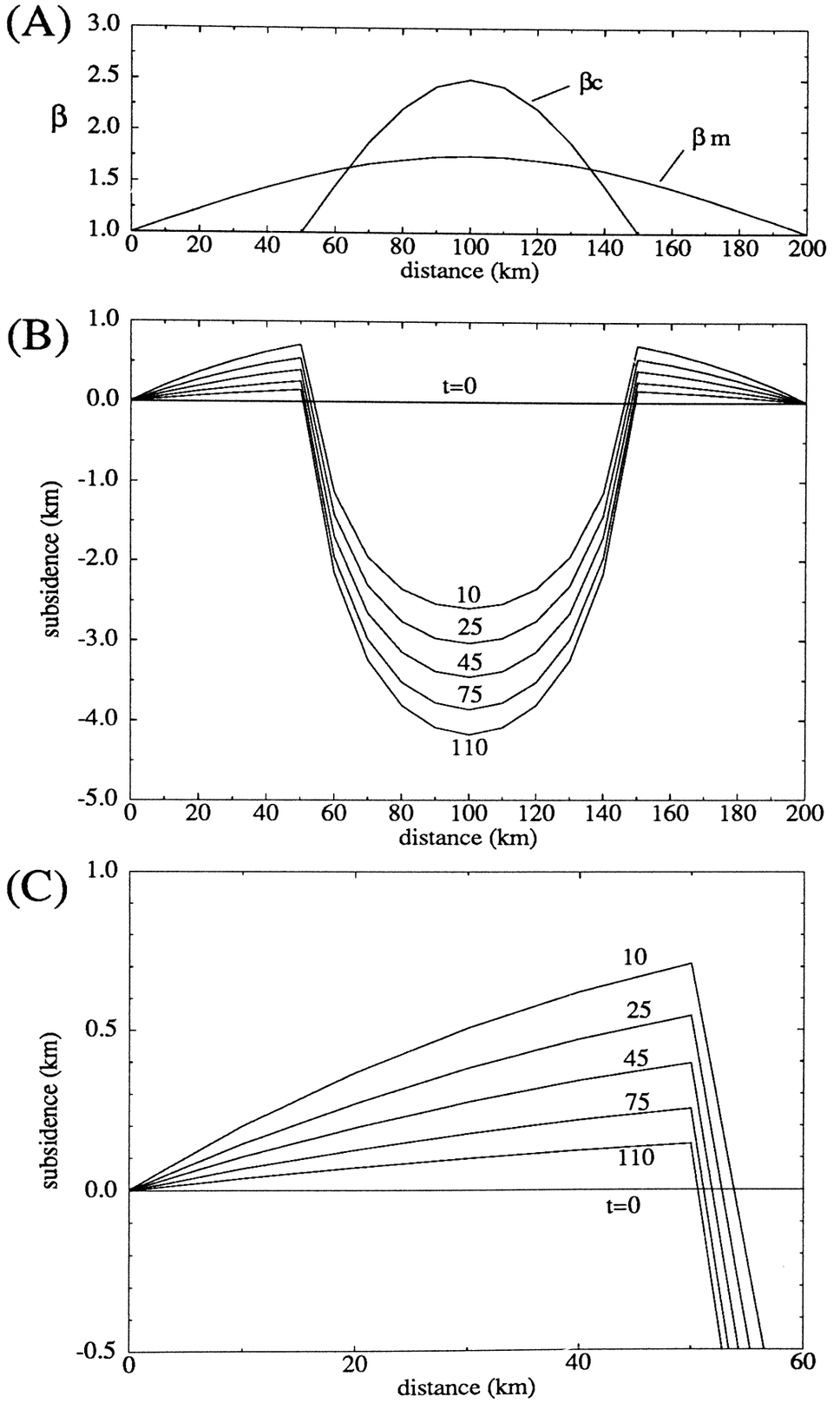

Figure 6.20. Two-dimensional, two-layer, finite-duration stretching model (A) Distribution of stretching factors, approximated as sine functions β_c – crust, β_m – mantle lithosphere. Note that the area under the curves are the same. (B) Water-filled tectonic subsidence profiles calculated using the β profiles in (A). Rifting duration: 10 Ma. Shown are curves for times since rifting in Ma. Note the uplift of basin flanks at the end of stretching phase (10 Ma). (C) Close-up of basin flank between 0 and 60 km in (B), showing the subsidence during the post-stretching phase.

above sea level but soon subside as a result of cooling of the lithosphere. The uplift occurs because, beneath the flanks, the mantle lithosphere is thinned more than at the centre, resulting in thermal uplift that is greater than the subsidence caused by crustal thinning. The opposite occurs at the basin centre because thinning of the crust there is greater than that in the mantle. Notice, also, that the basin flanks do not subside below sea level as $t \rightarrow \infty$ because the effects of erosion and sedimentation were ignored in the modelling.

One way to avoid having to invoke a large amount of erosion of the rift flanks so that it will subside below sea level is to assume a Gaussian, instead of sine, function to describe the β profiles, as proposed originally by White and McKenzie (1988). Figure 6.21 shows the results of modelling using Gaussian functions for the β profiles. The relevant equations for $\beta_c(x)$ and $\beta_m(x)$ are given in White and McKenzie (1988). As in the model in Fig. 6.19, exactly the same parameters were used: $W_c = 100$ km, $W_m = 200$ km, $\beta_c = 2.5$, and rifting duration of 10 Ma. The results, however, show a markedly different subsidence pattern which, clearly, is determined by the way in which the stretching functions are specified. The most striking difference, in the case of the Gaussian β functions, is the inward-sloping basin flanks which are absent from the previous model in Fig. 6.19. The total uplift at the end of rifting (10 Ma) is less than 0.3 km, significantly less than that predicted by the sinusoidal β profiles. The Gaussian β profiles produce a relatively narrower basin and a more gently-sloping rift flanks. The total synrift subsidence (after 10 Ma) is slightly greater in the Gaussian than in the sinusoidal model.

Lateral heat flow

Another possible contributing factor to flank uplift is lateral heat flow through the sides of the Basin because of the temperature gradient that exists between the stretched central region of the Basin and the relatively cool unstretched margins. As a result, the basin flanks are temporarily uplifted during the synrift and postrift

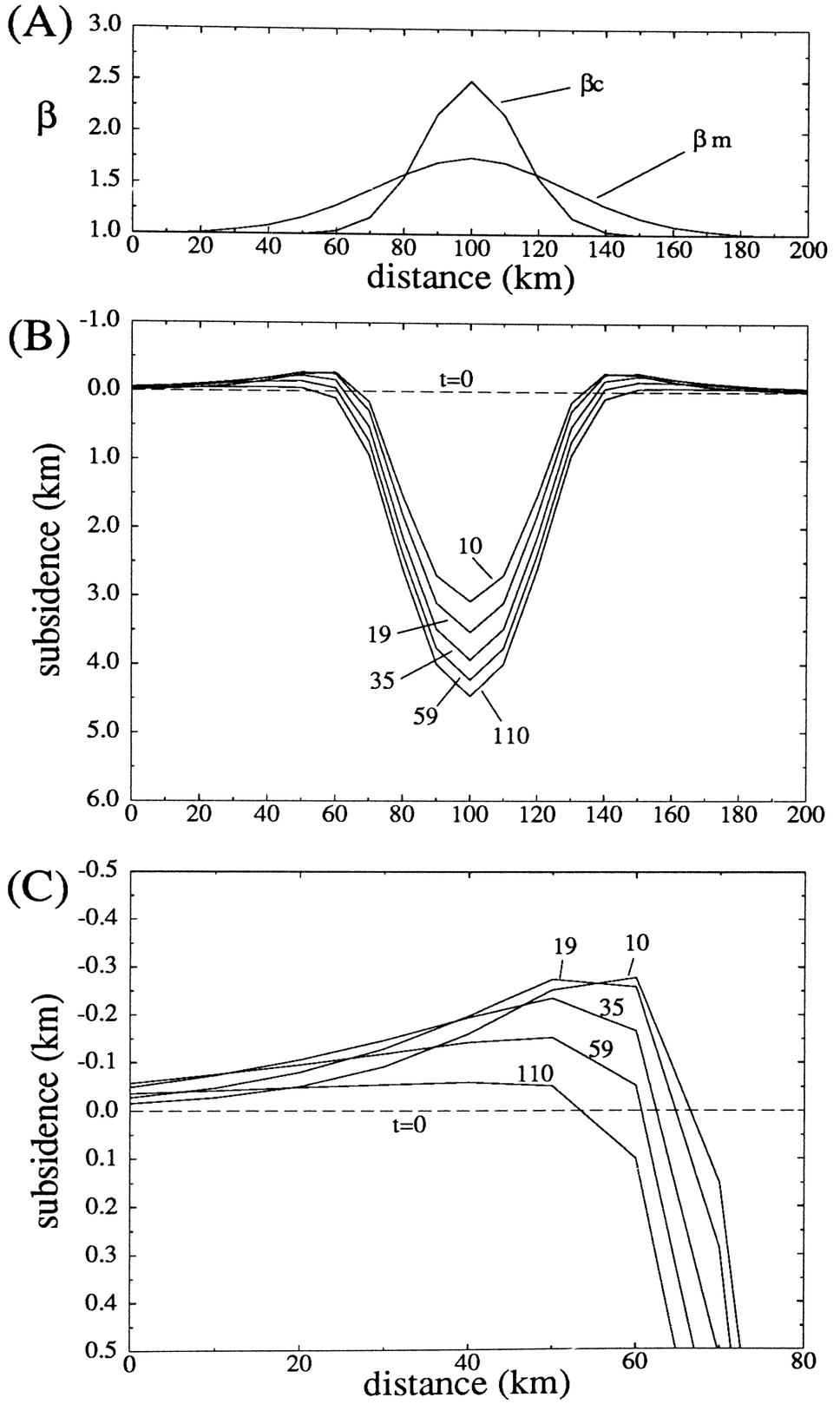

Figure 6.21. Two-layer, finite-duration stretching model, as in Fig. 6.19, calculated using (A) Gaussian distribution of stretching factors, β_c – crust, β_m – mantle lithosphere. (B) Water-filled tectonic subsidence profiles calculated using the β profiles in (A). Rifting duration: 10 Ma. Shown are curves for times since rifting in Ma. Note the uplift of basin flanks at the end of stretching phase (10 Ma). (C) Close-up between 0 and 80 km of (B), showing the subsidence of basin flanks during the thermal subsidence phase.

phases as heat is conducted from the centre outwards. The effect of lateral heat conduction during the synrift phase is significant, especially in narrow, "thick-skinned" strike-slip or pull-apart basins (Pitman and Andrews, 1985).

By incorporating lateral heat conduction in the model, the problems associated with non-uniform stretching or flexural rigidity can be avoided. Figure 6.22 shows the subsidence along a 2D profile across the Basin, incorporating the effects of lateral heat flow (see Appendix B.1 for details). In this experiment, uniform stretching is assumed, while the β profile is the same as that for β_c in Fig. 6.21A. For computation of the subsidence, which includes lateral and vertical heat conduction, the two-dimensional heat flow equation is solved using XRIFT (Appendix B.1). The lithosphere is divided into blocks, each 10 km wide, and the temperature structure of each block is monitored throughout the stretching phase before calculating the subsidence (Cochran, 1983). It is assumed, as before, that the stretching duration is 10 Ma.

Figure 6.22 compares the result of modelling the subsidence when (A) only vertical heat conduction is considered and (B) both vertical and horizontal heat flow are incorporated. We can see, in (B), the basin flanks are temporarily uplifted as a result of heat flow into the unstretched region. Also, for a given time since the start of rifting, the subsidence in (B) is correspondingly greater than in the case of vertical heat conduction only (A). The flank uplift is transient in nature because when the lithosphere cools, it subsides to its equilibrium elevation (sea level). Note also, in (C), the uplift continues for some time after the stretching ends because of the continuing flow of heat from the centre of the Basin as the lithosphere cools. If the uplifted basin flanks are partially eroded, the resulting surface will subside below sea level, thus giving the subsidence pattern observed in the backstripped wells.

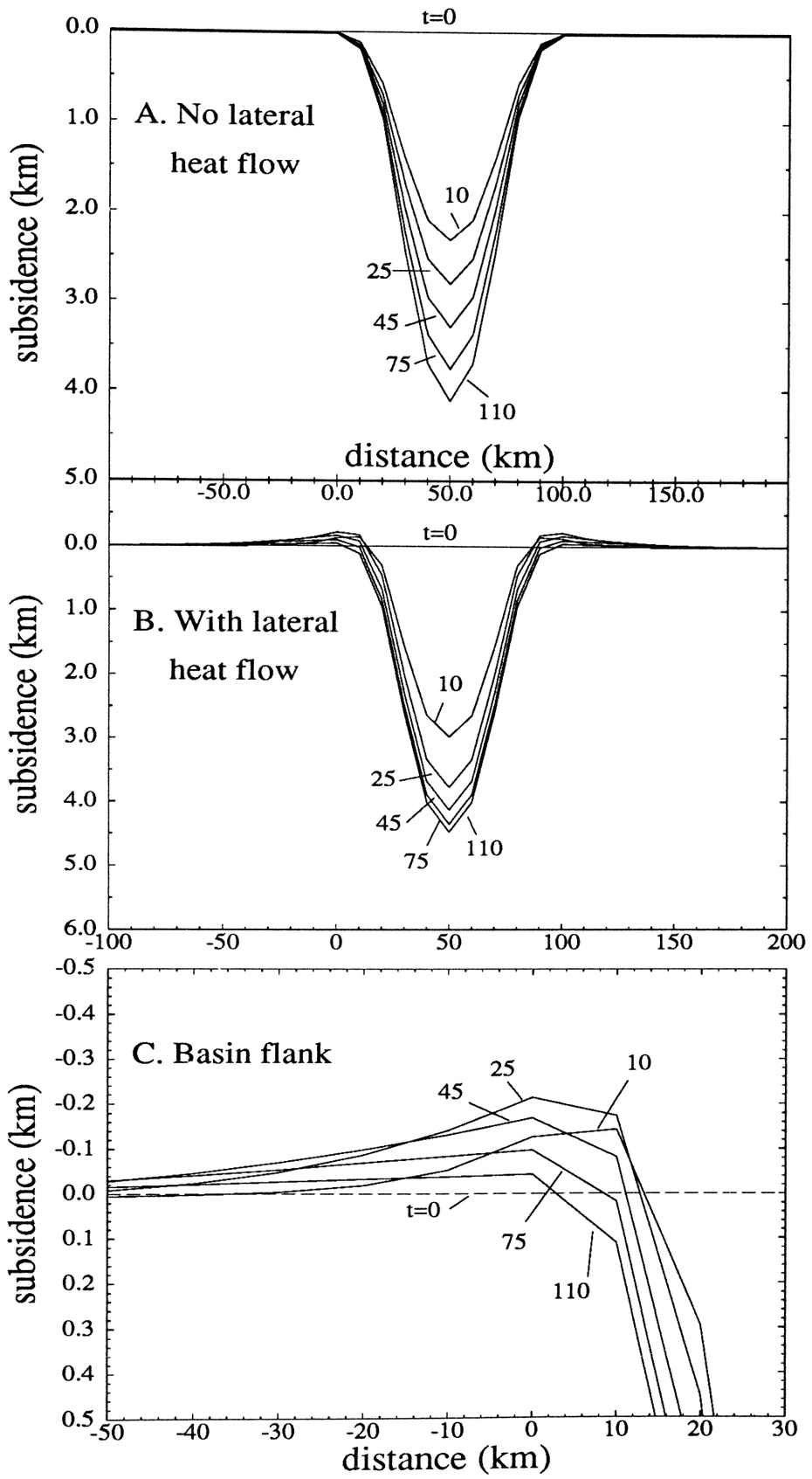

Figure 6.22. Basin model with lateral heat flow effects. Uniform stretching is assumed. Rifting duration 10 Ma. β profile the same as that for β_c in Fig. 6.21A. (A) Computed water-filled subsidence profile without lateral heat flow, for comparison. Lines represent time since rifting in Ma. (B) Subsidence with lateral heat flow included. Note the uplift of basin flanks. (C) Close-up of basin flank to show subsidence pattern.

6.3.3 Basin Simulation

In this section, the non-uniform stretching model, incorporating vertical and lateral heat flow, is used to simulate the stratigraphic pattern in the Malay Basin. It is assumed that any surface elevated above zero is eroded instantaneously to sea level before the next increment of sedimentation. Compaction of sediments is calculated using the exponential porosity-depth relationship discussed in Section 6.2.1. Airy isostasy is assumed throughout.

Figure 6.23 shows the result of a simulation using the same β profiles as in Fig. 6.21A but incorporating sedimentation at regular time intervals, assuming a basin age of 35 Ma. The results show that erosion of the basin flanks resulted in subsidence below sea level during the postrift phase, which created extra accommodation space for sediment to accumulate. The width of the postrift basin is larger than that of the synrift basin, both of which are roughly the same as the width of the stretching zones in the mantle and in the crust (Fig. 6.20A). This is a useful observation because the widths of the synrift and postrift basins may be used a rough indicator of the widths of crustal and mantle stretching zones, respectively.

A characteristic feature of the simulated stratigraphy is the onlap of postrift strata onto the flanks of the basin, as was described by White and McKenzie (1988) (Fig. 6.23C), producing the typical steer's head geometry (Fig. 1.7, p. 16). The Malay Basin has a similar cross-sectional geometry (Fig. 4.5, p. 125) characterised by a relatively narrow synrift basin, overlain by a much wider postrift basin. The inward-sloping basin margins become surfaces towards which the postrift strata onlap and pinch out.

The simulation results above suggest that the basic geometry of the Malay Basin can be explain by a model that combines non-uniform pure-shear stretching of the lithosphere and the effects of lateral and vertical heat flow. A steer's head basin geometry with similar stratigraphic architecture may also result if

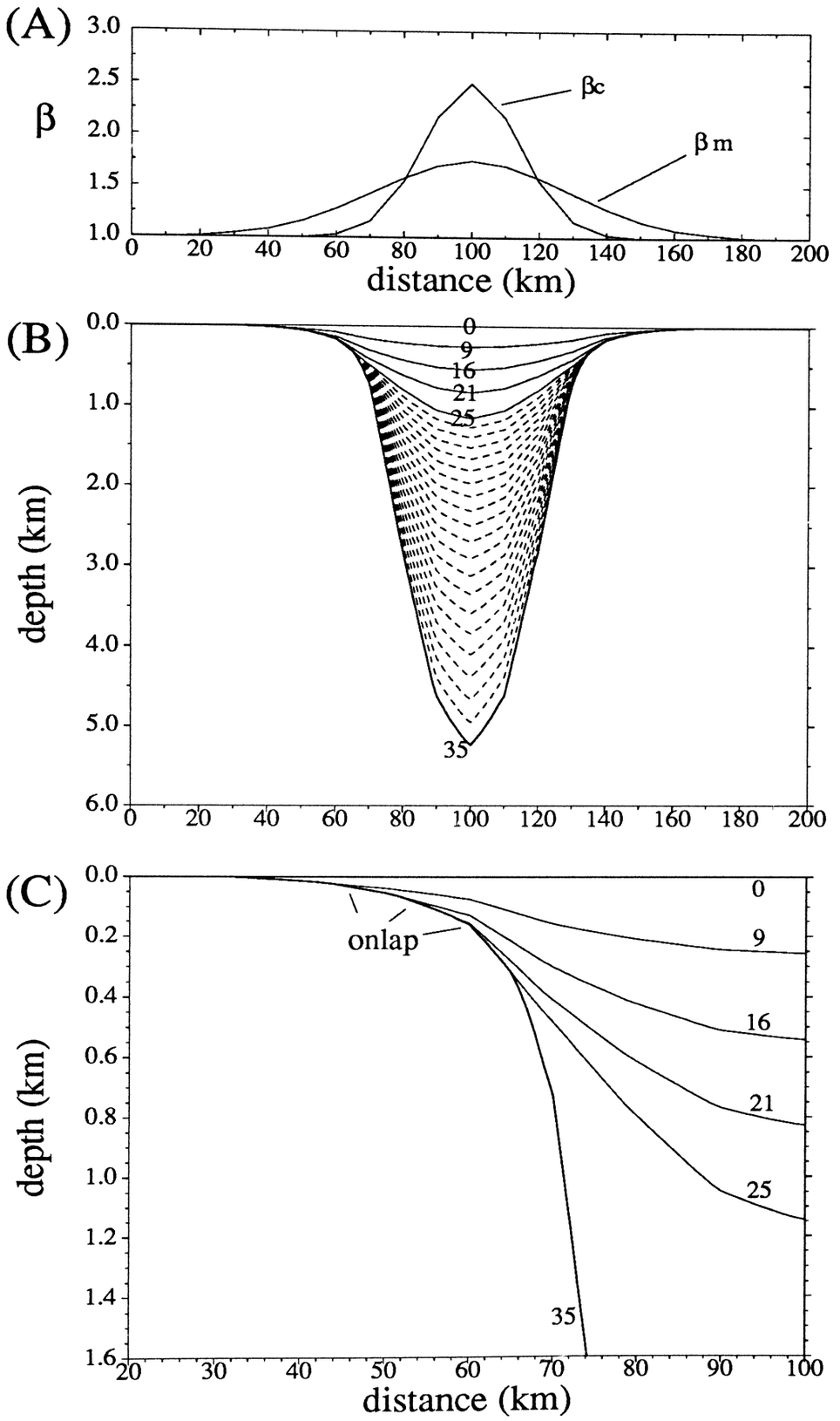

Figure 6.23. Simulation of basin in Fig. 6.21 incorporationg erosion and sedimentation. (A) Gaussian β distribution in mantle and crust. (B) Simulated basin stratigraphy. Dashed lines represent time-lines within synrift sediment at 0.5 Ma intervals, solid lines represent post-rift horizons with the indicated ages. Uplifted rift flanks (see Fig. 6.20B) are assumed to be eroded to sea level, resulting in net subsidence during postrift phase. Sediment compacts according to exponential porosity law (Section 6.2.1). Flexural rigidity = 0. (C) Close-up of basin margin in (B) showing the onlap by postrift strata on the margins.

the stretched lithosphere, although infinitely weak during the stretching phase, becomes increasingly rigid after stretching has ceased, as suggested by Watts *et al.* (1982). In their model, flexural rigidity is assumed to follow the depth to the 450° oceanic lithospheric isotherm, which implies that flexural rigidity increases as the lithosphere cools during the postrift phase. The width of the basin increases with time during the postrift phase, resulting in stratigraphic onlap at the basin margins (Fig. 6.24). This model, however, assumes that continental lithosphere behaves the same way as oceanic lithosphere, *i.e.* the flexural rigidity is a function of thermal structure and, hence, age. There is still some uncertainty as to whether this assumption is valid. Studies of continental T_e (Watts, 1992; Burov and Diament, 1995) have shown that the relationship between T_e and plate age, or cooling history, in continental lithosphere is not as straight-forward as was previously believed.

Because the effective elastic thickness, T_e, of the lithosphere in the study area is low (< 12 km) (Chapter 5), the role of flexure in basin evolution is considered to be minimal. Figure 6.25 compares the results of simulation for several values of T_e. The figure suggests that there is very little difference in the overall shape and internal stratigraphy of the Basin for the range of T_e used in the model. When T_e is greater than 0 km, *i.e.* the lithosphere is more rigid, the resulting basin is marginally wider/shallower compared to when $T_e = 0$. Because the results from gravity modelling (Chapter 5) have indicated that T_e is unlikely to be greater than about 10–12 km, it is probably justified to assume Airy isostasy when modelling the stratigraphy of the Basin.

6.3.4 Subsidence at Centre of Basin

Wells at the centre of the Basin are a problem because they penetrate only the topmost portion of the postrift stratigraphy, which could result in errors in the β estimation. Figure 6.26 shows the subsidence curves for six wells at the centre of the Basin. The observed subsidence curves require unrealistically high β values

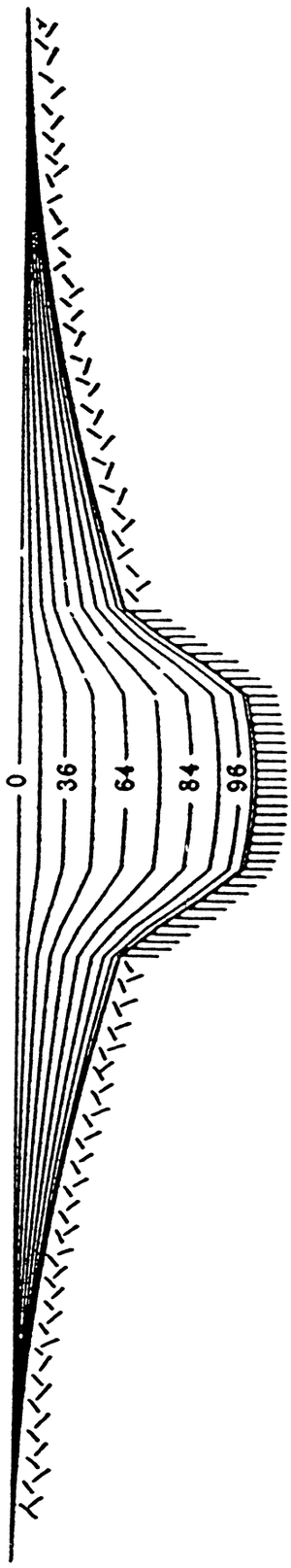

Figure 6.24. Alternative model for generating stratigraphic onlap at basin margins (from fig. 13b of Watts *et al.* 1982), which assumes flexural rigidity that follows the depth 450° isotherm. Stretching factor, β, at centre of basin is 2, T_e varies with time and space. Only vertical heat flow included in the calculation.

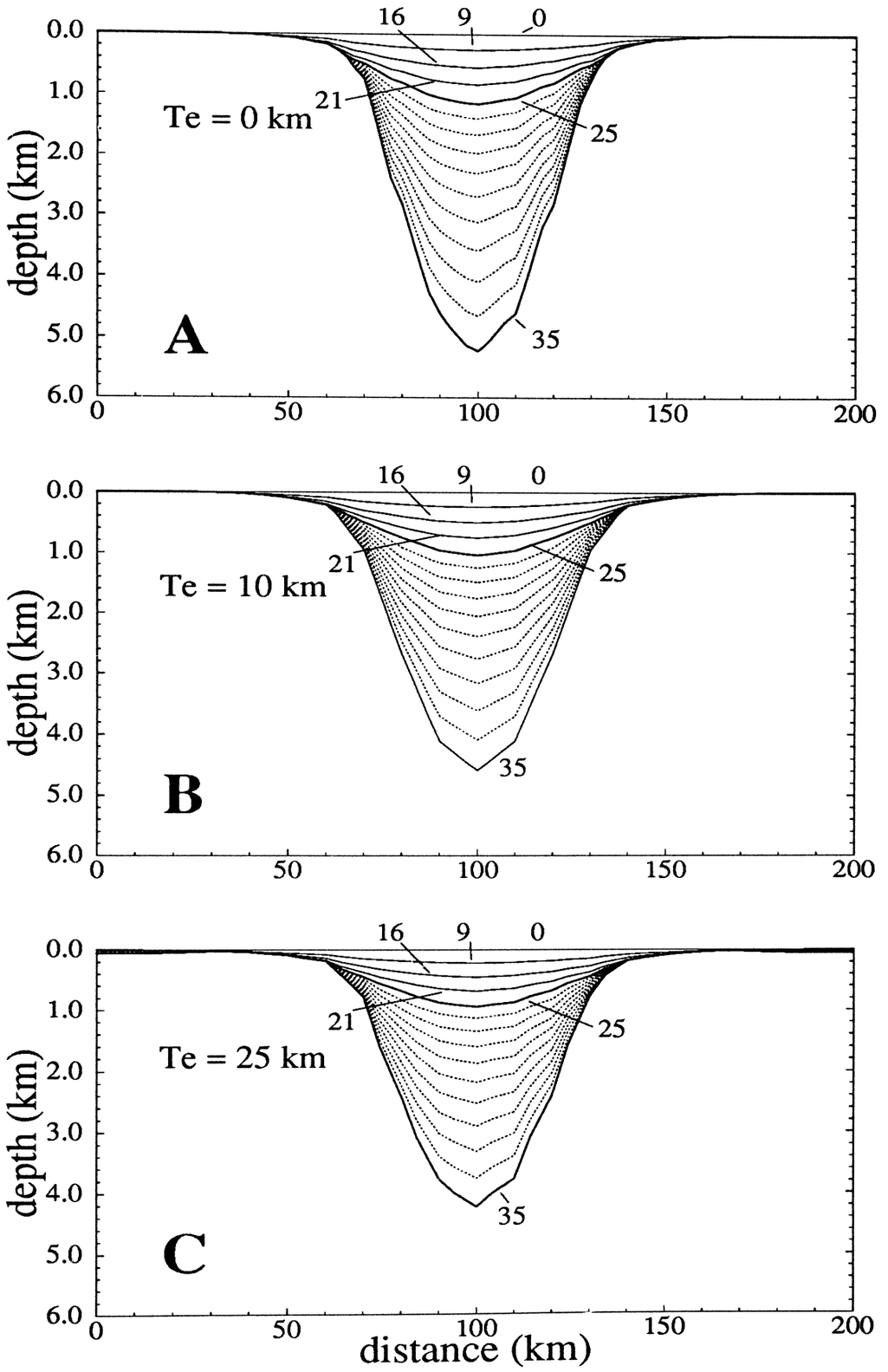

Figure 6.25. Model simulation of non-uniform stretching with finite flexural rigidity (T_e) for the same basin in Fig. 6.23. T_e is assumed to be constant in time and space. (A) $T_e = 0$ km (same as Fig. 6.23B). (B) $T_e = 10$ km. (C) $T_e = 25$ km. Labels represent age of horizon in Ma. Dashed lines represent synrift time lines at 0.5 Ma interval.

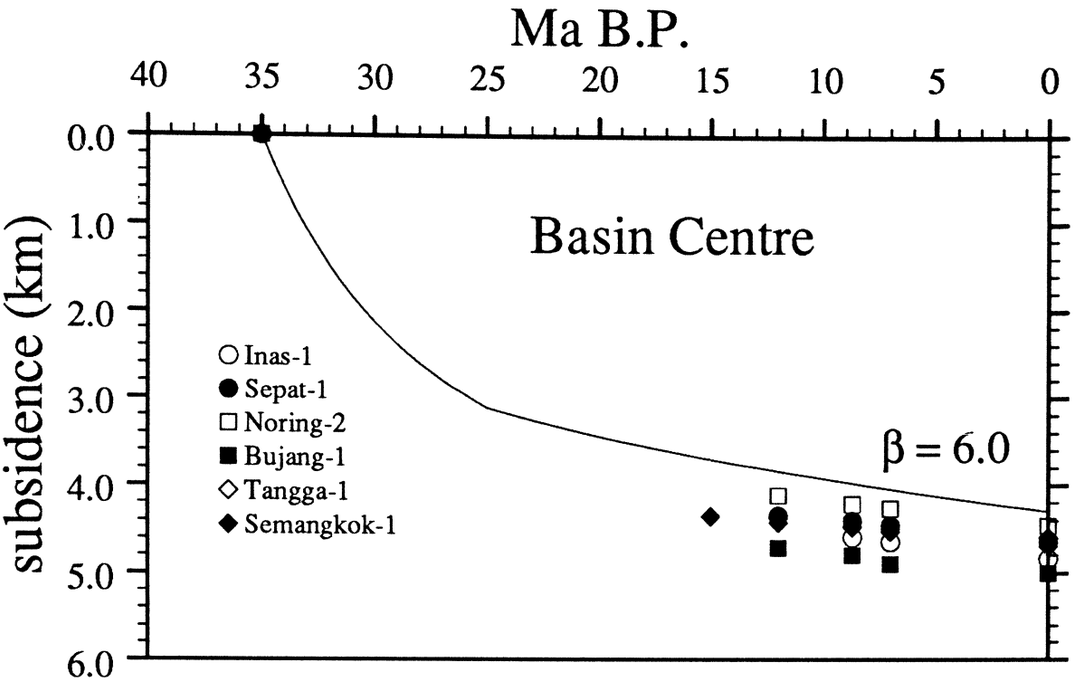

Figure 6.26. Subsidence curves for the wells at the centre of the Malay Basin. Note that unrealistically high β ($\ll 6$) is needed to explain the subsidence.

(>6) to account for the large amount of subsidence. As pointed out at the beginning of this chapter (see Fig. 6.7B, p. 211), the tectonic subsidence in the Basin (up to 5 km) can not be explained by β values less than 4. In fact, the gravity data suggest that the minimum and maximum stretching factors are 2.3 and 3.4, respectively. It seems that the estimation of β, particularly at the centre of the Basin, is unreliable.

Because the subsidence history in the central wells represents the postrift subsidence only, β may be estimated from the slope of the thermal subsidence curve. For simplicity, the instantaneous stretching model is used. Stretching is assumed to have occurred 35 Ma ago. β is estimated from the slope of the plot between the observed tectonic subsidence, $S_T(t)$, and $(1 - e^{-t/\tau})$, where t is time since stretching and τ is the thermal time constant of the lithosphere (62.75 Ma). Figure 6.27 is a plot of tectonic subsidence *vs* $(1 - e^{-t/\tau})$ for the six wells at the centre of the

Basin (well location in Fig. 6.8). The slope, m, is obtained by linear regression, and is equivalent to

$$m = E_o \left(\frac{\beta}{\pi}\right) \sin\left(\frac{\pi}{\beta}\right) \tag{6.12}$$

where $E_o = 4a\rho_m \alpha T_o / \pi^2(\rho_m - \rho_w)$ (McKenzie, 1978). The parameter values in Table 5.2 give $E_o = 3.20$ km. β is solved iteratively using 6.12. The results are tabulated in Table 6.4. The slope of the curves give β values ranging from 1.60 in Semangkok-1 to as high as 4.43 in Inas-1.

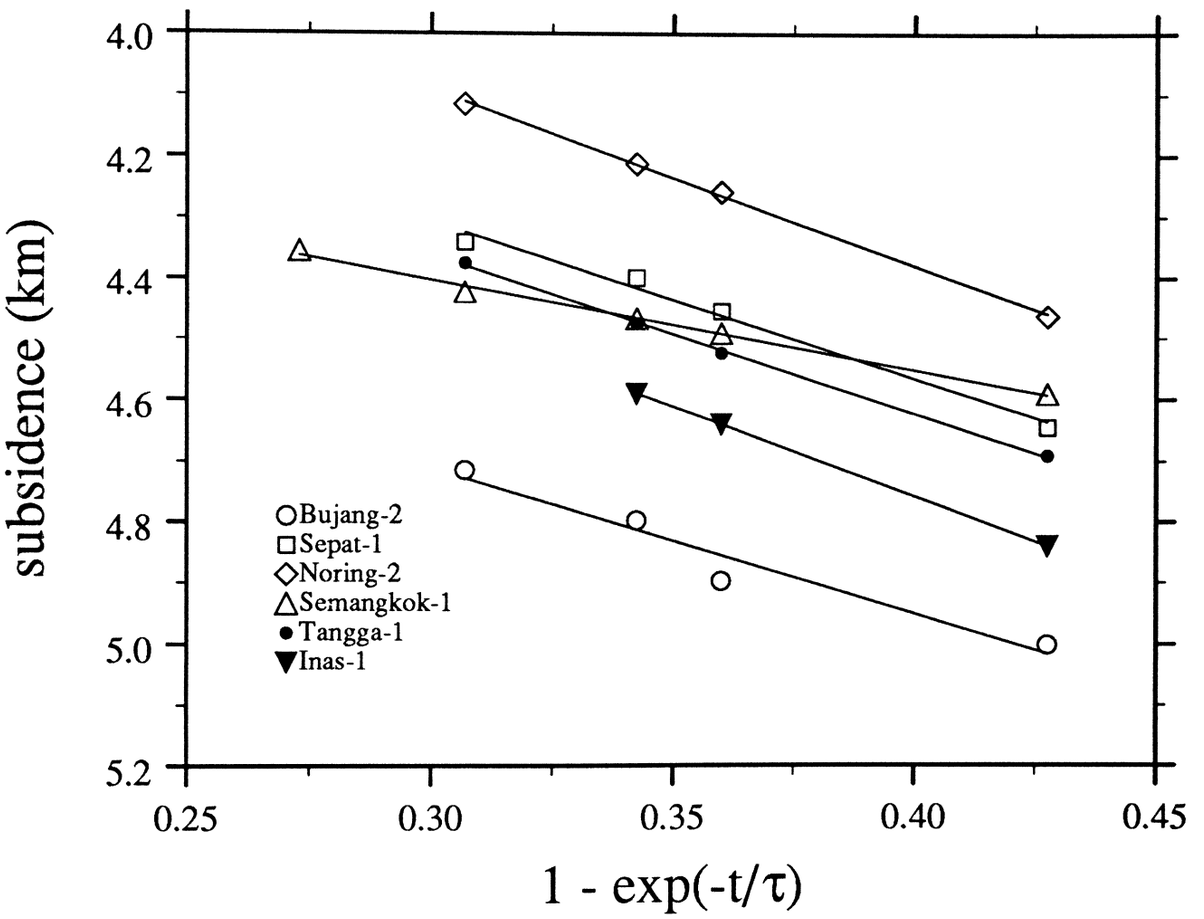

Figure 6.27. Plot of subsidence *vs* $(1\text{-}e^{-t/\tau})$ for six wells at the centre of the Malay Basin.

In Fig. 6.28, the stretching factor derived from the tectonic subsidence is contoured to show the extent of lithospheric thinning in the Basin. The map suggests that the maximum stretching factors obtained from backstripped stratigraphic data are comparable with, although somewhat higher than, those derived from the gravity modelling (Chapter 5), which indicates maximum crustal thinning, β_c, of only 3.4. The apparent discrepancy may have arisen, partly, because

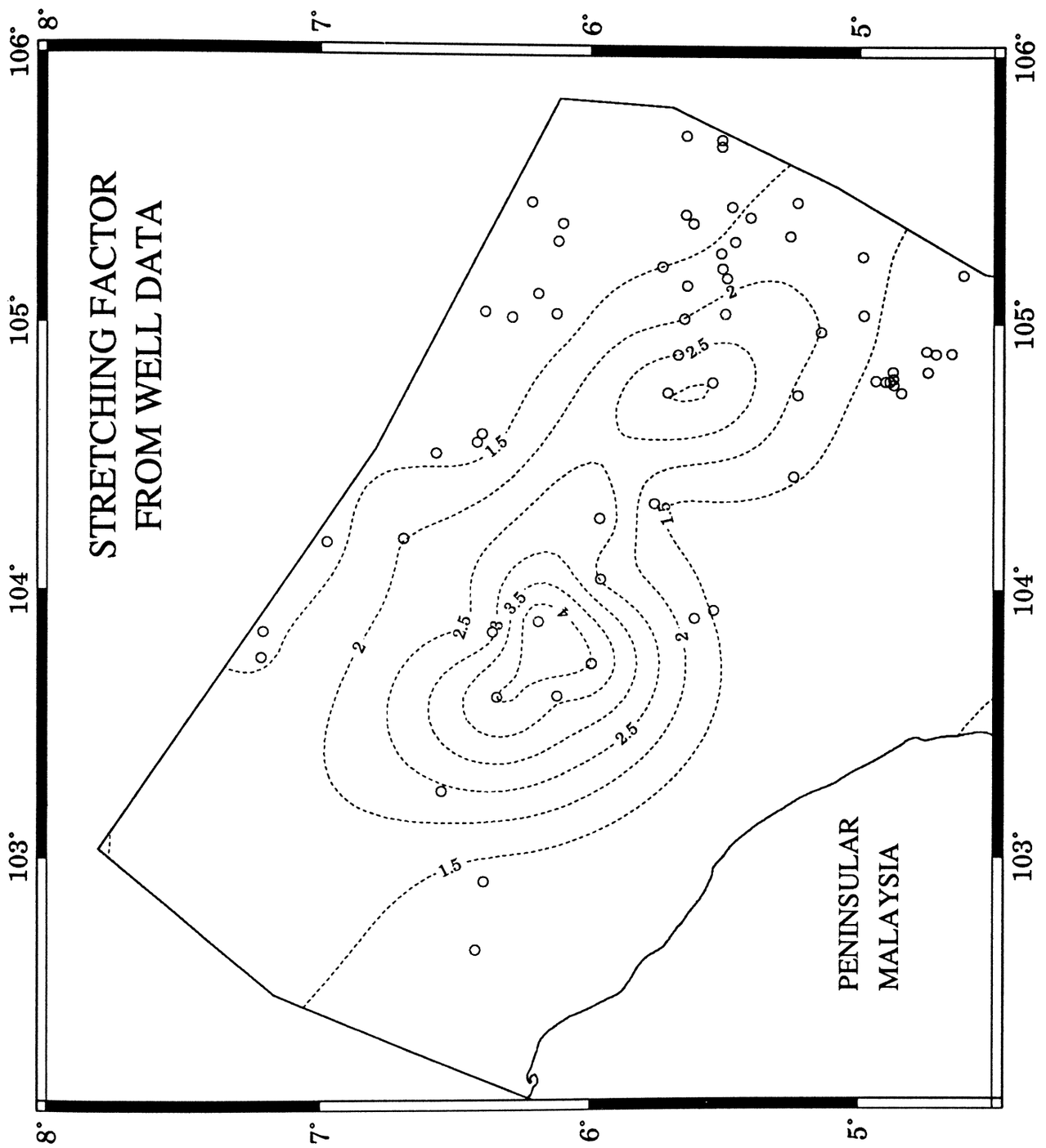

Figure 6.28. Contour map of stretching factor, β, in the Malay Basin, derived from 1D backstripping of well data. Contour interval = 0.5. Small circles represent data points.